Advances in Optics and Photonics

Toward real-time terahertz imaging

HICHEM GUERBOUKHA,[1,2] KATHIRVEL NALLAPPAN,[1] AND MAKSIM SKOROBOGATIY[1,*]

[1]Engineering Physics, Polytechnique de Montréal, C. P. 6079, succ. Centre-ville, Montréal, Quebec H3C 3A7, Canada
[2]e-mail: hichem.guerboukha@polymtl.ca
*Corresponding author: maksim.skorobogatiy@polymtl.ca

Received May 2, 2018; revised August 31, 2018; accepted September 21, 2018; published November 15, 2018 (Doc. ID 330724)

Terahertz (THz) science and technology have greatly progressed over the past two decades to a point where the THz region of the electromagnetic spectrum is now a mature research area with many fundamental and practical applications. Furthermore, THz imaging is positioned to play a key role in many industrial applications, as THz technology is steadily shifting from university-grade instrumentation to commercial systems. In this context, the objective of this review is to discuss recent advances in THz imaging with an emphasis on the modalities that could enable real-time high-resolution imaging. To this end, we first discuss several key imaging modalities developed over the years: THz transmission, reflection, and conductivity imaging; THz pulsed imaging; THz computed tomography; and THz near-field imaging. Then, we discuss several enabling technologies for real-time THz imaging within the time-domain spectroscopy paradigm: fast optical delay lines, photoconductive antenna arrays, and electro-optic sampling with cameras. Next, we discuss the advances in THz cameras, particularly THz thermal cameras and THz field-effect transistor cameras. Finally, we overview the most recent techniques that enable fast THz imaging with single-pixel detectors: mechanical beam-steering, compressive sensing, spectral encoding, and fast Fourier optics. We believe that this critical and comprehensive review of enabling hardware, instrumentation, algorithms, and potential applications in real-time high-resolution THz imaging can serve a diverse community of fundamental and applied scientists.

https://doi.org/10.1364/AOP.10.000843

Toward real-time terahertz imaging

Hichem Guerboukha, Kathirvel Nallappan, and Maksim Skorobogatiy

1. INTRODUCTION

Science and technology behind modern day imaging have come a long way since the invention of the photography in the 1800s. In the same century, many great minds devoted their energy to comprehend the nature of light, culminating in the famous theory of electromagnetism summarized in Maxwell's equations. Today, it is taken for granted that light is an electromagnetic wave, and that visible light constitutes only a very small portion of the electromagnetic spectrum. In the 20th century, imaging moved far beyond the visible spectral range, resulting in the development of many novel imaging techniques, from x-ray radiography that uses waves of subatomic size to radars that employ waves as large as several meters.

Currently, many parts of the electromagnetic spectrum are being widely used for countless applications. This review is dedicated to only a small part of the electromagnetic spectrum in rapid development—the terahertz (THz) range. While there is no unique definition of the THz band, it is generally considered to cover the range of frequencies from 0.1 to 10 THz, having respective wavelengths from 3 mm down to 30 μm (Fig. 1). Today, research in application of THz waves constitutes a very dynamic and multidisciplinary field in rapid development, with many fundamental discoveries being made and practical applications identified [1,2]. At the junction between microwaves and infrared, the THz range shares many of their properties and potential applications. For example, as a natural extension of microwaves, it is seen by many as the next frontier in wireless communications, promising higher data transmission rates to answer the ever-increasing demand for information transfer capacity [3–7].

In the field of sensing and imaging, THz radiation offers unique means to interrogate matter [8]. Like microwaves, THz is capable of penetrating most dielectric materials, revealing inner structures with meaningful contrast. However, different from microwaves, the THz wavelength is sufficiently small to also provide much higher image resolution. Furthermore, many molecular species have unique spectral fingerprints in the THz range. Already, these advantages have been used in multiple fields: industrial environments [9,10]; the pharmaceutical [11,12] and biomedical [13–16] sectors; the agri-food industry [17–19]; defense and security [20,21]; art conservation [22,23]; etc.

We start our review by summarizing in Table 1 some of the most promising commercial sources of THz radiation. For real-time imaging, an intense THz source is clearly beneficial when active illumination of the sample is required. The wavelength of the source is also an important factor as image spatial resolution is directly related to the wavelength of light used in illumination.

Similarly, there are many choices today for detection of THz radiation. Such detectors range widely in their physical operation principles and sensitivities, ranging from thermal bolometers to solid-state transistors. At the same time, with few exceptions, most commercially available detectors, particularly those offering coherent detection, currently come as single-pixel devices. Furthermore, some achieve exceptional sensitivities, at the cost of cryogenic cooling. In the context of THz imaging, important

research effort is currently concentrated toward the development of sensitive multipixel THz cameras operating at room temperatures (see Table 2 for a list of uncooled detectors). While coherent detection is probably too much to hope for in the short term, we nevertheless foresee considerable improvement of the sensitivities and the frame rates of THz cameras, taking advantage of existing microfabrication technology to enable scalability and lower fabrication costs. For more detailed reviews of THz detectors, we suggest several recent publications on this subject [71–73].

As surprising as it may seem, the lack of THz cameras did not impede the development of many ingenious relatively fast and high-resolution THz imaging modalities. In fact, many such imaging techniques cannot be realized using existing THz cameras as they rely on frequency-/time-resolved and field-resolved measurements. The most obvious example is imaging using a THz time-domain spectroscopy system

Figure 1

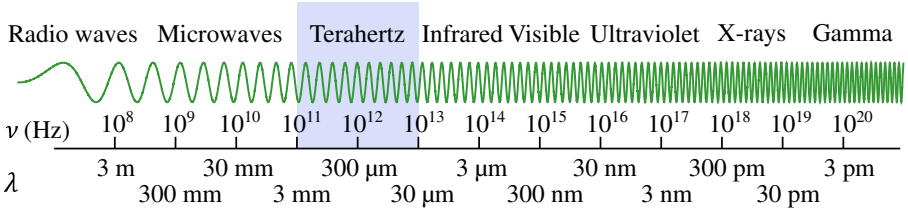

Terahertz range in the electromagnetic spectrum.

Table 1. Typical THz Sources for Off-the-Shelf Imaging Applications

Source and Emission Principle	Mode	Frequency	Power	References
Diode-based frequency multiplier				
Frequency multiplication of microwave source (e.g., Gunn/IMPATT diodes) with Schottky diode	CW tunable	<2 THz	++	[24]
Backward wave oscillator				
Backward acceleration of an electron beam in a corrugated traveling wave-tube under vacuum	CW tunable	<1 THz	+++	[25–27]
Quantum cascade laser				
Cascade of electrons in intersubband transitions by engineered quantum well heterostructures	CW pulsed	~1 – 10 THz	++	[28–31]
Photomixer				
Frequency difference through beating of two optical frequencies in a semiconductor	CW tunable	<3 THz	+	[32–34]
Difference frequency generation				
Nonlinear polarization at the difference frequency of two optical pump beams in a nonlinear crystal	CW tunable	<4 THz	+++	[35]
Parametric amplification and injection seeding				
Second-order nonlinear conversion of a pump pulse into two photons of lower energies (signal and idler)	CW tunable	<3 THz	+++	[36–39]
Photoconductive antenna (THz-TDS)				
Ultrafast photoexcitation of charge carriers in a biased semiconductor gap	Pulsed	<3 THz	++	[40–46]
Optical rectification (THz-TDS)				
Time-varying polarization proportional to the picosecond envelope of a pumping ultrafast optical pulse in a nonlinear crystal	Pulsed	<6 THz	++	[47–51]

Table 2. Typical THz Detectors/Cameras Operating at Room Temperature

Detector	Detection Principle	NEP[a] (pW/$\sqrt{\text{Hz}}$)	Array	References
Thermal				
Microbolometer	Resistive change by thermal excitation	~10–100	Possible (Section 4.1)	[52–54]
Pyroelectric detector	Polarization change by thermal excitation of a pyroelectric crystal	~10–1000	Possible (Section 4.1)	[55–57]
Golay cell	Pressure change by thermal excitation of an encapsulated gas	~100–1000	Single-pixel	[58]
Mixer				
Schottky-barrier diode	High-frequency detection enabled by fast switching speeds in metal/semiconductor junction	~10–100	Possible	[59,60]
Plasmonic detector				
Field-effect transistor	Plasmonic excitation of electronic charge densities in transistor channels	~10–100	Possible (Section 4.2)	[61–63]
Optically triggered (THz-TDS)				
Photoconductive antenna	Ultrafast photoexcitation of charge carriers in a semiconductor gap	—	Possible (Section 3.3)	[40–46]
Electro-optic sampling	Birefringence-induced by THz pulse in nonlinear media	—	Possible (Section 3.4)	[64–68]
Air-biased-coherent-detection (ABCD)	THz field-induced second harmonic (TFISH) in plasma gas	—	Single-pixel	[69,70]

[a]The noise-equivalent power (NEP) is defined as the input power that gives a signal-to-noise ratio of 1 with a 1 Hz output bandwidth. It is a measure of the minimum detectable power, and a lower NEP indicates a more sensitive detector.

(THz-TDS) that measures directly the electric field of a short THz pulse in time domain. In fact, historically, the first THz image was obtained using THz-TDS [74]. The principal strength of this method comes from the fact that it provides a broadband spectral image with both amplitude and phase information (Fig. 2). The principal

Figure 2

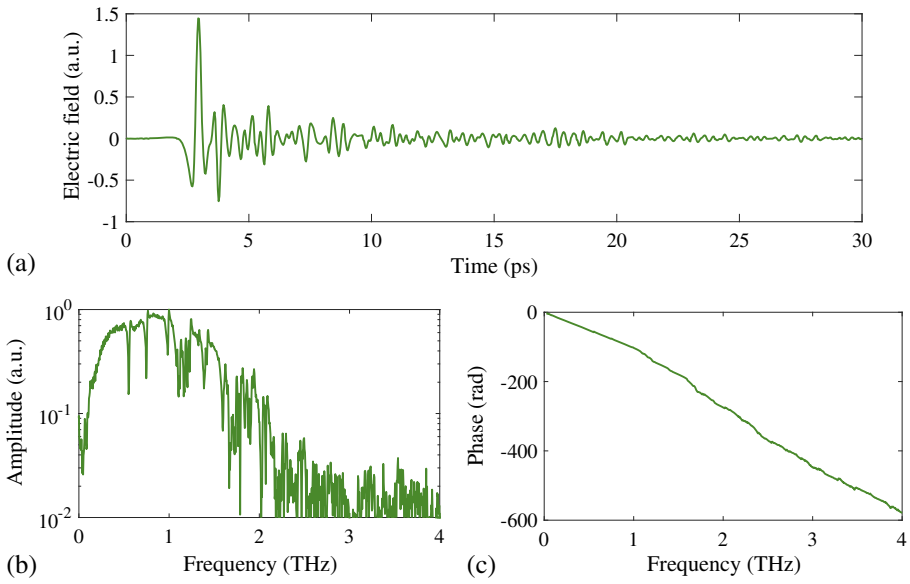

THz-TDS measurement. (a) A THz pulse in the time domain. (b) The corresponding Fourier transform amplitude and (c) phase. The dips in the spectrum correspond to absorption in water vapor.

disadvantage of a classic THz-TDS approach is the necessity of a lengthy two-dimensional (2D) raster scanning in order to obtain an image. This is in clear contrast with THz cameras, which are fast, but limited to the measurement of some spectrally averaged power distribution.

This review is dedicated to the means of achieving real-time THz imaging. The paper is structured as follows. In Section 2, we first review many important THz imaging modalities developed so far: THz transmission, reflection, and conductivity imaging; THz pulsed imaging; THz computed tomography; and THz near-field imaging. In addition to the presentation of those modalities, we also discuss their specific challenges toward real-time image acquisition. Then, in the following sections, we detail various practical realizations of real-time THz imaging systems. In Section 3, we begin by reviewing the fundamentals of THz-TDS and discuss several enabling technologies for real-time imaging: fast optical delay lines, photoconductive antennas arrays, and electro-optic sampling with cameras. In Section 4, we review two major candidates for real-time high-resolution imaging THz cameras. Particularly we review recent progress in THz thermal cameras and THz field-effect transistor (FET)-based cameras. Finally, in Section 5, we overview several promising techniques that enable fast THz imaging with single-pixel detectors: mechanical beam-steering, compressive sensing, spectral encoding, and fast Fourier optics. We believe that this critical and comprehensive review of enabling hardware, instrumentation, mathematical algorithms, and potential applications in real-time high-resolution THz imaging can serve a diverse community of fundamental and applied scientists.

2. TERAHERTZ IMAGING: METHODS AND APPLICATIONS

In this section, we review several classical THz imaging techniques developed over the past two decades. These techniques serve as a benchmark to the novel THz imaging methods that we will detail in the following chapters. Particularly, we discuss the following THz imaging modalities: (1) Imaging with a THz-TDS; (2) THz transmission, reflection, and conductivity imaging; (3) THz pulsed imaging; (4) THz computed tomography; and (5) THz near-field imaging. In the context of this review, our objective is to explain the relevant principles of image reconstruction and identify various potential applications of THz imaging. We will also discuss their specific challenges to achieve real-time image acquisition. Since each of the abovementioned techniques has already been a subject of in-depth reviews in the past, we also refer the reader to these publications.

2.1. Imaging with a THz Time-Domain Spectroscopy System

Historically, the THz time-domain spectroscopy system (THz-TDS) was one of the first ways to measure THz radiation. In THz-TDS, broadband THz pulses are generated and detected using photoconductive antenna or nonlinear optical methods. The generation and detection of THz pulses is detailed in Section 3.1. The strength of the THz-TDS technique is in its ability to measure the amplitude and the phase of the THz electric field in time domain.

We first discuss a classic way of obtaining an image using THz-TDS. As an example, we use a THz-TDS in transmission mode and image a triangle made of high-density polyethylene (HDPE), a star made of paper, and a metallic washer [Fig. 3(a)]. The three samples are placed on top of a paper sheet surrounded by a metallic aperture made of aluminum foil.

To obtain a 2D image, the sample is raster-scanned and individual traces are recorded point by point in the focal plane of a pair of lenses or parabolic mirror that focuses a pre-collimated THz beam [Fig. 3(b)]. The result is a three-dimensional (3D) data cube

with the third dimension being time. A Fourier transform is performed on the third dimension to obtain a hyperspectral image, i.e., an image per THz frequency. To extract useful information and to create an image, a certain normalization must be used to convert the raw one-dimensional (1D) time or frequency data into physically significant values [75–77]. The normalization is chosen to enhance the image contrast and is generally application dependent. It can also involve a reference measurement, for example, a measurement through an empty system or an uncovered substrate. Different examples of normalizations are presented in Fig. 4 (time domain) and Fig. 5 (frequency domain).

Figure 3

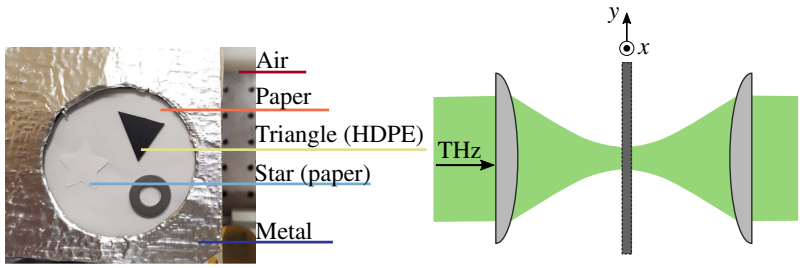

(a) Photograph of the sample. (b) The sample was mechanically moved in the (x, y) focal plane of a pair of lenses.

Figure 4

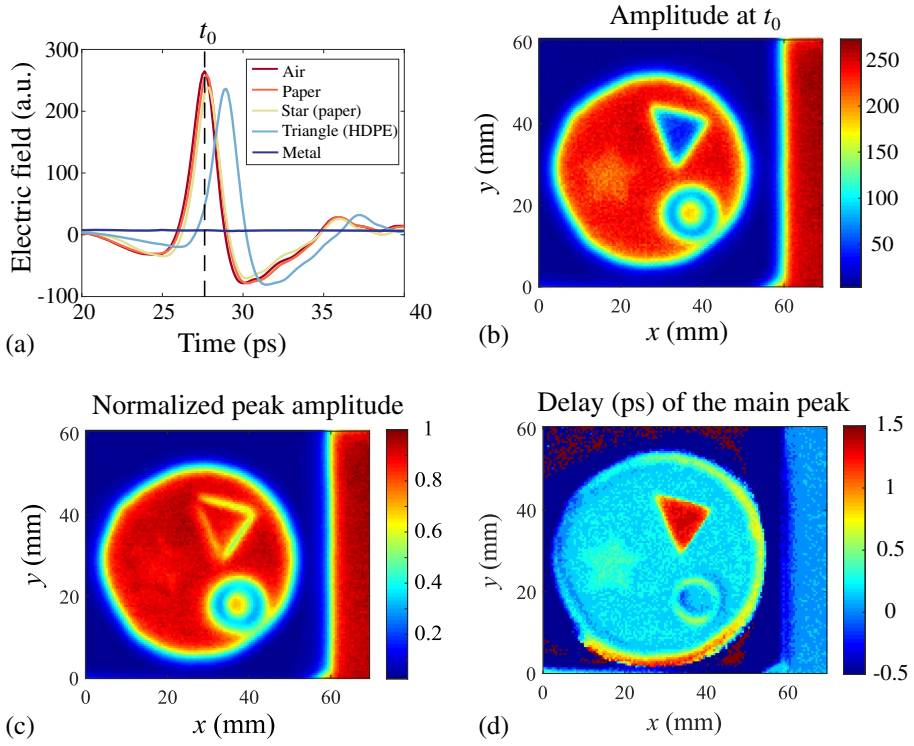

(a) Example of typical THz traces acquired at different positions across the sample in Fig. 3(a). (b) Amplitude of the electric field at $t_0 = 27.6$ ps: $E_{x,y}(t_0)$. (c) Normalized amplitude of the main peak: $\max(|E_{x,y}(t)|)/\max(|E_{\mathrm{ref}}(t)|)$. (d) Delay of the main peak relative to a reference peak: $t\{\max[|E_{x,y}(t)|]\} - t\{\max[|E_{\mathrm{ref}}(t)|]\}$.

In Fig. 4(a), typical THz pulses are shown for different positions in the sample. When interacting with the sample, the THz pulse can be attenuated, delayed, or broadened. In Visualization 1, we present an example of a 3D cube image as a function of time, while in Fig. 4(b), we present a slice of this cube at $t_0 = 27.6$ ps. Visualizing the electric field as a function of time reveals the irradiation dynamics at the picosecond scale. A second common way of creating a THz image is to look at the maximum peak in time domain, normalized by the maximum peak of a reference function [Fig. 4(c)]. Here, the reference is taken as the THz pulse measured in air. The result is an image that provides information about the absorption, reflection, or scattering losses in the material. For example, scattering losses are clearly observable at the borders of the HDPE triangle. A third image can be obtained by mapping the time delay of the main peak with respect to the reference measurement [Fig. 4(d)]. This allows us to map the optical path change $\Delta(x, y) = n(x, y)d(x, y)$ across the sample, which can then provide material/thickness contrast. The temporal cross correlation of the two THz waveforms (with and without the sample) can also be used to visualize the optical path change [78].

By applying a Fourier transform on the third dimension of the data cube, one gets the amplitude [Fig. 5(a)] and the phase [Fig. 5(b)] of the spectrum. The amplitude gives a general indication of the losses, which, in general, increase with the frequency. The phase is related to the optical path (the refractive index/thickness). When necessary, it must be carefully unwrapped in regions of adequate signal-to-noise ratios (SNRs) to avoid numerical artifacts. In Visualization 2, we present an example of a 3D data cube as a function of frequency. In particular, the spatial resolution increases with the THz frequency. In Fig. 5(c), we plot the amplitude at 0.475 THz, while the phase (wrapped into a $-\pi$ to π interval) is shown in Fig. 5(d). The amplitude image shows the losses in

Figure 5

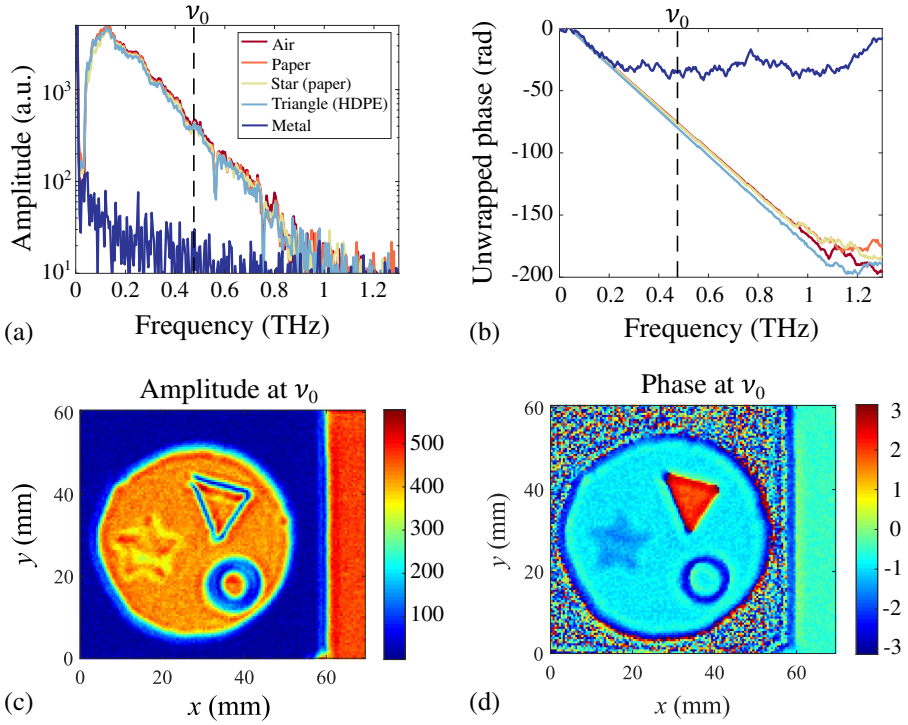

(a) Amplitude and (b) unwrapped phase of the spectrum at different positions across the sample in Fig. 3(a). (c) Amplitude and (d) phase images at $\nu_0 = 0.475$ THz.

the material, which are maximal for the propagation through the metallic washer. Again, scattering losses are observable at the borders of the HDPE triangle. Inside the star paper and the HDPE triangle, the phase image offers more contrast than the amplitude image. This is because, although the losses are similar in those materials, the refractive index is sufficiently different to provide a meaningful contrast. In general, phase imaging inherently possesses a 2π ambiguity that can be removed using a multiwavelength approach [79] or an interferometric scheme [80]. In Section 2.2, we show how to further analyze the THz-TDS measurement to extract the complex refractive index of a material.

Regarding the real-time operation of THz-TDS imaging systems, there are two major problems when using classical THz-TDS setups (see Section 3 for more technical details). The first problem is the need to use an optical delay line to obtain the temporal/spectral dimension. Common to many pump–probe optical experiments, the optical delay line usually comes in the form of a pair of mirrors mounted on a micropositioning stage. The linear mechanical movement of the delay line becomes a hurdle for real-time operation. In Section 3.2, we present alternative solutions for fast optical delay lines that can provide acquisition time in the millisecond scale. The second problem is that one typically employs single-pixel THz detectors due to their wide commercial availability. This means that to obtain an image, one needs to mechanically scan the sample point by point. As an alternative to this slow imaging technique, in Section 3.3, we detail the technical realization of 2D THz-TDS photoconductive antenna arrays, while in Section 3.3, we discuss 2D electro-optic sampling (EOS) in the context of THz-TDS imaging.

2.2. THz Transmission, Reflection, and Conductivity Imaging

In THz-TDS measurements, both the amplitude and the phase of a THz waveform can be extracted. With appropriate numerical treatment, one can then obtain the complex refractive index using the Fresnel coefficients expressed in terms of the relevant material refractive indices. Consider, for example, an interface between media 1 and 2, each media characterized with its own complex refractive index $\tilde{n}_{1,2} = n_{1,2} - ik_{1,2}$. Assuming that a THz parallel beam is transiting from media 1 into media 2, then the corresponding transmission and reflection coefficients can be written as

$$\begin{aligned} \text{Transmission coefficient} \quad & t_{12} = \frac{2\tilde{n}_1}{\tilde{n}_1 + \tilde{n}_2}, \\ \text{Reflection coefficient} \quad & r_{12} = \frac{\tilde{n}_1 - \tilde{n}_2}{\tilde{n}_1 + \tilde{n}_2}. \end{aligned} \tag{1}$$

By fitting experimentally measured transmission and refraction coefficients with the corresponding analytical expressions [Eqs. (1)], one can extract the material complex refractive indices, thus opening a way for direct imaging of the material refractive index distribution across the sample. In this example, we assume a collimated THz beam, while classical imaging is normally done via point-by-point raster scanning with a THz beam focused at the plane of a sample. In that case, one can still use the method described above; however, expressions for the Fresnel coefficients have to be somewhat modified to account for the non-planar wavefront of the probing beam [81,82].

In the following subsections, we detail several common imaging modalities that allow imaging complex refractive index distribution at the interface between dissimilar media: THz transmission, reflection, and conductivity imaging.

2.2a. Transmission Spectroscopy

First, we present a more in-depth review on interpreting complex transmission data to extract the sample complex refractive index. In what follows, we suppose a collimated THz beam, while, as mentioned earlier, the same algorithm with minor modifications can also be used in the case of focused THz beams for point-by-point imaging. Following [83], consider a sample in the form of a plate of thickness L (media 2) and complex refractive index $\tilde{n}_2$, located between two media, media 1 and 3, having complex refractive indices $\tilde{n}_1$ and $\tilde{n}_3$, respectively. In what follows we assume normal incidence of the probing THz wave [Fig. 6(a)]. To obtain the normalized transmission function $S_t(\omega)$ for a collimated THz beam, one performs two measurements: one is THz transmission through the sample $E_s(\omega)$, while another (reference measurement) is THz transmission through an empty system (sample removed and replaced with media 1) $E_{\text{ref}}(\omega)$. Then, the normalized transmission function at the angular frequency ω can be written as

$$S_t(\omega) = \frac{E_s(\omega)}{E_{\text{ref}}(\omega)} = \frac{t_{12}t_{23}\,\exp\left(\frac{i\tilde{n}_2\omega L}{c}\right)}{t_{13}\,\exp\left(\frac{i\tilde{n}_1\omega L}{c}\right)} \cdot \text{FP}(L,\omega) = \frac{2\tilde{n}_2(\tilde{n}_1+\tilde{n}_3)}{(\tilde{n}_1+\tilde{n}_2)(\tilde{n}_2+\tilde{n}_3)} \cdot \exp\left[i(\tilde{n}_2-\tilde{n}_1)\frac{\omega L}{c}\right] \cdot \text{FP}(L,\omega), \tag{2}$$

where

$$\text{FP}(L,\omega) = \sum_{k=0}^{\infty}\left[r_{23}r_{21}\,\exp\left(\frac{i2\tilde{n}_2\omega L}{c}\right)\right]^k = \frac{1}{1-\left(\frac{\tilde{n}_2-\tilde{n}_1}{\tilde{n}_2+\tilde{n}_1}\right)\left(\frac{\tilde{n}_2-\tilde{n}_3}{\tilde{n}_2+\tilde{n}_3}\right)\cdot\exp\left(i2\tilde{n}_2\frac{\omega L}{c}\right)} \tag{3}$$

is the Fabry–Perot term that accounts for multiple reflections inside the sample. This term becomes important when characterizing thin films [84], but it can be neglected ($\text{FP}(L,\omega)=1$) if the sample under consideration is optically thick. In a THz-TDS measurement, a sample can be considered optically thick if the echoes (multiple reflections) are well separated in time, and only the directly transmitted wave ($k=0$ term in the sum of Eq. (3) is sampled during the time-domain measurement) [83]. Alternatively, a sample can be considered optically thick when the sample material loss is high enough, $2\cdot\text{Im}(\tilde{n}_2)\omega L/c \gg 1$, so that multiple reflected waves in Eqs. (3) are so small in amplitude that they can be disregarded. A generalization of Eq. (2) for non-normal incidence is provided in Ref. [85].

Several methods can be used to solve Eq. (2) [83,85,86–90]. For example, if the sample ($\tilde{n}_2=\tilde{n}=n-ik$) is in air ($\tilde{n}_1=\tilde{n}_3=\tilde{n}_{\text{air}}=1$) and if the Fabry–Perot term is neglected ($\text{FP}(L,\omega)=1$), Eq. (2) becomes

Figure 6

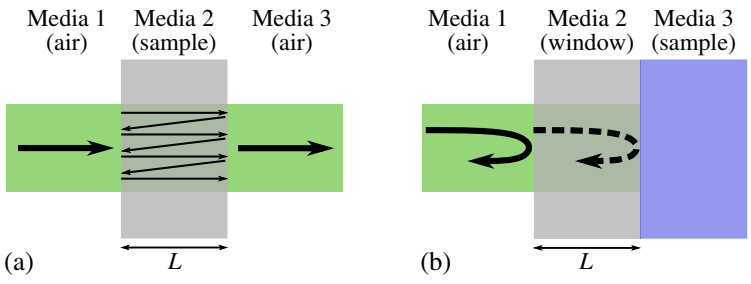

(a) Schematic of the transmission and (b) reflection setups for the experimental measurement of the transmission and reflection coefficients.

$$S_t(\omega) = \frac{4\tilde{n}}{(\tilde{n}+1)^2} \cdot \exp\left[-k\frac{\omega L}{c}\right] \exp\left[i(n-1)\frac{\omega L}{c}\right] \tag{4}$$

and can be rearranged to

$$n(\omega) = \frac{c}{\omega L}\left\{\arg\left[\frac{(\tilde{n}+1)^2}{4\tilde{n}} S_t(\omega)\right]\right\} + 1, \tag{5}$$

$$k(\omega) = -\frac{c}{\omega L}\ln\left[\left|\frac{(\tilde{n}+1)^2}{4\tilde{n}} S_t(\omega)\right|\right], \tag{6}$$

where $\arg(z)$ is the phase of the complex number z. A fixed-point algorithm can be used to get $n(\omega)$ and $k(\omega)$ [86,88,90]. In this algorithm, initial values of $n_0(\omega)$ and $k_0(\omega)$ are injected into Eqs. (5) and (6) to give new values of $n(\omega)$ and $k(\omega)$. By repeating this process iteratively, a fixed point is found, for which the values of $n(\omega)$ and $k(\omega)$ converge. As an initial guess for $n_0(\omega)$ and $k_0(\omega)$, one can assume that $4\tilde{n}/(\tilde{n}+1)^2 = 1$ [88]. Then,

$$n_0(\omega) = \frac{c}{\omega L}\{\arg[S(\omega)]\} + 1, \tag{7}$$

$$k_0(\omega) = -\frac{c}{\omega L}\ln[|S(\omega)|]. \tag{8}$$

This approximation becomes almost exact if the material losses are small, i.e., $k \ll n$ [91].

For optically thick samples, the cut-back method can also be used to measure the sample complex refractive index. This is an adaptation of the waveguide characterization technique detailed in Refs. [92–96], and it can also be applied to planar uniform samples. Within this method, transmission measurements are performed for two sample lengths, L_1 and L_2. The main advantage of this technique is that the complex refractive index can be analytically obtained without resorting to iterative algorithms. Indeed, assuming that Fabry–Perot terms do not contribute $\mathrm{FP}(L_1,\omega) = \mathrm{FP}(L_2,\omega) = 1$, the relative transmission function does not include any Fresnel coefficients:

$$\begin{aligned} S_t(\omega) &= \frac{E_2(\omega)}{E_1(\omega)} = \frac{t_{12}t_{23}\,\exp\left(\frac{i\tilde{n}\omega L_2}{c}\right)}{t_{12}t_{23}\,\exp\left(\frac{i\tilde{n}\omega L_1}{c}\right)} = \exp\left[i\frac{\tilde{n}\omega}{c}(L_2-L_1)\right] \\ &= \exp\left[-\frac{k\omega}{c}(L_2-L_1)\right]\exp\left[i\frac{n\omega}{c}(L_2-L_1)\right]. \end{aligned} \tag{9}$$

From this, the complex refractive index $\tilde{n} = n + ik$ can be computed analytically:

$$n(\omega) = \frac{c}{\omega(L_2-L_1)}\,\arg[S_t(\omega)], \tag{10}$$

$$k(\omega) = -\frac{c}{\omega(L_2-L_1)}\,\ln[|S_t(\omega)|]. \tag{11}$$

This method can be used to rapidly retrieve the complex refractive index without relying on iterative algorithms.

2.2b. Reflection Spectroscopy

Complementary to the transmission spectroscopy covered in the previous subsection, one can also interrogate materials in the reflection mode. In this subsection, we review interpretation of the complex reflection data to extract the sample complex refractive index. Thus, using analytical expressions for the generalized Fresnel coefficients [Eq. (1)], equations can be derived for the normalized reflection function, which depends on both the collimated THz beam polarization and incidence angle (see Ref. [97] for a comprehensive formulation).

A common experimental setup for reflection spectroscopy is depicted in Fig. 6(b). The sample under study (media 3) is placed behind a window of thickness L (media 2), which, in turn, is placed in air (media 1). As an example, we assume normal incidence of the THz beam, and we also assume that both THz emitter and detector are on the same side (transceiver configuration). This configuration, for example, was used to characterize liquids inside plastic bottles [97–101]. If the window is sufficiently thick, so that one could separate in time domain the traces coming from the air/window reflection $E_{\mathrm{ref}}(\omega)$ and the window/sample reflection $E_s(\omega)$, and if we can disregard the Fabry–Perot effect in the window, then the normalized reflection function can be written as

$$S_r(\omega) = \frac{E_s(\omega)}{E_{\mathrm{ref}}(\omega)} = \frac{t_{12}r_{23}t_{21}}{r_{12}} \exp\left(-\frac{i\tilde{n}_2\omega L}{c}\right) = \frac{4\tilde{n}_1\tilde{n}_2}{\tilde{n}_1^2 - \tilde{n}_2^2} \exp\left(-\frac{i\tilde{n}_2\omega L}{c}\right)\frac{\tilde{n}_2 - \tilde{n}_3}{\tilde{n}_2 + \tilde{n}_3}. \tag{12}$$

If we assume that media 1 is air ($\tilde{n}_1 = 1$) and media 2 is a window of a known refractive index ($\tilde{n}_2 = \tilde{n}_w$), Eq. (12) can be written as

$$C = \frac{E_s(\omega)}{E_{\mathrm{ref}}(\omega)}\frac{1 - \tilde{n}_w^2}{4\tilde{n}_w} \exp\left(\frac{i\tilde{n}_w\omega L}{c}\right) = \frac{\tilde{n}_w - \tilde{n}_3}{\tilde{n}_w + \tilde{n}_3}. \tag{13}$$

Then, $\tilde{n}_3(\omega)$ can be found analytically as

$$\tilde{n}_3(\omega) = \left[\frac{1 - C}{1 + C}\right]\tilde{n}_w(\omega). \tag{14}$$

When the sample is strongly absorbing, reflection geometry is clearly superior to the transmission spectroscopy as it does not rely on transmission through absorbing samples. Indeed, transmission spectroscopy is limited by the maximal dynamic range of the THz-TDS system, defined as the frequency-dependent maximal signal amplitude relative to the noise floor. When a sample is strongly absorbing, the noise floor is quickly reached for a short length of the sample. On the other hand, reflection spectroscopy does not rely on transmission through the sample, but rather on the amplitude and phase accuracy of the reflected signal. Therefore, the maximal absorbing coefficient depends on the SNR, defined as the average signal divided by its standard deviation [100,102]. For example, since liquid water is strongly absorbing in the THz spectral range, many biomedical applications of THz waves are performed in reflection geometry [14,103].

2.2c. Conductivity Imaging

In this subsection, we detail how to extract the electrical properties of a material from the complex refractive index. In many important physics problems, one needs to accurately determine the complex permittivity to electrically characterize a material. THz-TDS gives an almost direct experimental contactless measurement of the complex permittivity without resorting to the Kramers–Kronig relations, as is often done in Fourier-transform infrared spectroscopy (FTIR), for example. Indeed, from the refractive index calculated using the methods described in Sections 2.2a and 2.2b, the complex permittivity $\tilde{\varepsilon}(\omega)$ can be obtained with [104,105]

$$\begin{aligned}\tilde{\varepsilon}(\omega) &= \varepsilon_1(\omega) + i\varepsilon_2(\omega) = 1 + i\frac{\tilde{\sigma}}{\varepsilon_0\omega},\\ \varepsilon_1(\omega) &= n(\omega)^2 - k(\omega)^2,\\ \varepsilon_2(\omega) &= 2n(\omega)k(\omega).\end{aligned} \tag{15}$$

The complex permittivity is also related to the complex conductivity $\tilde{\sigma}(\omega)$ through $\tilde{\varepsilon}(\omega) = 1 + i\tilde{\sigma}(\omega)/\varepsilon_0\omega$, with ε_0 the vacuum permittivity. Therefore,

$$\begin{aligned}\tilde{\sigma}(\omega) &= \sigma_1(\omega) + i\sigma_2(\omega),\\ \sigma_1(\omega) &= \varepsilon_0\varepsilon_2(\omega)\omega,\\ \sigma_2(\omega) &= -[\varepsilon_1(\omega) - 1]\varepsilon_0\omega.\end{aligned} \tag{16}$$

Insights about the nature of the conductivity can be obtained by fitting the frequency-dependent conductivity with a conductivity model. For example, in the Drude model, the conductivity can be fitted to

$$\tilde{\sigma}(\omega) = \frac{\sigma_{\mathrm{DC}}}{1 - i\omega\tau}, \quad \sigma_{\mathrm{DC}} = ne\mu = \frac{ne^2\tau}{m} = \varepsilon_0\omega_p^2\tau, \tag{17}$$

where n is the charge-carrier density, e the elementary charge, μ the mobility, m the mass of the carrier, τ the Drude scattering time, and ω_p the plasma frequency.

Furthermore, the THz pulse can provide insights into the charge-carrier dynamics at the picosecond time scale. Time-resolved THz spectroscopy (TRTS), also known as optical-pump–THz-probe spectroscopy, is a technique derived from THz-TDS in which an optical pump is used to photoexcite the charge carrier in a material under study. By using an optical delay line, the transient conductivity is then probed with the THz pulse. This method is often used to study conductive materials [104–108]. In Section 2.5b, we will see an application of this method in the context of THz near-field imaging.

As an example of THz conductivity imaging, we now discuss contactless mapping of the electrical properties of graphene using THz-TDS. Graphene is a unique bidimensional material with many extraordinary properties that has attracted significant attention due to its potential applications in many fundamental and applied fields [109–111]. With the upcoming integration of graphene into a variety of commercial products comes the need for a rapid, non-destructive, and accurate electrical characterization of this material on an industrial scale [112]. In this context, THz-TDS offers a contactless solution to such a need [113–116].

In Ref. [112], Bøggild *et al.* presented a comparative analysis of three techniques for large-area mapping of the graphene electrical properties. The dry laser lithography first transforms a graphene wafer into multiple electrode devices in 1–2 h before using an automated probe station to extract the relevant parameters using the field-effect or Hall-effect measurement (minutes per measurement point). The need to pattern individual electrode devices makes this method destructive by nature. The micro four-point probes (M4PP) use metal-coated silicon microcantilevers to scan across the graphene sheet and obtain the electrical properties using the field-effect measurement (∼1 min per measurement point). This technique is non-destructive since it requires no sample preparation. However, contamination can occur because the tips and the graphene sheet are in contact. In comparison, THz-TDS imaging is non-contact and non-destructive. Furthermore, the acquisition time for a measurement point is limited by the mechanical scanning speed of the detector and the need to use an optical delay line to sample the temporal dimension (∼millisecond per measurement point).

In Ref. [117], Buron *et al.* demonstrated the conductance mapping of graphene with THz-TDS. Large-area graphene thin films were first grown using the chemical vapor deposition technique, before being transferred onto silicon substrates [Fig. 7(a)]. Then, the prepared samples were scanned in transmission geometry using a focused THz beam. By using the Fresnel coefficient in transmission geometry, the complex conductance could be determined in the thin film limit. The conductance was found to be virtually constant across the whole THz range, with an imaginary part close to zero and a real part near its DC value [Fig. 7(b)]. The real part of the conductance was (0.768 ± 0.077) mS comparable to (0.64 ± 0.13) mS measured with a contact-based M4PP. Next, to demonstrate nonuniform imaging, a damaged graphene sample [photograph in Fig. 7(c)] was imaged using THz-TDS [see Fig. 7(d)]. Again, the sheet conductance results agree with the M4PP measurement in Fig. 7(e). In Ref. [118], the same group used a gate voltage on the graphene sheet to map the carrier mobility, while in Ref. [119] the carrier mobility, carrier density and carrier scattering time were obtained by fitting the Drude model to the conductance spectra.

In general, the challenges of real-time THz spectroscopy and conductivity imaging are similar to those of the THz-TDS imaging system. To speed up image acquisition, the spectrum needs to be rapidly obtained using a fast optical delay line (see Section 3.2) and the detector needs to be a 2D array (see Sections 3.3 and 3.4). Furthermore, to determine the complex refractive index, one may need to use iterative algorithms, which can be problematic for real-time operation. However, in some cases, analytical solutions can be found. For example, in transmission spectroscopy, if the material losses are small (i.e., $k \ll n$), Eqs. (7) and (8) can be directly used, while the cut-back method provides an analytical solution [Eqs. (10) and (11)]. As for conductivity imaging, similar iterative algorithms must be used to obtain acceptable fits of the frequency-dependent permittivity with conductivity models. Ideally, the calculation times could be improved by using graphical processing units (GPUs).

Figure 7

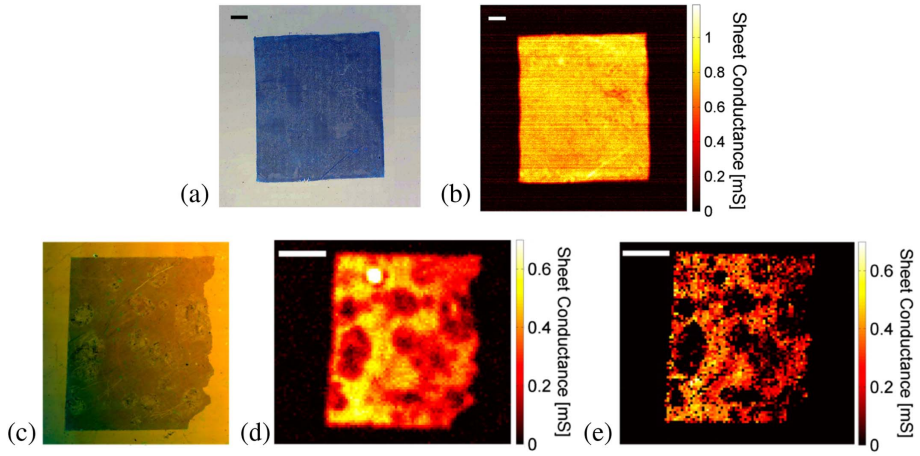

(a) Photograph of the graphene sheet and (b) corresponding sheet conductance map obtained using THz-TDS. (c) Damaged graphene sheet and (d) corresponding conductance mapped using THz-TDS and (e) M4PP. Reprinted with permission from Buron *et al.*, Nano Lett. **12**, 5074–5081 (2012) [117]. Copyright 2012 American Chemical Society.

2.3. THz Pulsed Imaging

THz pulsed imaging (TPI) also known as THz time-of-flight imaging (TOF) refers to mapping the arrival times of the THz pulses to the detector. The measurement is performed in reflection geometry using a THz-TDS configuration. The temporal delay between the reflected pulses reveals the internal structure of the sample.

Already in the early days of THz imaging, TPI was demonstrated by imaging the internal structure of a 3.5 inch floppy disk [120]. In a TOF measurement, the optical path travelled by the pulse is directly related to the pulse temporal delay Δt. Assuming a constant refractive index n over the relevant THz frequency range (associated with the pulse Fourier transform), one can use the time delay between the pulse reflected by the sample surface and the pulse reflected by the sample internal interface to measure the distance d from the sample surface to such internal interface:

$$d = \frac{c\Delta t}{2n}. \tag{18}$$

One of the practical applications of the TPI technique was demonstrated in the pharmaceutical industry [12,121–123]. There, an important problem is quality control of medicinal tablet coatings during their fabrication. Unlike in the visible/infrared regions of the spectrum, the majority of dry tablets are semi-transparent to THz radiation, thus enabling non-destructive imaging at high penetration depth [124,125]. In [126], for example, May *et al.* developed an inline sensor to monitor the tablet coating thickness in real time. The THz radiation was focused on a commercial perforated tablet coater [Figs. 8(a)–8(c)]. With a prior knowledge of the coating refractive index, Eq. (18) was used to measure the tablet coating thickness during the coating process [Fig. 8(d)]. The general concept behind TPI was also used to assess the hardness,

Figure 8

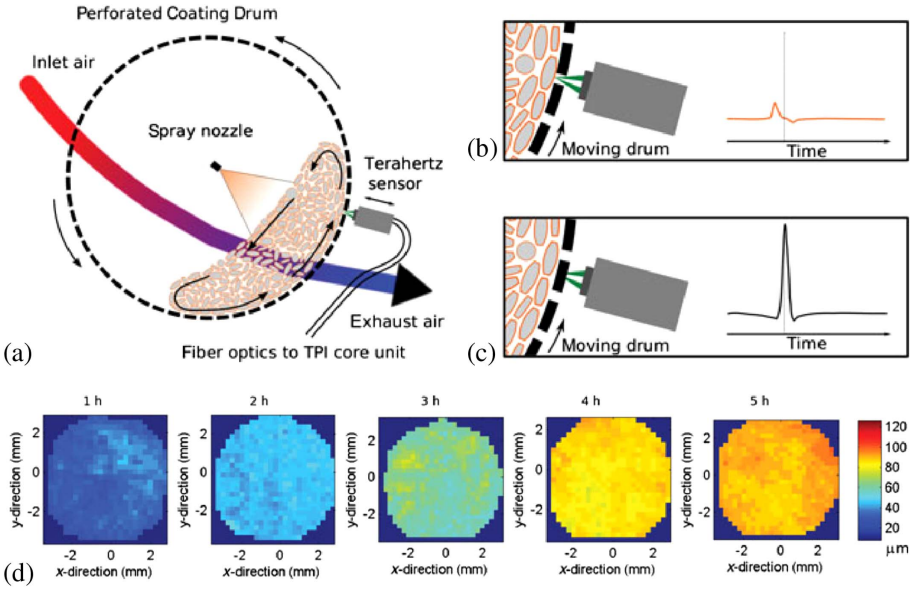

(a) Schematic of the tablet coating monitoring using THz-TDS in reflection geometry. (b) Time-domain measurement of the coating thickness and (c) reference measurement. (d) TPI of a tablet during the coating process and corresponding thickness evaluation. Reprinted from J. Pharm. Sci. **100**, May *et al.*, "Terahertz in-line sensor for direct coating thickness measurement of individual tablets during film coating in real-time," 1535–1544 (2011) [126]. Copyright 2011, with permission from Elsevier.

density, [127] and porosity [128] of the pharmaceutical tablets, as well as thickness uniformity of automobile exterior coatings [129].

Moreover, in the field of art conservation, TPI was used as a non-destructive method to study the paint layers of ancient masterpieces [23,130–133]. Thus, in Ref. [134], by using TPI in reflection mode, a hidden portrait has been revealed in an 18th century easel painting by the Danish painter Nicolai Abildgaard. While the visible image portrays an old woman [Fig. 9(a)], the x-ray image revealed a portrait of a man underneath the top paint layer [Fig. 9(b)]. However, x-ray radiation, due to its ionizing property, can be hazardous to paint and it can compromise radiometric dating. Moreover, while x-ray essentially probes the losses in the paint, TPI can provide supplementary information, such as the paint thickness.

To create a THz image, the authors first deconvoluted the reflected THz signal using a plane metal surface placed at the position of the paint as a reference. Various paint layers were then identified by looking for the distinct reflected pulses in the time-domain data [Fig. 9(c)]. Additionally, the authors used spectral integration over certain frequency ranges to reveal various details of the internal painting:

$$M = \int_{\nu_1}^{\nu_2} |\mathrm{FFT}(E(t_1 < t < t_0)|\mathrm{d}\nu, \tag{19}$$

where the time intervals t_0 and t_1 correspond to the beginning and the end (in time domain) of a particular reflected pulse. For example, by integrating over the whole frequency range for the reflected pulse that defines the second paint layer, they observed the hidden portrait [Fig. 9(d)], while by integrating over the 0.55–0.62 THz

Figure 9

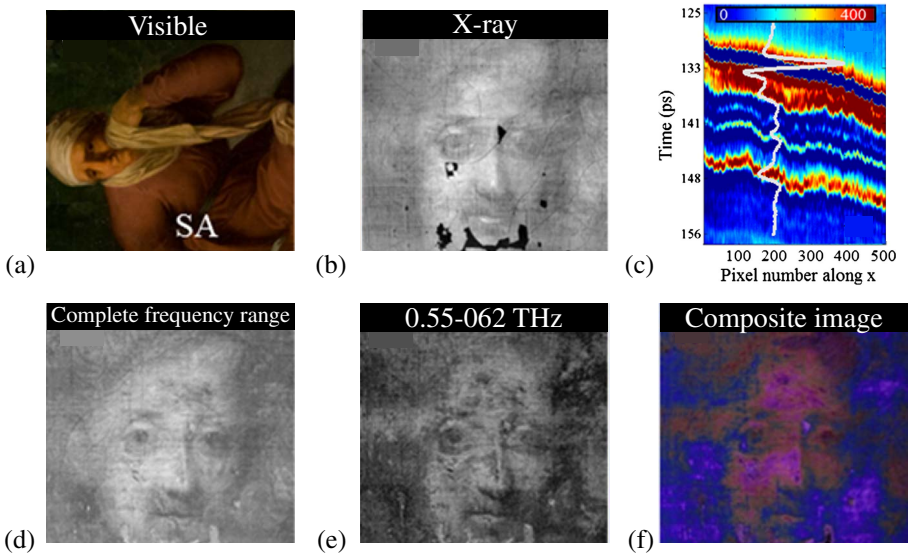

(a) Visible image of the painting. (b) X-ray image reveals the hidden paint. (c) Time-domain data shows several distinct layers of paint. (d) THz image obtained by integrating over the full frequency range of the reflected pulse that defines the second paint layer. (e) THz image as in (d) but with spectral data integrated over the 0.55–0.62 THz range. It reveals sharper details around the mouth and the nose. (f) THz false color image obtained by superimposing various frequency-averaged images (blue, 0.22–0.36 THz; red, 0.36–048 THz; and green, 0.48–055 THz). It reveals that several distinct pigments have been used in the painting. Adapted with permission from [134].

range, finer details were observed around the nose and the mouth of the subject [Fig. 9(e)]. In Fig. 9(f), a false color image was realized by superimposing various frequency-averaged THz images obtained using different frequency integration intervals. The color differences in the composite image can be interpreted by noting that different paint pigments have distinct spectral optical properties.

In Ref. [135], TPI imaging was combined with computational imaging techniques to extract, in a fully automated manner, information about the sample layered structure. In particular, by using a THz-TDS setup in reflection geometry [Fig. 10(a)], Redo-Sanchez *et al.* demonstrated an automatized reading of the roman characters written on pages pressed together to mimic a closed book [Figs. 10(b) and 10(c)]. First, using a -probabilistic pulse extraction (PPEX) algorithm developed by the authors, they identified the presence of different pages by recognizing (numbering) the temporal intervals containing distinct reflected THz pulses [Fig. 10(d)]. Next, they performed Fourier transforms of the individual reflected pulses in order to obtain spectrally resolved images of distinct pages. To select the frequency image with the highest contrast, they analyzed the kurtosis of the pixel intensity histograms, assuming that kurtosis is higher for higher image contrasts [Figs. 10(e) and 10(f)]. In those selected images, the characters can then be easily recognized in the first paper layers, but the character recognition becomes challenging as the depth increases due to decreased contrast and the presence of phantom images from other layers. To address this issue, the authors used a convex cardinal shape composition (CCSC) optimization algorithm [136] to automatically recognize the letters. The CCSC algorithm works essentially by comparing the regions of high intensity to a set of letters at different positions and orientations.

As for real-time imaging using the TPI technique, the optical delay line is a crucial component (see Section 3.2) in such systems, since the method relies on the detection of the reflected echoes obtained in the temporal data of the THz-TDS system. Furthermore, to speed acquisition, 2D arrays can be used to avoid mechanical movement of the sample (Sections 3.3 and 3.4). Alternatively, single-pixel detection combined with compressive sensing techniques can be employed (see Ref. [137] and Section 4.2a). Moreover, TPI measurements usually involve multiple reflections for a sample with multiple layers. Therefore, manual intervention is necessary to identify the temporal intervals corresponding to the distinct reflected echoes. To avoid human involvement in the data acquisition process and to speed up the image construction, artificial intelligence or other algorithms can be developed to automatically distinguish the temporal intervals (see, for example, the PPEX algorithm detailed in Ref. [135]).

2.4. THz Computed Tomography

Since many materials are relatively transparent to THz radiation, developing 3D THz imaging modalities that can reveal the material's internal structure constitutes an active research field. Extensive reviews of various reconstruction methods for 3D imaging are provided in [77,138,139]. As an example, here we detail the THz computed tomography (THz-CT) technique. First demonstrated in the THz spectral range in Refs. [140,141], the technique derives from the x-ray CT commonly used in the biomedical field.

A typical setup for THz-CT is presented in Fig. 11(a). A parallel THz beam is incident onto a sample having, for example, local optical losses distributed according to $\alpha(x, y)$. Here, we define an auxiliary function $f(x, y) = -\alpha(x, y)$, where (x, y) are the coordinates in the local coordinate system associated with the sample. A sample is then placed onto a rotational stage with an instant position characterized by the rotation

angle θ. The sample is then rotated, while the detector (or the sample) is moved along a fixed line by distance t to construct the sinogram $P(\theta, t)$ [Fig. 11(b)]. In this particular example, the auxiliary function $P(\theta, t)$ is defined as the natural logarithm of the measured THz intensity distribution $P(\theta, t) = \ln(I(\theta, t))$. Therefore, in this example,

Figure 10

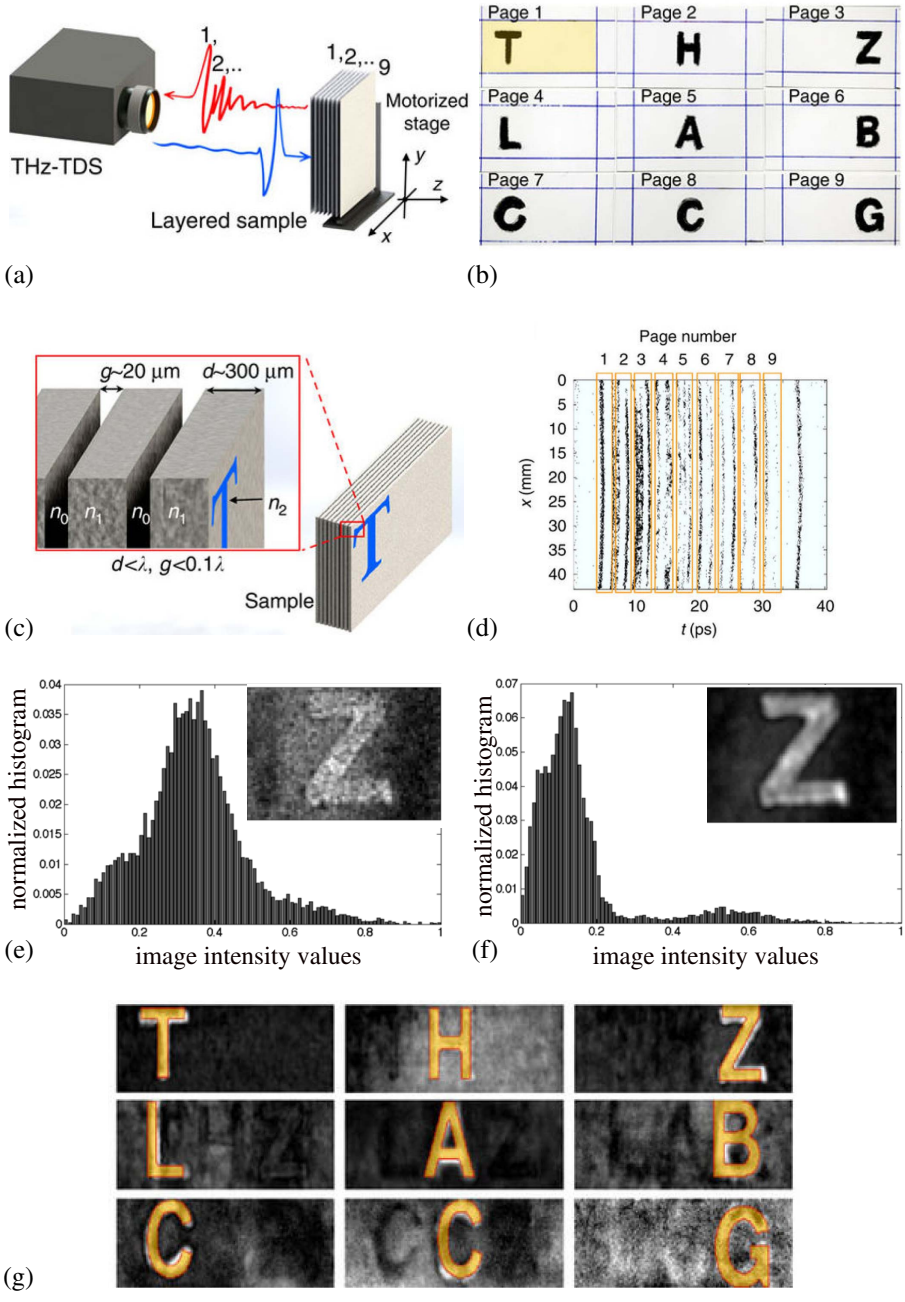

(a) Experimental setup featuring a THz-TDS setup in reflection mode. (b) Images of different pages in the visible spectral range and (c) schematic of the book pages. (d) Page number identification using the PPEX algorithm. (e) Pixel intensity histogram for a THz frequency image with a low kurtosis and (f) a high kurtosis. (g) Automatic character recognition by using the CCSC optimization algorithm. Adapted from [135] under the terms of the Creative Commons Attribution 4.0 License. With copyright permission.

the sinogram physically corresponds to some measure of the cumulative optical loss due to transmission through the sample along a certain straight line $L(\theta, t)$ defined by the stage rotation angle and the detector position [142]:

$$P(\theta, t) = \int_{L(\theta,t)} f(x, y)\mathrm{d}l. \tag{20}$$

The mathematical operation in Eq. (20) is known as the Radon transform. It corresponds to the line integral over $L(\theta, t)$. The detector or sample is moved laterally (variable t) and rotated (variable θ) and the sinogram $P(\theta, t)$ is measured. Therefore, to reconstruct the original object $f(x, y)$ (for example the optical loss distribution), the inverse Radon transform is computed through the filtered back-projection (FBP) algorithm [143] or using iterative algorithms, such as the simultaneous algebraic reconstruction technique (SART) and the ordered subsets expectations maximization (OSEM) [144].

In Ref. [142], Brahm *et al.* used the broadband information provided by THz-TDS to identify chemical contents. A sample made of glucose and lactose in a polystyrene holder [Fig. 11(c)] was measured at different angles. To create the sinogram, the measurements were normalized by reference measurements of lactose and glucose. In the resulting sinogram, the amplitude values varied between -1 and $+1$ to indicate the presence of lactose and glucose, respectively [Fig. 11(d)]. Then, the FPB algorithm was used to reconstruct the slice of the object [Fig. 11(e)]. In [145], the identification and localization were refined by using a wavelet-based method.

THz-CT measures a slice of the object. To obtain the information about the third dimension, instead of measuring along a unidimensional line [axis t is Fig. 11(a)],

Figure 11

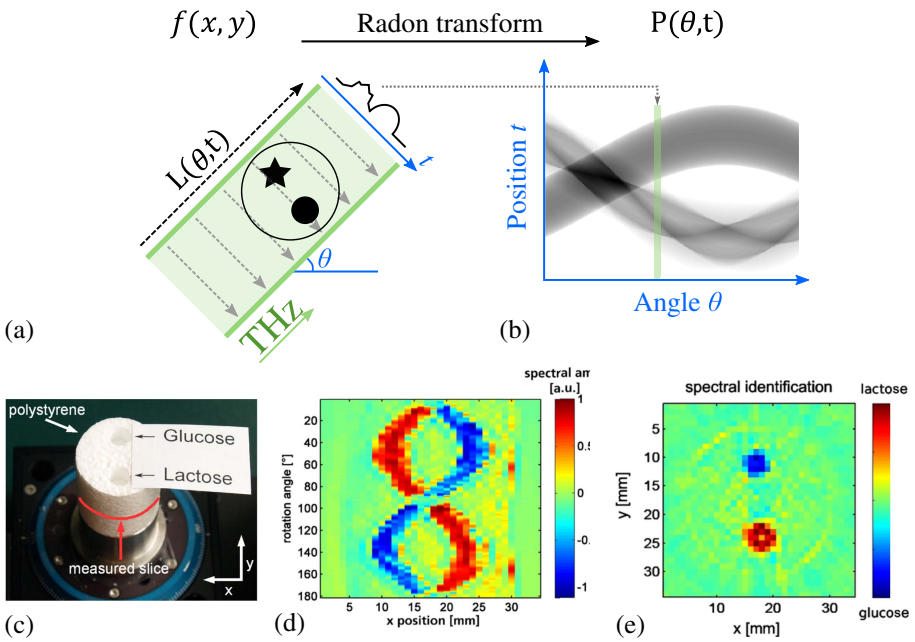

(a) THz-CT in the transmission geometry. (b) A typical sinogram from THz-CT. (c) Photograph of the sample with glucose and lactose, (d) corresponding sinogram, and (e) reconstructed material's distribution of the slice in (c). Reprinted with permission from Brahm *et al.*, Appl. Phys. B **100**, 151–158 (2010) [142]. Copyright 2010 AIP Publishing LLC.

a 2D image per angle θ must be acquired. In Ref. [146], Bessou *et al.* performed THz-CT on dried human bones. In Figs. 12(a)–12(c), a photograph, an x-ray radiograph, and a THz transmission image of a right human coxal bone are presented. As can be seen from Fig. 12(b), the wing of the ilium is transparent to the x rays, while the inferior part is opaque. The THz image [Fig. 12(c)] presents similar characteristics despite a lower spatial resolution. In Fig. 12(d), angular slices of the reconstructed bone are presented, while the 3D reconstruction is shown in Fig. 12(e).

In x-ray CT, since the relative size of the wavelength (~nanometers) is much smaller than that of the object (~millimeters), one can ignore the illuminating beam self-diffraction and consider it strictly parallel. On the other hand, in THz-CT, the beam size is limited by the size of the focusing optics, which is typically no larger than ~10 cm in diameter, while the wavelength of THz light can be as large as several millimeters. Thus, in the THz regime, parallel beam approximation might not be adequate and should be replaced by a Gaussian beam approximation. To obtain better reconstructions, the Gaussian beam intensity profile was introduced into the propagation model in Ref. [147]. In Ref. [148], a statistical reconstruction method called maximum likelihood for transmission (ML-TR) initially developed for x-ray CT was modified to include the Gaussian beam propagation. Alternatively, a nondiffractive

Figure 12

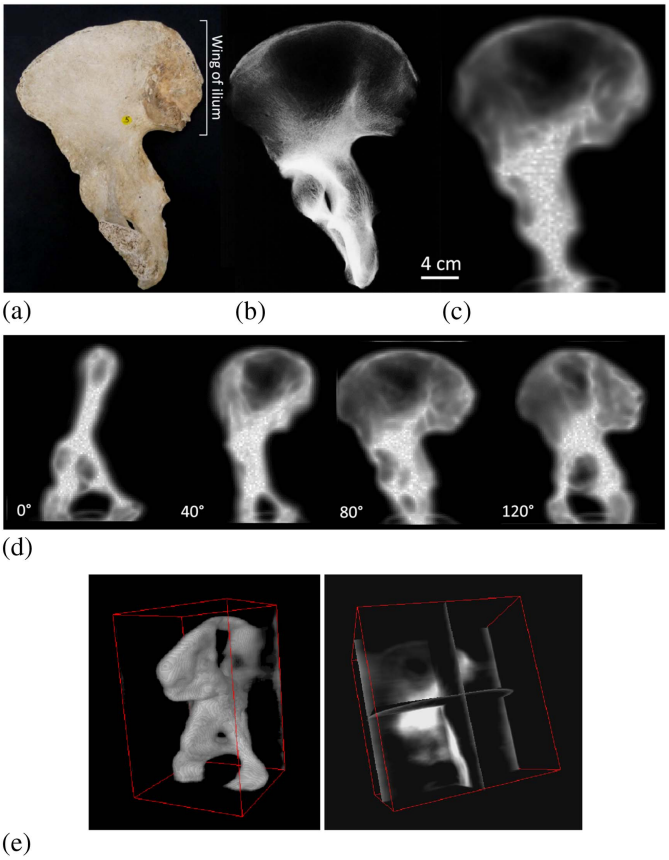

(a) Photograph, (b) x-ray, and (c) THz transmission image of a dried right human coxal bone. (d) THz-CT for four different orientations of the bone. (e) 3D reconstruction and (f) internal structure revealed by THz-CT. Reprinted with permission from [146]. Copyright 2012 Optical Society of America.

Bessel THz beam was shown to improve the quality of the reconstruction in Ref. [149].

Furthermore, while in x-ray CT, only the absorption losses are measured, in THz-CT, reflection and refraction losses become important for non-uniform samples with large refractive index. In Ref. [150], Abraham *et al.* used a multipeak averaging procedure coupled to the algorithm to reduce the effect of the refraction losses on image quality, while in Refs. [151,152], the Fresnel reflection and refraction losses were evaluated and eliminated using a ray-tracing method. Among successful applications of THz-CT, we note in particular, a study of the internal content of a 18th Dynasty Egyptian sealed pottery reported in Refs. [153–155]. In Ref. [156], polymer additive manufacturing objects from the aerospace and medical industries were successfully imaged in 3D using THz-CT.

Real-time THz-CT is particularly challenging since a third dimension (the angular rotation of the sample) must be measured. However, THz-CT does not require the time-domain/spectral information to reconstruct an object's internal structure. In fact, schemes involving only the transmitted amplitude/intensity THz radiation can be used. For example, in Ref. [157], silicon-based CMOS emitter and detector were used at a frequency of 490 GHz. Other CW THz-CT works involved the use of a double-heterojunction bipolar transistor at 350 and 650 GHz [158], a gas laser at 2.52 THz [159], a superconducting intrinsic Josephson junction oscillator at 440 GHz [160], and injection-seeded parametric emitter and detector [161]. This opens the possibility of using THz cameras (Section 4) to simultaneously obtain two spatial dimensions. For example, in Ref. [162], a pyroelectric camera was used to obtain a 3D image of a straw. Furthermore, if one uses THz-TDS for THz-CT, in addition to the need of array detectors (Section 3.3 and 3.4), one also needs to use fast optical delay lines (Section 3.2). In particular, in Section 3.4b, we review the work of Jewariya *et al.* [163] who demonstrated THz-CT acquisition in only 6 min using EOS and a CCD camera. Finally, if one wants to avoid the use of array detectors, a single-pixel detector can also be used for THz-CT, either with fast beam-steering optics [164] or with compressive sensing [165] (Sections 5.1a and 5.2a).

2.5. THz Near-Field Imaging

The imaging systems that we have discussed so far operate in the far-field regime, and, thus, feature resolutions that are limited by diffraction of the THz beam on the elements of the optical system. For example, light from a point source positioned near the microscope objective focal plane and passing through a circular lens produces a diffraction pattern in the shape of concentric rings (Airy disk). The spatial resolution in the object plane is generally defined using the Rayleigh criterion [166], where the minimal resolvable feature δx is defined as the minimal distance between a point source central maximum and the second point source first minimum. This can be written as

$$\delta x = 1.22\frac{\lambda F}{D}, \tag{21}$$

where F and D are the focal length and diameter of the lens, respectively. This corresponds to the size, in the object plane, of the smallest object that the lens can resolve and also the radius of the smallest spot to which a collimated beam of light can be focused. Therefore, according to Eq. (21), the smallest resolvable feature is normally comparable to or larger than the wavelength of the THz light.

To resolve the object's subwavelength features, one needs to detect the evanescent fields, which exist only at short distances from the object (near-field region). This

type of imaging is known as THz near-field imaging. Prior reviews of this topic are found in Refs. [167–170]. Several techniques have been explored to enable subwavelength THz imaging. In the following, we first briefly overview some recent subwavelength imaging techniques, before focusing on two major types of techniques that have attracted the most attention in the literature, namely, aperture-based and scattering-based near-field imaging.

The confocal THz near-field imaging technique, as its name suggests, derives from the confocal microscopy at optical wavelengths. It consists of using a pair of apertures (pinholes) that act as spatial filters to block THz radiation propagating outside the cone of light, thus resulting in increased lateral and depth resolution [171–174]. For example, in Ref. [173], using a quantum cascade laser at 2.9 THz, the authors demonstrated lateral and axial resolutions of 70 μm ($\lambda/1.4$) and 400 μm. In Ref. [174], medieval manuscripts were imaged with confocal THz imaging at 0.3 THz with a lateral resolution of 0.5 mm ($\lambda/2$). In confocal microscopy, the lateral resolution is improved by reducing the pinhole diameter. However, the diameter cannot be reduced below a certain threshold for which no signal is collected at all, therefore requiring powerful sources.

In comparison, the solid-lens immersion approach allows for more throughput light intensities. The idea here is to use a specially designed lens that generates a spot size smaller than the diffraction limit in the evanescent field region following the lens. For example, the lens can be a cube [175,176] or a sphere [177]. In Ref. [178], a combination of an aspheric lens and a truncated sphere was used to achieve a resolution of $\lambda/3.1$ (at 0.5 THz), better than the resolution of an aspheric lens alone ($\lambda/1.2$). In this case, however, the spatial resolution (although subwavelength) is fundamentally limited by the material properties of the immersion lens (specifically its refractive index). In Ref. [179], a similar setup was used to image soft biological tissues with a resolution of $\lambda/6.7$ at 0.6 THz.

In the direct-contact method, the sample is placed in direct contact with a subwavelength detector. This approach is generally employed with EOS using THz-TDS (Section 3.1a). In this case, the detector is a femtosecond optical beam (the size of which is smaller than the THz wavelength) that probes the polarization change in a nonlinear crystal. The sample is then in direct contact with the crystal, leading to a direct measurement of the THz electric field in the near-field region. For example, in Ref. [180], Adam *et al.* demonstrated a 20 μm resolution by imaging various metal structures deposited onto an electro-optic GaP crystal. In Ref. [181], Seo *et al.* measured the 2D time-domain THz electric field behind the slit arrays, from which the magnetic and Poynting fields were reconstructed. Because of the possibility of using cameras operating in the visible/infrared range, the direct-contact EOS technique is a serious candidate for real-time near-field THz imaging. This will be reviewed in Section 3.4b. Very recently, an additional approach using SiGe heterojunction bipolar transistor technology has emerged for direct-contact near-field imaging [182]. Fabricated with 130 nm BiCMOS process technology, the sensor operating at 0.55 THz both generated and detected THz radiation. The close on-chip proximity of the emitter and the detector allowed the demonstration of a lateral resolution of 10–12 μm ($\lambda/55$).

Among other THz near-field imaging techniques, we note the deconvolution from the image of the point-spread function, mathematically modeled using the Gaussian beam theory and variables such as the beam divergence, depth of focus, and absorption coefficient of the object [183,184].

Realizing real-time near-field imaging is not trivial since most of the techniques rely on the mechanical scanning of subwavelength apertures/tips. Therefore, the parallel

acquisition of multiple images becomes difficult. In that context, the direct-contact THz near-field imaging technique distinguishes itself as it allows acquiring 2D images. Furthermore, spectroscopic features being rich at the subwavelength scale, there is great interest in combining THz-TDS with near-field THz imaging. This combination is realized in EOS with crystals and it is the subject of Section 3.4b.

2.5a. THz Aperture Near-Field Optical Microscopy

The most direct way of enabling a near-field imaging system is to use a subwavelength-size aperture in the near field. In the visible/infrared this approach is also known as scanning near-field optical microscopy (SNOM). The resolution of this method scales with the size of the aperture, however, the sensitivity of the method decreases rapidly (superlinearly) with smaller aperture sizes [185]. The aperture can also be a tapered metal cone tip [186], a dynamically moving aperture produced by optically pumping a semiconductor wafer [187]. We mention that, in principle, apertureless subwavelength dielectric probes can be designed using a solid immersion lens approach, which can provide much higher throughput light intensities than aperture-based methods [178]. In this case, however, the spatial resolution (although subwavelength) is fundamentally limited by the material properties of the immersion lens, which is not the case for aperture-based near-field imaging.

In more detail, in Ref. [185], the detector (a photoconductive antenna) was placed at a subwavelength distance from a near-field rectangular aperture probe to detect the exponentially decaying evanescent THz field [188]. In this arrangement, the spatial resolution is determined by the aperture size [189]; however, following Bethe's study of diffraction by a circular hole [190,191], the transmitted electric field decreases with the third power of the aperture size, thus rendering the transmission through deeply subwavelength apertures extremely small. To increase the optical transmission through subwavelength apertures, in Ref. [192], Ishihara *et al.* inscribed concentric periodic grooves onto a metallic substrate around the aperture. In this bull's-eye structure, the incident THz wave excites surface waves that increase the electric field values in the subwavelength aperture 20-fold. In Ref. [193], the circular aperture was replaced by a bow-tie aperture to increase the transmission by 3 and enable a resolution of 12 μm ($\lambda/17$ at 1.45 THz).

Recently, the near-field probe and the THz photoconductive antenna were integrated on a single-chip. In Ref. [194], Macfaden *et al.* placed the aperture probe at a 1 μm distance from the THz antenna, which resulted in a sub-1-μm thickness of the GaAs semiconductor active layer, which is a key enabling element of the antenna. The problem with such a small thickness of the GaAs layer is that it is much smaller than the characteristic optical absorption length (1.4 μm) at the wavelength (800 nm) used for photoexcitation (infrared pump beam) of the antenna. This means that few charge carriers are generated by the pump beam within the GaAs layer of the PCA and, consequently, sensitivity of the THz detection is reduced. To increase the detection efficiency, the authors introduced a distributed Bragg reflector between the semiconductor layer and the subwavelength aperture [Fig. 13(a)]. The purpose of this reflector was twofold. First, it behaved as a resonator that enhanced the optical field of the pumping infrared beam at the position of the antenna gap. Second, it provided optical isolation of the sample under study from the pumping optical pulse, which is important when imaging light-sensitive materials such as semiconductors. As a result, with the integrated chip, a spatial resolution of 3 μm ($\lambda/100$ at 1 THz) was demonstrated. In Ref. 195], to increase the sensitivity of the antenna even further, a gold nanoantenna array was added in the vicinity of the active layer of the antenna [Fig. 13(b)]. The array was designed to have a plasmonic resonance at 800 nm

and the experimental spectra showed that 80% of the pump light was absorbed. With this structure, a spatial resolution of 2 μm was demonstrated ($\lambda/150$ at 1 THz).

2.5b. THz Scattering Near-Field Optical Microscopy

A second class of THz near-field systems is known as THz scattering near-field optical microscopy. In those systems, the THz radiation is focused on a metallic tip that confines strongly the THz radiation in a small region. When brought close to a sample, the tip scatters in the far field the THz radiation that has interacted with the sample in the near field. To distinguish the scattered field from the background noise, the tip is mechanically modulated at a certain fixed frequency that enables THz detection with a lock-in amplifier.

In the early demonstrations of the scattering-type THz near-field imaging, spatial resolutions of 18 μm ($\lambda/110$ at 0.15 THz) [196] and 150 nm ($\lambda/1000$ at 2 THz) [197] were achieved. Those resolutions were essentially determined by the size of the tip apex. One of the main advantages of the scattering-type THz near-field imaging is that the THz system can be coupled with existing imaging techniques that use vibrating probing tips. For example, in Ref. [198], THz illumination and detection were combined with the vibrating cantilever of an atomic force microscope (AFM) to map the charge-carrier concentration of a transistor at the nanometer scale with 40 nm resolution ($\lambda/3000$ at 2.54 THz).

Laser THz emission microscopy (LTEM) is a near-field imaging technique initially proposed for non-destructive inspection of electrical failures in circuits [199]. Within this method, upon femtosecond illumination of a sample, charge carriers are accelerated, and THz pulses are emitted. In LTEM, the spatial resolution is determined by the femtosecond pulse spot size, leading to a spatial resolution of 3 μm ($\lambda/2000$ at 0.05 THz) in Ref. [199]. Very recently, nanoscale LTEM was proposed by focusing

Figure 13

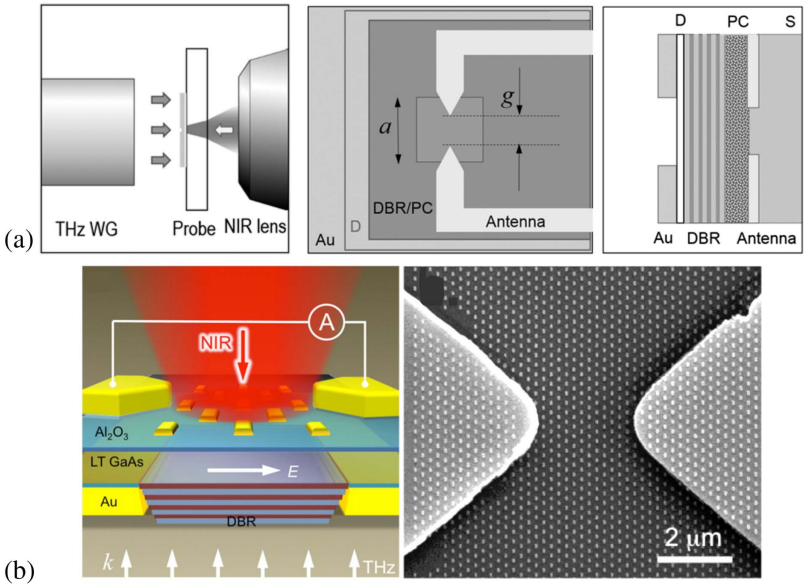

(a) Integrated subwavelength aperture/THz-PCA in a single chip separated by a distributed Bragg reflector. Adapted from Macfaden *et al.*, Appl. Phys. Lett. **104**, 01110 (2014) [194]. Copyright 2014 AIP Publishing LLC. (b) Integrated chip enhanced with a plasmonic nanoarray. Adapted with permission from Mitrofanov *et al.*, ACS Photon **2**, 1763–1768 (2015) [195]. Copyright 2015 American Chemical Society.

the infrared femtosecond pulse on a commercial AFM metal tip and a semiconductor substrate [200]. Dipole oscillations of the charges are the source of THz pulses in the region of the tip apex. Nanoscale imaging can then be performed by detecting the THz pulses that have interacted with a sample brought close to the metal tip. In [200], a tip-size-limited spatial resolution of 20 nm was achieved and allowed the THz imaging of a single gold nanorod.

In Ref. [201], THz-TDS was coupled to a scanning tunneling microscope (STM) to combine the nanometer spatial resolution of the STM with the subpicosecond time resolution of the THz-TDS. Without modifying the STM design, the THz pulse was focused onto the probe tip to produce a subpicosecond voltage transient that drove electrons across the junction [Fig. 14(a)]. Since the measured current is localized in the tunnel junction, the spatial resolution is defined by the size of the tip apex, which was measured to be 2 nm ($\lambda/150000$ at 1 THz) in Ref. [201]. To demonstrate the potential of the THz-STM in measuring ultrafast carrier dynamics, Cocker *et al.* [201] optically pumped a sample of InAs nanodots grown on GaAs. Then, they measured both the STM topography and the THz-STM images. By varying the time delay between the optical pulse and the THz pulse, clear contrast in the THz-STM images was observed [Fig. 14(b)]. In Ref. [202], by using THz-STM, the authors imaged the dynamics of the orbital structure of a pentacene molecule.

3. ENABLING REAL-TIME THZ-TDS IMAGING

Many of the imaging techniques we reviewed in Section 2 use the THz-TDS setup. In this section, we have a closer look at THz-TDS, as well as at various techniques that can speed up acquisition of the THz pulses and enable real-time imaging.

Figure 14

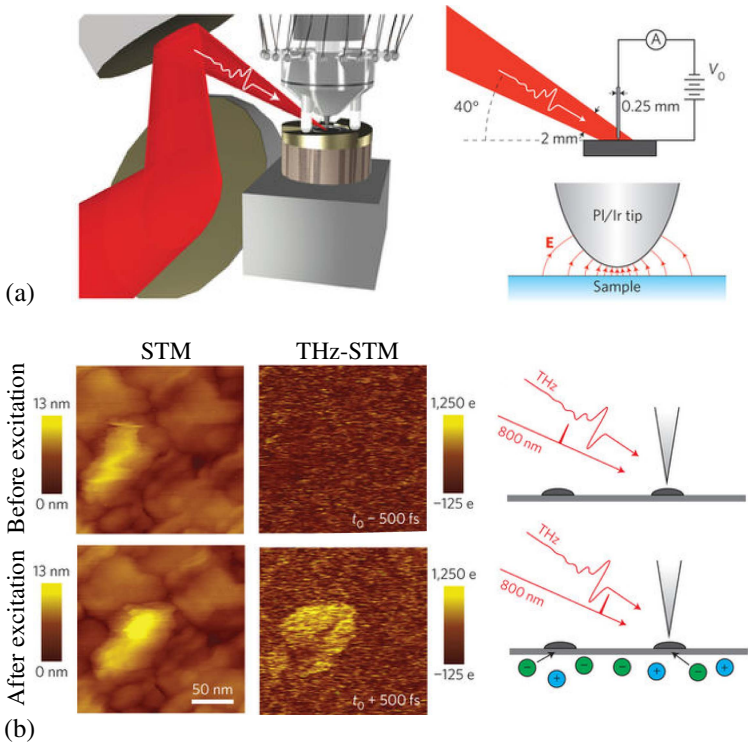

(a) Schematic of the THz-STM. (b) STM image, THz-STM image and schematic before and after optical excitation. Reprinted by permission from Macmillan Publishers Ltd.: Cocker *et al.*, Nat. Photonics **7**, 620–625 (2013) [201]. Copyright 2013.

Figure 15 depicts two classical experimental setups for THz-TDS in transmission and reflection modalities. An ultrafast laser beam is divided and sent along two optical paths. THz pulses are generated in the emission arm and then they travel to a sample placed at the focal plane of the focusing optics. After interacting with the sample, the THz pulses are coherently detected in the detection line arm, using an optical delay line to induce a temporal difference between the optical pump and the probe pulses.

There are two main methods to generate and detect THz pulses: (1) using photoconductive antennas (PCA) and (2) using optical rectification and EOS in nonlinear crystals. In this section, we begin by detailing the emission and detection principles using the abovementioned technologies (Section 3.1). For real-time imaging, the predominance of the relatively slow optical delay lines presents one of the main challenges. Therefore, in Section 3.2, we review several novel optical delay line designs that speed up pulse acquisition. Typically, both PCA and EOS are single-pixel detectors, which complicates the acquisition of high-resolution THz images. Therefore, in Section 3.3, we overview some of the recent works aimed at fabricating PCA arrays, while in Section 3.4, we detail the use of cameras to perform EOS.

3.1. Coherent THz Generation and Detection THz-TDS

3.1a. Photoconductive Antenna

A photoconductive antenna (PCA) can be used to generate and detect THz pulses [40–46]. The PCA is made of two metal electrodes deposited onto a semiconductor substrate. Photoexcited carriers are created in the gap between the electrodes by optical excitation (typically using ultrafast infrared pump laser beams). The PCA is essentially a photoswitch, where, for THz generation and detection, both the switch-on and switch-off times must be subpicosecond [203]. The switch-on is determined by the pump pulse duration of the optical excitation (typically <100 fs), while the switch-off time is dictated mainly by the carrier lifetime.

To generate THz, the antenna gap is voltage-biased and illuminated with a femtosecond laser pulse [Fig. 16(a)]. Excited photocarriers are then accelerated on a subpicosecond time scale. This rapid rise and fall of the transient photocurrent is the source of a THz electromagnetic field irradiated away from the antenna. The process of transient photocurrent switching can generate broadband THz pulses with bandwidths up to 15 THz [204], the limitation being the carrier lifetime. Recently, average THz power levels as high as 3.8 mW (with 240 mW optical pumping) were achieved, by using a large-area PCA with embedded plasmonic contact electrode gratings [205,206], while

Figure 15

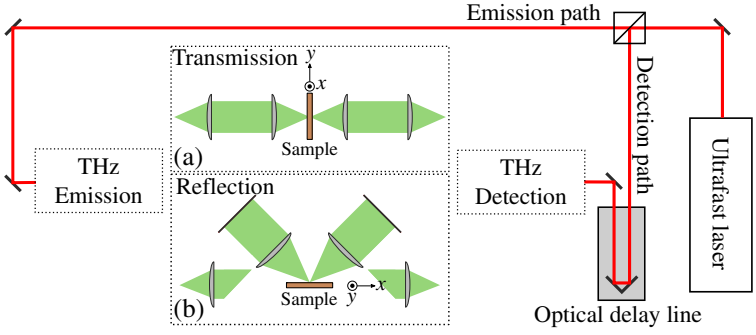

Schematic of a THz time-domain spectroscopy system in (a) transmission and (b) reflection geometries. The emission and detection hardware are described in Section 3.1.

most THz-TDS systems operate with THz pulses of ~1–100 μW average power. To improve the SNR, the emitter antenna is typically biased with an alternating voltage and lock-in amplification is used.

For THz detection, no bias voltage is applied between the electrodes [Fig. 16(b)], while the excited photocarriers are accelerated by the incoming THz radiation. This results in a time-varying photocurrent $J(\omega)$ between the antenna electrodes, which is proportional to the field amplitude of the THz radiation $E_{\mathrm{THz}}(\omega)$:

$$J(\omega) \propto [I(\omega)R(\omega)]E_{\mathrm{THz}}(\omega), \tag{22}$$

where $I(\omega)$ is the spectrum of the optical source, and $R(\omega)$ is the Fourier transform of the time response of the semiconductor photocarriers, which includes the trapping and recombination times [207,208]. The term $[I(\omega)R(\omega)]$ is the spectral sensitivity of the PCA, and it can be seen as a low-pass filter function applied to the incident THz pulse $E_{\mathrm{THz}}(\omega)$. Consequently, the detected THz bandwidth can be improved by pumping the PCA detector with temporarily shorter optical pulses (larger bandwidth) or by tuning the charge-carrier lifetimes. In Refs. [209,210], significant improvement in the THz detection sensitivity was reported by using nanostructured plasmonic contact electrodes that effectively reduce the average transport path length of the photocarriers. Consequently, an increased number of carriers reached the contact electrodes, leading to higher photocurrent and increased sensitivities.

Finally, we note that the classic PCA is a single-pixel detector, which is problematic for real-time high-resolution THz imaging due to the necessity of slow raster scanning of the sample. Recently, there were several reports of designing arrays of PCA detectors, which can be beneficial for imaging applications. We detail these advancements in Section 3.3.

3.1b. Optical Rectification and Electro-Optic Sampling

Optical rectification is a second-order nonlinear process commonly used to generate pulsed THz radiation [47–49] [Fig. 17(a)]. An ultrafast optical pulse $E(\omega)$ propagating inside a nonlinear electro-optic crystal is the source of a time-varying second-order polarization term that can be expressed as [203]

$$P_i^{(2)}(0) = \sum_{j,k} \varepsilon_0 \chi_{ijk}^{(2)}(0, \omega, -\omega) E_j(\omega) E_k^*(\omega), \tag{23}$$

where the indices i, j, and k correspond to the Cartesian components of the field, and $\chi_{ijk}^{(2)}$ is the second-order susceptibility tensor element for the crystal. Equation (23) indicates that, when the optical electric field $E(\omega)$ is correctly oriented relative to the crystal axis, the induced second-order polarization is roughly proportional to

Figure 16

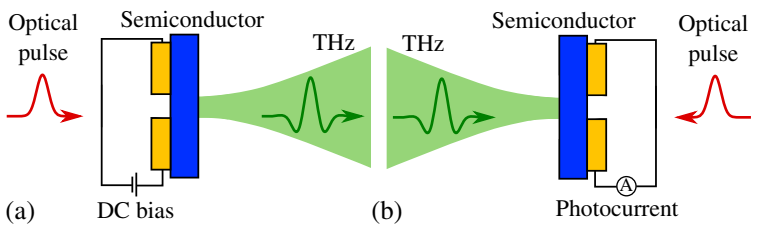

Schematic of the photoconductive antenna operation to (a) generate and (b) detect THz pulses.

its square $|\vec{P}^{(2)}| \propto |E(\omega)|^2$. For THz generation, the optical field is a time-dependent femtosecond pulse, for example, a Gaussian distribution with a width related to a [211]:

$$E(t) \propto E_0 e^{-at^2} e^{i\omega t}. \tag{24}$$

Therefore, the induced polarization is also time dependent and proportional to the envelope of the optical pulse:

$$|P^{(2)}| \propto E_0 e^{-2at^2}. \tag{25}$$

Furthermore, this induced polarization is the source of a THz electric field $\vec{E}_{\mathrm{THz}}(\omega)$ through the wave equation

$$\nabla^2 \vec{E}_{\mathrm{THz}} - \frac{n_{\mathrm{THz}}}{c^2} \frac{\partial^2 \vec{E}_{\mathrm{THz}}}{\partial t^2} = \frac{1}{\varepsilon_0 c^2} \frac{\partial^2 \vec{P}^{(2)}}{\partial t^2}, \tag{26}$$

where n_{THz} is the crystal's refractive index at THz frequencies. Thus, in principle, the THz pulse spectral bandwidth can be increased by reducing the optical pump pulse duration. In practice, the phase-matching condition, which includes the crystal dispersion at optical and THz frequencies [212], bounds the interaction length (walk-off length) and limits the efficiency of the THz generation. ZnTe is the most commonly used crystal for THz generation. A second popular choice is the $LiNbO_3$ crystal, which has a larger nonlinear coefficient, but that requires a tilted-pulse-front excitation for efficient generation [213–215]. With this method, single-cycle THz pulses with amplitudes exceeding 1 MV/cm can be generated [216]. Recently, nonlinear organic crystals have also been successfully used to generate THz pulses through optical rectification [50]. In Ref. [51], Vicario *et al.* used a Cr:forsterite laser at 1.25 μm to pump organic crystals DAST, OH1, and DSTMS, generating THz pulses with peak electric fields of 6.2, 9.9, and 18 MV/cm, respectively. We also mention the generation of THz pulses with tight focus of ultrafast optical pulses to generate gas plasma (for example, in air) and THz radiation through a four-wave mixing process involving third-order nonlinear susceptibility [69]. The reciprocal nonlinear process can also be used to coherently measure the THz pulse from the THz field-induced second harmonic (TFISH). This technique is known as the THz air-biased coherent detection technique (THz-ABCD). Compared to the generation/detection with optical rectification in a crystal, THz-ABCD provides a very large spectral bandwidth (from 0.2 THz to >30 THz), limited primarily by the optical pulse duration [70].

Using nonlinear crystals, the detection is based on electro-optic sampling (EOS), which is conceptually the opposite of optical rectification [64–68,212]. Under the Pockels effect, the THz electric field modulates the birefringence of a $\chi^{(2)}$ crystal. Therefore, by probing the birefringence with a femtosecond optical beam, the THz electric field can be coherently measured. Figure 17(b) shows a typical experimental setup for detecting THz pulses using EOS. The optical probe beam and the THz pulse interact inside the crystal. The linearly polarized optical beam will have a slightly elliptical polarization at the output of the crystal. Then, a polarization control system is used to extract from the elliptical polarization its two orthogonal linear components for balanced detection. For example, a quarter-wave plate can be used to convert the optical probe beam polarization into an almost-circular polarization. Then, a Wollaston prism can be used to divide the almost-circular polarization into two orthogonal components. Finally, a balanced photodetector measures the intensity difference between the two orthogonal components, which is proportional to the applied THz electric field.

Since EOS measures the state of polarization of a probing optical beam, conventional visible/infrared cameras can be used to provide real-time THz images (see Section 3.4 for details). We mention that the nonlinear parametric upconversion process [39,217,218] has also been used to demonstrate CW THz imaging with infrared cameras [161,219,220].

3.2. Fast Optical Delay Line

In THz-TDS, an optical delay line is used to scan and measure the THz pulse in time domain. The pulse spectrum is then retrieved using Fourier transform. In a classic THz-TDS setup, a linear reflective optical delay line positioned either in the emission or detection side is used. Such delay lines are realized by mounting a retroreflective prism onto a linear mechanical micropositioning stage. Thus, when the delay line travels a distance Δz, the time delay between the probe and pump pulses is modified to $\Delta t = 2\Delta z/c$. In this expression, the factor 2 expresses the fact that the optical beam travels twice the distance (back and forth) in the delay line. As a typical THz pulse has $\sim$1 ps duration, one normally uses $\delta t = 0.01$ ps sampling resolution to correctly resolve the THz pulse. This, in turn, imposes restriction on the precision of the micro-positioning stage $\delta z = c\delta t/2 \sim 1.5$ μm, which is readily achievable with high-quality commercial micro-positioning mechanical stages.

The THz spectrum is obtained by taking the Fourier transform of the temporal pulse. From the properties of the Fourier transform, it follows that the pulse maximal frequency $\nu_{\max}$ and the frequency resolution $\delta\nu$ are given by

$$\nu_{\max} = \frac{1}{2\delta t} = \frac{c}{4\delta z}, \tag{27}$$

$$\delta\nu = \frac{1}{\Delta t_{\max}} = \frac{c}{2\Delta z_{\max}}, \tag{28}$$

where δt and $\Delta t_{\max}$ are the temporal sampling resolution and the total temporal delay used in the pulse acquisition, respectively, while δz and $\Delta z_{\max}$ are the positional increment and the total movement of the delay line, respectively. For example, a

Figure 17

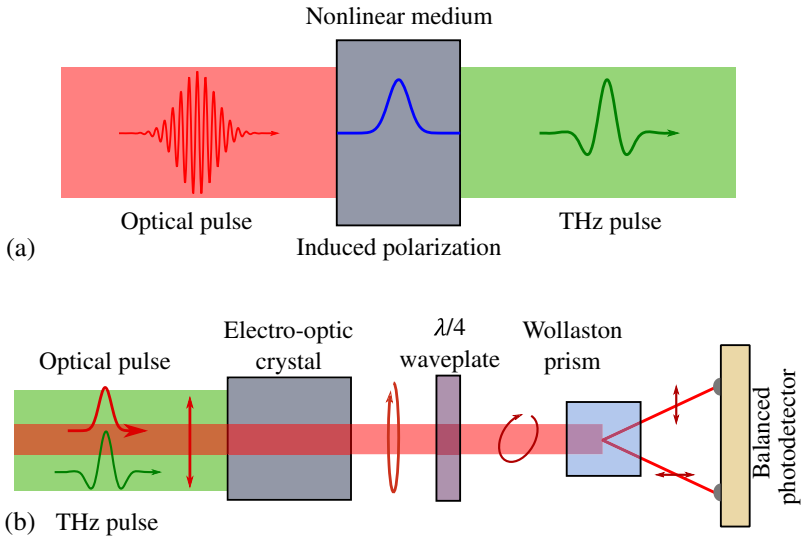

(a) THz generation using optical rectification and (b) THz detection using EOS.

$\delta z = 30$ μm positioning step size and a total delay line displacement of $\Delta z_{\max} = 30$ mm gives a spectrum with a maximal frequency of 2.5 THz and a resolution of 5 GHz.

For real-time imaging applications, the raster scanning of a sample is too time-consuming mostly due to the limited scanning speed of the optical delay lines, which typically do not exceed 1 Hz, thus resulting in ~1 s per pixel acquisition rates. The limited speed of traditional optical delay lines that use mechanical micropositioning stages is essentially due to their interrupted back-and-forth linear displacement. From a mechanical point of view, rotary movements enable uninterrupted displacements with higher speeds, which prompted significant research into the development of rotary delay lines. In the following, we begin by reviewing two major types of mechanical rotary delay lines that are based on rotary reflectors (Section 3.2a) or rotary prisms (Section 3.2b). Finally, in Section 3.2c we focus our attention on non-mechanical delay lines.

Here, it is important to note that even if infinitely fast optical delay lines would become available in the future, one still has to be aware of the fundamental signal acquisition delay per pixel, which is related to the averaging time constant of the lock-in amplifier used to increase the SNR of the detected signal. As more powerful THz emitters become available in the future, the averaging times could become shorter. A typical lock-in averaging time used in the current low-power THz-TDS systems is larger than $\delta t_{av} = 1$ ms. Ideally, lock-in averaging has to be done for every position of the delay line, thus resulting in a total acquisition time for a single THz pulse (single pixel) of $\delta t_{av}\Delta t_{\max}/\delta t = \delta t_{av}\Delta z_{\max}/\delta z \sim 1$ s in the case of $\delta t_{av} = 1$ ms, $\Delta z_{\max} = 30$ mm, and $\delta z = 30$ μm discussed above, which is a an example of a typical high-resolution THz scan.

3.2a. Rotary Reflectors

Rotary delay lines can feature planar or curvilinear mirrors that are mounted directly or otherwise actuated by a rotating motor shaft. Rotary reflector lines were typically placed in the path of an optical pump beam, but they could be placed in the THz beam path.

Rotary optical delay lines were originally developed for optical coherence tomography (OCT) (notably multiple-pass cavity delay lines [221,222]), and they generally feature a combination of rotating curved and planar mirrors [223,224], which can even include turbines in place of motors for faster rotation speeds. Although optical delay lines for OCT enable very high scanning rates of up to several tens of kilohertz, such delay lines show small optical delays (~20 ps) that are insufficient for THz-TDS applications.

To increase the maximal optimal delay, retroreflectors coupled to a galvanometer were proposed for ultrafast optical measurements [225]. Such a system achieved an optical delay of 300 ps with a scanning rate of 30 Hz. However, since the linear movement of the mirror induced by the rotating galvanometer was sinusoidal in time, an additional calibration step was needed to recover the instant value of the linear optical delay as a function of time.

Curvilinear reflective surfaces designed to provide linear optical delay as a function of the reflector rotation angle were first reported in Refs. [226–230]. In Ref. [228], Kim *et al.* mounted six reflectors onto a servo motor and demonstrated acquisition of the THz pulses with a net scanning rate of 400 Hz and a maximal optical delay of 70 ps. However, in their design, the incident beam and the reflected beam were collinear. Therefore, a beam splitter was needed to separate the incident and reflected beams, thus leading to a significant loss of optical power. The importance of this design is in

its linear dependence on the reflector rotation angle. Thus, by using a motor with a fixed and stable angular rotation frequency, a linear optical delay as a function of time is assured, and no additional calibration steps are needed.

In Ref. [229], Skorobogatiy developed a comprehensive mathematical theory for the design of rotary delay lines that feature up to three rotating and stationary curvilinear reflectors. Analytical and semi-analytical expressions for the reflector shapes were given for four classes of rotary delay lines that included linear dependence of the optical delay on the reflector rotation angle. Thus, the work analyzed (1) a single rotating reflector, (2) a single rotating reflector and a single stationary reflector, (3) two rotating reflectors, and (4) two rotating reflectors and a single stationary reflector. In the case of two rotating reflectors, the author showed that it is possible to separate the incoming and outgoing beams, while still keeping a linear relationship between the delay and the rotation angle.

In the follow-up work [230], a linear rotary delay line featuring two rotating reflectors was realized experimentally and employed in a THz-TDS setup designed for spectroscopy of dynamic processes. Particularly, four pairs of curvilinear reflectors were fabricated using computer numerical control (CNC) machining on the same rotary disk [Fig. 18(a)]. The acquisition of THz pulses was demonstrated with a speed of up to 48 Hz per blade (192 Hz with four blades), with a maximal optical delay of ~80 ps [Fig. 18(b)]. The input and output beams were physically separated in space, thus avoiding the use of a beam splitter. To record THz traces with such high acquisition rates, the authors replaced the lock-in amplifier with a low-noise transimpedance amplifier. They showed that the bandwidth of the detected signal decreased as the rotation speed increased, and they related this to the acquisition electronics [Fig. 18(c)]. As for practical applications of such a system, the authors monitored the time dynamics of a spray painting process by observing the amplitude and temporal position evolution of the main THz peak during paint deposition and drying [Figs. 18(d) and 18(e)]. They also demonstrated detection of thickness of free-falling polyethylene samples (moving speeds of up to 1 m/s) by monitoring in real time the optical delay of the THz pulse [Figs. 18(f) and 18(g)] with and without a sample. The results were shown to be on par with manual micrometer measurements of the sample thickness.

However, the curvilinear reflectors developed in Refs. [226–230] were essentially designed with ray optics, assuming infinitely thin laser beams. Therefore, distortion of the wavefront was important and, consequently, the parallel incident beam was distorted after reflection. This results in a less efficient generation or detection of THz radiation.

3.2b. Rotary Prisms

Rotary delay lines can also feature rotating prisms. In such systems, the variable optical delay is generated by rotating a prism in the path of the optical pump or the THz beams. In Ref. [231], Ballif *et al.* used a rapidly rotating BK7 glass cube ($n = 1.5$ at 850 nm) to realize such a delay line. They showed that the optical delay as a function of the angle had 20% deviation from a linear curve. In Ref. [232], they demonstrated a high repetition rate of 28.6 kHz with a maximal optical delay of 6.67 ps. However, this delay is too small to be useful for applications in THz-TDS. By increasing the size of the cube, the total optical delay can be increased. Thus, with a cube size of 50 mm, the same authors demonstrated a total optical delay of up to 215 ps [231]. However, with large cubes, when placed in the path of a pump beam, group velocity dispersion (GVD) becomes important, which leads to broadening of the femtosecond pulse, lower THz generation efficiency, and reduced THz pulse bandwidth.

Figure 18

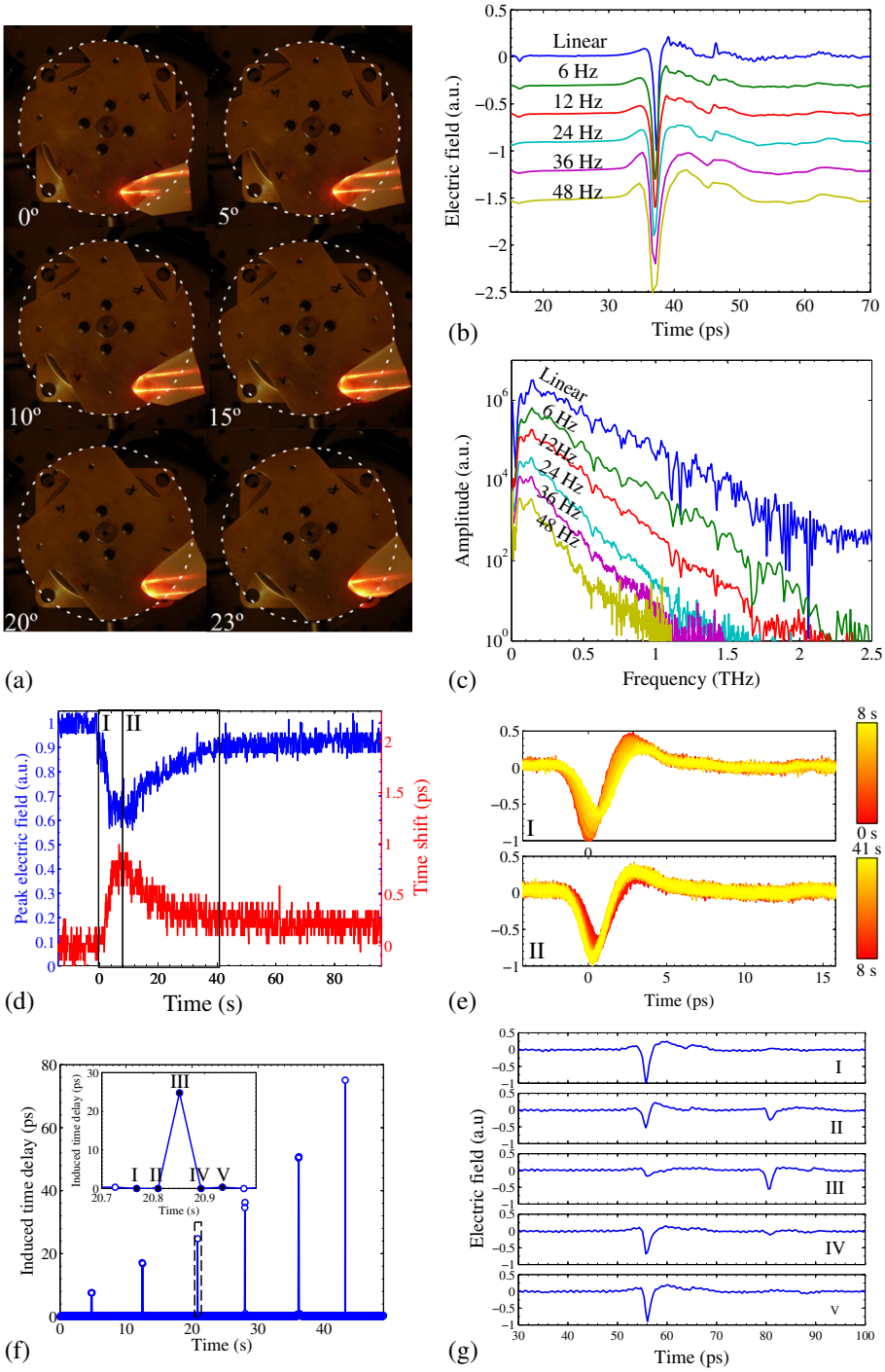

(a) Experimental realization of a linear rotary delay line featuring four pairs of the curvilinear reflectors. (b) Time-domain THz pulses and (c) corresponding spectra for different angular rotation speeds. (d) Real-time monitoring of the spray-painting process. Amplitude (blue top) and temporal position (red bottom) of the THz peak that passes through a sprayed-on layer of paint. (e) Time-domain THz pulses during spraying action (region I) and during paint layer drying (region II). (f) Thickness evaluation of free-falling polyethylene samples. Induced time delay due to passing of polyethylene samples of different thicknesses. Inset: passing of a 14.72 mm sample and (g) corresponding time traces. © 2015 IEEE. Reprinted, with permission, from Guerboukha *et al.*, IEEE Trans. Terahertz Sci. Technol. **5**, 564–572 (2015) [230].

The abovementioned rotary delay line was designed for an infrared pump of nanometer-size wavelength. Therefore, complex alignment and precise manufacturing was required, with prism surface roughness smaller than $\lambda/10$. To circumvent these complexities, in Ref. [233], Probst *et al.* used an 80 mm cube of high-density polyethylene ($n = 1.53$) in the path of a THz beam to generate the optical delay [Fig. 19(a)]. This cost-effective method was relatively simple to implement. However, it provided a highly nonlinear dependence of the time delay on the rotation angle [Figs. 19(b) and 19(c)], thus requiring an additional calibration step. A complete rotation of the cube generated eight THz pulses with maximal optical delay of 40 ps each. The authors demonstrated acquisition rates of up to 800 Hz, the main limitations being the acquisition electronics, the induced air turbulence at high rotation speeds, relatively small time delay, and THz signal attenuation due to absorption in the prism material [Figs. 19(d) and 19(e)]. Furthermore, the authors used their delay line to image a floppy disk (100 mm × 100 mm) in less than 3 min, limited by the raster scanning of the sample and the acquisition electronics [Figs. 19(f) and 19(g)].

3.2c. Non-Mechanical Time-Domain Sampling

To avoid mechanical sampling of the time delay, methods based on modifying the laser repetition rate of the femtosecond laser can be used. Asynchronous optical

Figure 19

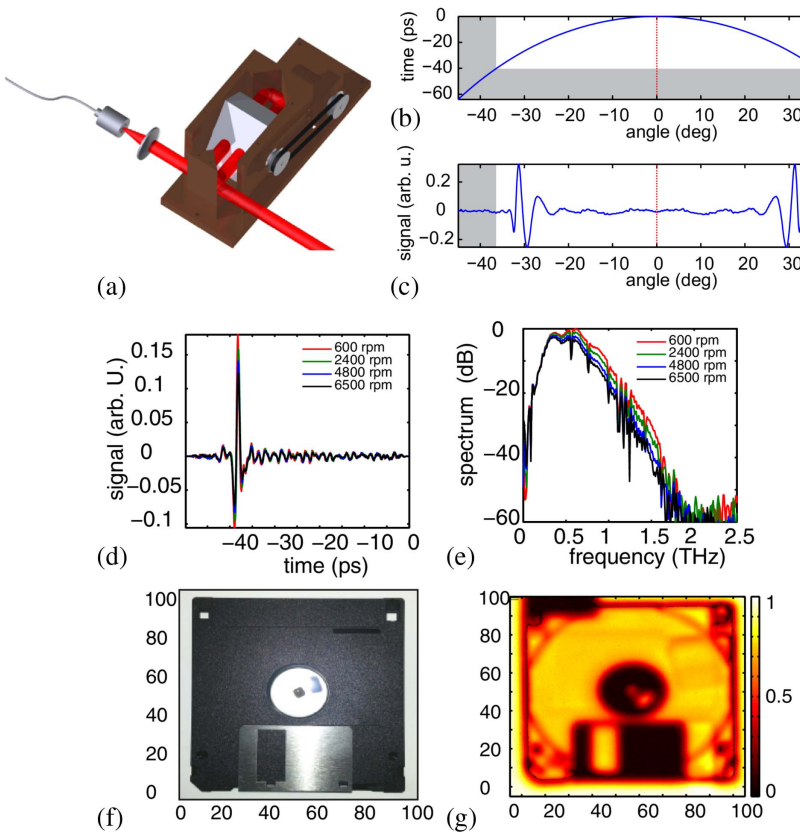

(a) Rotary optical delay line featuring a rotating HDPE cubic prism. (b) Nonlinear time delay as a function of the angle of rotation. (c) Raw THz traces for different rotation speeds of a prism. (d) Calibrated time traces and (e) corresponding spectra for different rotation speeds. (f) Photograph and (g) THz transmission image of a 3.5 inch floppy disk. Reprinted with permission from [233]. Copyright 2014 Optical Society of America.

sampling (ASOPS) was introduced in the pump–probe scheme to detect molecular species concentrations in flames [234,235]. It was first implemented in the THz-TDS configuration in Refs. [236,237]. In this technique, scanning of the time delay is obtained by using two femtosecond lasers (one laser is placed in the emission line, another in the detection line) featuring two slightly different pulse repetition rates f_1, f_2. Consequently, the relative time delay between the two pulse trains will mimic a linear ramp from 0 to $\Delta t = 1/f_1$ (assuming $f_2 > f_1$), while the scan rate will be determined by the beat frequency between the two lasers $\Delta f = f_2 - f_1$ [Fig. 20(a)].

In Ref. [238], Bartels *et al.* used two mode-locked Ti:sapphire femtosecond lasers with repetition rates close to 1 GHz and an offset frequency of $\Delta f = 10$ kHz. As a result, a temporal 1000 ps scan was performed with a scan rate of 10 kHz (acquisition time per single THz pulse trace of 100 μs). By reducing the temporal window, one can furthermore increase the scan rate. For example, in Ref. [239], 100 ps total delay has been demonstrated at a repetition rate of 100 kHz. However, to obtain such performance, unconventional lasers with 10 GHz repetition rate were used.

As ASOPS constantly scans the entire time interval between two consecutive pulses, this might be wasteful if the size of the scanned temporal window (say ~1000 ps) exceeds greatly the time duration of a typical broadened THz pulse (10–100 ps).

Figure 20

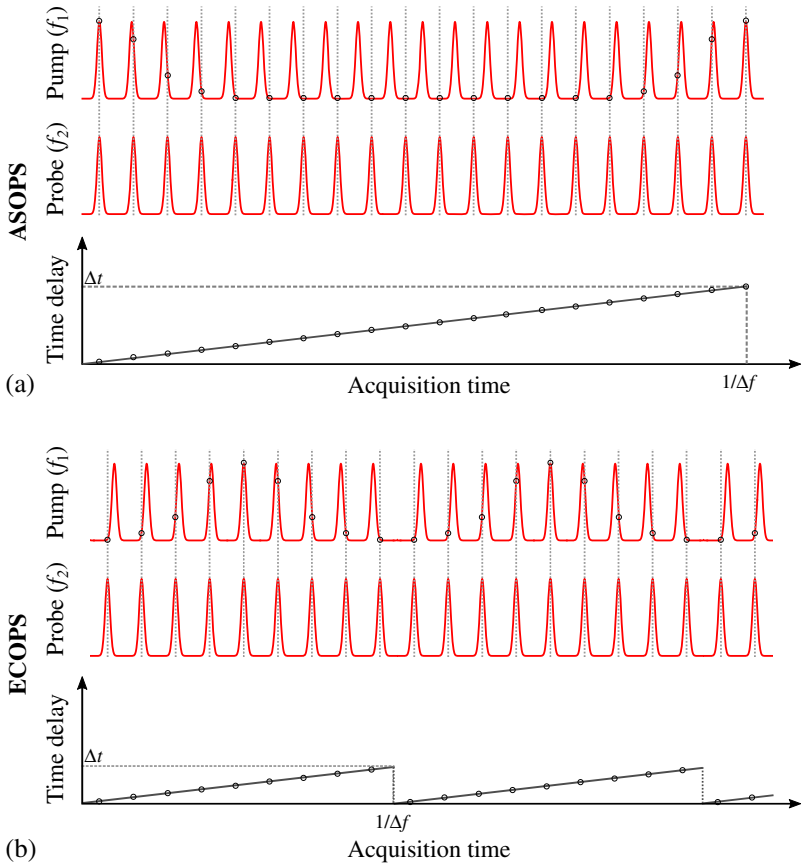

Schematic description of the (a) ASOPS and (b) ECOPS technique. In ASOPS, the pump and probe pulses have slightly different repetition rates, leading to a continuous scan of the time delay between consecutive pulses. In ECOPS, the repetition rate of the pump is modulated to avoid wasting the temporal window between consecutive pulses.

To reduce the size of the scanned temporal window, electronically controlled optical sampling (ECOPS) has been developed as an alternative to ASOPS [240–242]. In ECOPS, the repetition rate of one of the lasers is precisely controlled by electronically modulating the cavity length of one of the lasers. Consequently, the scan range can be correctly adjusted to the time of the THz pulse [Fig. 20(b)]. As a result, in Ref. [241], a 77 ps time delay window is scanned at a scan rate of 1 kHz, an improvement of 50 times compared to the conventional ASOPS, using the same parameters. In Ref. [243], for versatility, both the ASOPS and ECOPS techniques were implemented in the same fiber-based laser system.

ASOPS and ECOPS techniques have many benefits. The absence of moving parts allows for faster scanning rates, eliminates the positional instabilities of the laser beam, and removes the electronic noise caused by motor movement. However, its main disadvantage is the need to use two ultrafast lasers, which essentially doubles the cost of the THz-TDS system.

The optical sampling by laser cavity tuning (OSCAT) technique simplifies the system by using a single femtosecond laser [244–246]. Instead of having balanced optical paths in the emitter and detector sides, OSCAT uses the pulse i and the successive pulse $(i + a)$ in the same pulse train. Consider a laser emitting a train of optical pulses with a repetition rate of f that can be tuned by Δf (Fig. 21). The pulse i and the pulse $(i + a)$ have unbalanced optical paths, where the pulse $(i + a)$ has travelled the additional optical path length:

$$l_a = \frac{ac}{nf}, \tag{29}$$

with c the speed of light and n the refractive index of the propagation medium for the pulse $(i + a)$, for example, an optical fiber. With such unbalanced optical paths, the optical delay between the pulse i and the pulse $(i + a)$ is a function of the laser repetition rate f and its tuning Δf through the following relation:

$$\delta t = a\left(\frac{1}{f} - \frac{1}{f + \Delta f}\right). \tag{30}$$

Therefore, by dynamically changing the tuning Δf, the temporal window between two optical pulses can be scanned.

OSCAT was first introduced and demonstrated in cross-correlation measurements in Refs. [244,245]. In Ref. [246], the OSCAT technique was implemented for THz-TDS, with a 1550 nm fiber-coupled laser with a repetition rate of $f = 250$ MHz that could be tuned over $\Delta f = 2.5$ MHz using a precise intracavity stepper motor in the laser cavity. Therefore, to use the maximal delay between two adjacent pulses

Figure 21

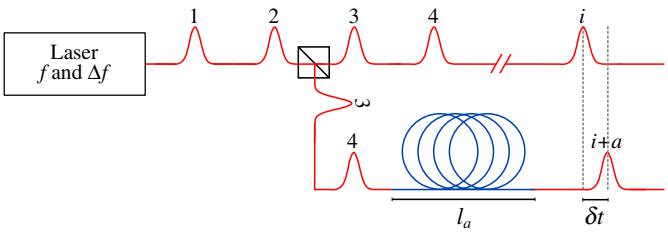

Schematic description of the OSCAT technique.

($\Delta t = 1/f = 4$ ns), $a = 101$st consecutive pulse must be used. This results in an additional optical path of $l_a = 121$ m in free space for the pulse $(i + a)$. Since this distance is impractical for compact THz-TDS systems, a combination of a standard single-mode fiber and a telecom dispersion fiber of a total length of 80 m was used. The same system was also operated in a rapid scan regime using a 3.5 kHz piezoactuator in the laser cavity to demonstrate over 5 ps optical delay at a scan rate of 100 Hz. Today, using the OSCAT technology, commercial systems achieve up to 40 ps total delay at scanning rates of 200 Hz.

3.3. Photoconductive Antenna Arrays

Integration of several PCAs into imaging arrays is an interesting proposition for real-time THz-TDS imaging. In this section, we overview some attempts to fabricate arrays of PCAs. In Ref. [247], Pradarutti *et al.* fabricated an array of 15 antennas with an inter-antenna distance of 1 mm packaged into a single photoconductive chip. Each antenna featured a gap of 30 μm by 5 μm. By using a telescope system and cylindrical lenses, they focused a 350 mW optical beam into an array of 15 PCA detectors [Fig. 22(a)]. A multichannel lock-in amplifier was used to improve the SNR [248]. The measured THz traces [Fig. 22(b)] demonstrate a lateral variation of the amplitude that was related to the incident THz nonuniform profile. Then, they imaged a metallic Siemens star of 60 mm ×50 mm [Fig. 22(c)] by moving the PCA array. The image was acquired in ∼10% of the time required to measure it with a single-pixel PCA. However, the area covered by the optical beam on the multiarray PCA (10,000 μm × 10,000 μm) was significantly larger than the effective gap area of the PCA (75 μm × 75 μm). Consequently, only about 2.6 mW illuminated each gap, while the remaining increased the overall noise level. In Ref. [249], a microlens array was used to focus the optical beam into the gaps. In Ref. [250], the authors proposed and experimentally explored a concept of dynamically reconfigurable THz-PCA arrays. Such arrays feature several wide-gap THz antennas placed in parallel to each other that were dynamically interrogated by steering a multifocused

Figure 22

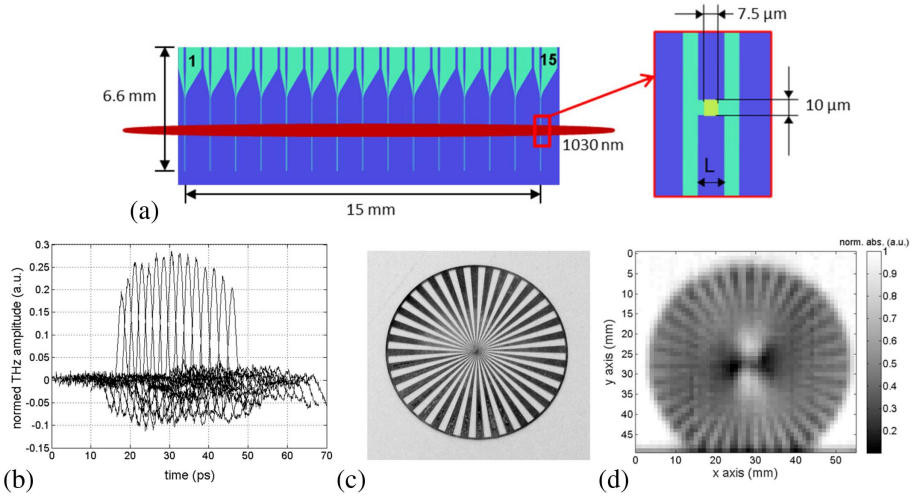

(a) Schematic and geometry of the linear array of PCA with 15 detectors used in Ref. [247]. (b) Simultaneously recorded THz pulses. (c) Photograph and (d) imaging of a metallic Siemens star. Reprinted with permission from [247]. Copyright 2014 Optical Society of America.

optical pump beam along the antenna gaps. The pump beam was formed and steered using a spatial light modulator.

Designing and using PCA arrays, although very attractive, presents many challenges. Considering that the efficiency of a single PCA is relatively low, simultaneous interrogation of multiple PCAs requires powerful probe beams. For example, a 10×10 array using 10 mW per channel would require a 1 W femtosecond laser. Additionally, the focusing optics are complicated to manufacture, and dense integration on multiple antennas on the same chip is problematic due to crosstalk or interference between them. These practical difficulties currently confine almost exclusively the use of PCAs as coherent single-pixel detectors for imaging (see Section 5).

3.4. EOS with Visible/Infrared Cameras

3.4a. Dynamic Subtraction and Balanced Electro-Optic Detection in a Camera

Within the EOS modality, since it is an optical beam in the visible/infrared region that is detected, conventional charge-coupled device (CCD) or complementary metal-oxide semiconductor (CMOS) visible/infrared cameras can be used to obtain a 2D THz image. However, unlike single-pixel detection schemes, the use of unfocused beams decreases the local amplitude of the detected signal, approaching it to the noise level. Furthermore, the SNR of an EOS-based THz imager suffers from the limited ability of directly using lock-in detection with the CCD and CMOS devices. In the following, we highlight some techniques developed in the literature to increase the SNR when using CCD/CMOS cameras with EOS.

Already in 1996, Wu *et al.* demonstrated EOS imaging with a ZnTe crystal and a thermoelectrically cooled CCD camera [67]. However, unlike in the case of single-pixel EOS, the THz beam is spread over a larger surface and no lock-in amplifier can be directly used with the CCD. This resulted in a poor SNR that required the use of a thermoelectrically cooled camera. The dynamic subtraction technique was introduced in Refs. [251–253] to improve the sensitivity. The technique essentially consists of subtracting a reference frame (without THz) from a signal frame (with THz) to dynamically remove the background noise.

To increase the sensitivity even further, in Ref. [254], Pradarutti *et al.* demonstrated balanced electro-optic detection using a linear array consisting of eight pairs of InGaAs photodiodes in conjunction with a Wollaston prism. Although their approach combined lock-in amplification to enable high SNR, raster scanning was still necessary to scan along the second dimension. In Ref. [255], both dynamic subtraction and balanced electro-optic signals were used to increase the SNR. A Wollaston prism divided the optical probe beam into two mutually orthogonal polarizations that were detected simultaneously by a CCD [Fig. 23(a)]. As expected [256], the two measured polarizations had opposite values such that their difference increased the signal by a factor of 2 [Figs. 23(b) and 23(c)]. An algorithm was designed to perform the subtraction of the two images and reduce the misalignment errors. Furthermore, dynamic subtraction was performed by subtracting one frame (with THz signal) from a reference frame (without THz). An example of a THz image is given in Figs. 23(d) and 23(e). In Ref. [257], the authors added a half-wave plate in the probe beam to perform real-time THz polarization imaging.

3.4b. Real-Time Near-Field EOS Imaging

Real-time near-field imaging using EOS is possible by placing the sample in direct contact with the nonlinear EOS crystal. In Ref. [258], Blanchard *et al.* imaged an area of 370 μm × 420 μm at 35 frames per second with a spatial resolution of 14 μm ($\lambda/30$ at the center frequency of 0.7 THz). To achieve such performance, the authors

generated a THz pulse with a peak electric field of 200 kV/cm by optical rectification in $LiNbO_3$ using a tilted-pulse-front excitation. For detection, the THz pulse was focused on a $LiNbO_3$ crystal with a thickness of 20 μm [Fig. 24(a)]. On the opposite side, the 800 nm probe light interacted with the crystal and was reflected into a balanced imaging setup using a CCD camera. As in Ref. [255], corresponding pixels of the orthogonal polarizations were subtracted to increase the SNR. To obtain high spatial resolution, a very thin electro-optic crystal has to be used. At the same time, a powerful THz source was necessary to compensate for the small interaction length between the THz and the optical probe. To demonstrate the ability of their THz microscope in imaging near-field structures, a metallic dipole antenna of subwavelength dimensions was directly deposited on top of the $LiNbO_3$ crystal [Fig. 24(b)]. By displacing the delay line, the reemitted THz radiation from the dipole could then be imaged at the picosecond scale [Fig. 24(c)].

In Ref. [260], to demonstrate biomolecule probing, free induction decay of a tyrosine crystal was observed in the near field, while in Ref. [261], resonant modes of a split ring resonator were imaged. Since then, many methods have been considered to

Figure 23

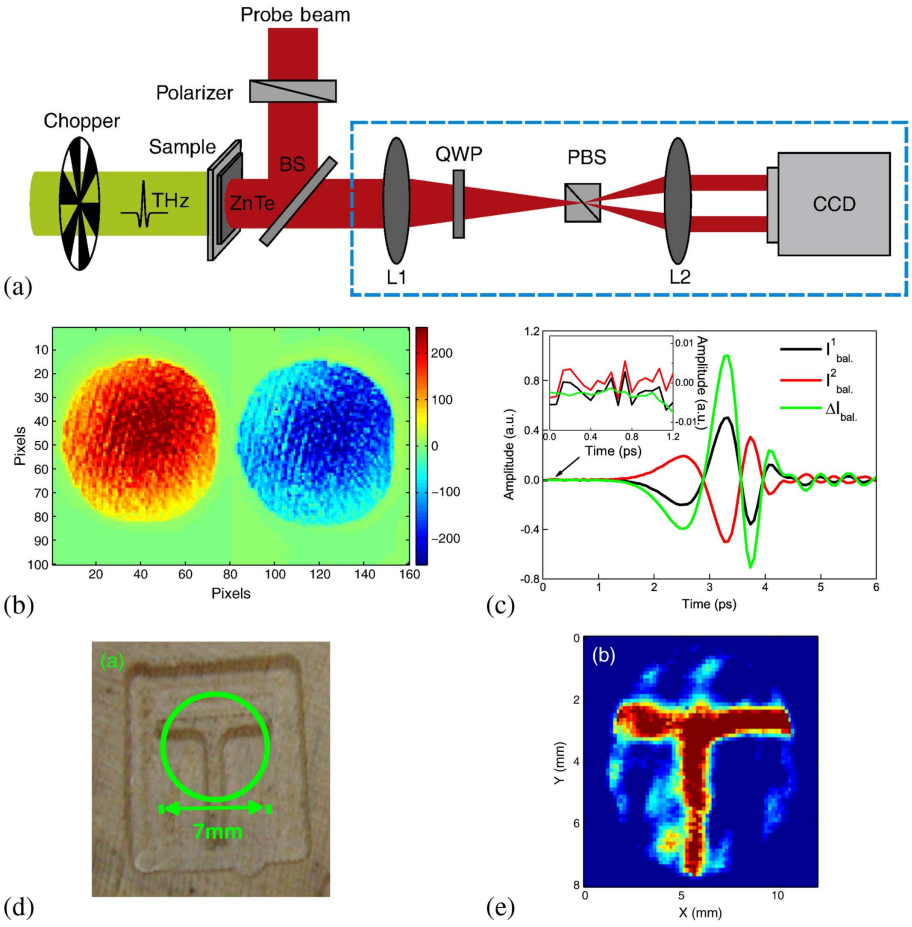

(a) Experimental setup for EOS with a CCD camera. (b) Both polarizations measured spatially by the CCD and (c) as a function of time with the delay line. (d) Photograph of the letter T engraved in wood and (e) reconstructed THz image by subtracting corresponding pixels in the CCD. Reprinted from Opt. Commun. **283**, Wang *et al.*, "Terahertz real-time imaging with balanced electro-optic detection," 4626–4632 [255]. Copyright 2010, with permission from Elsevier.

further increase the spatial resolution [170,259,262]. In Ref. [259], spatial resolution up to $\lambda/600$ at 100 GHz has been demonstrated. To achieve such performance, the $LiNbO_3$ crystal thickness has been reduced to 1 μm, the optical probe was spectrally

Figure 24

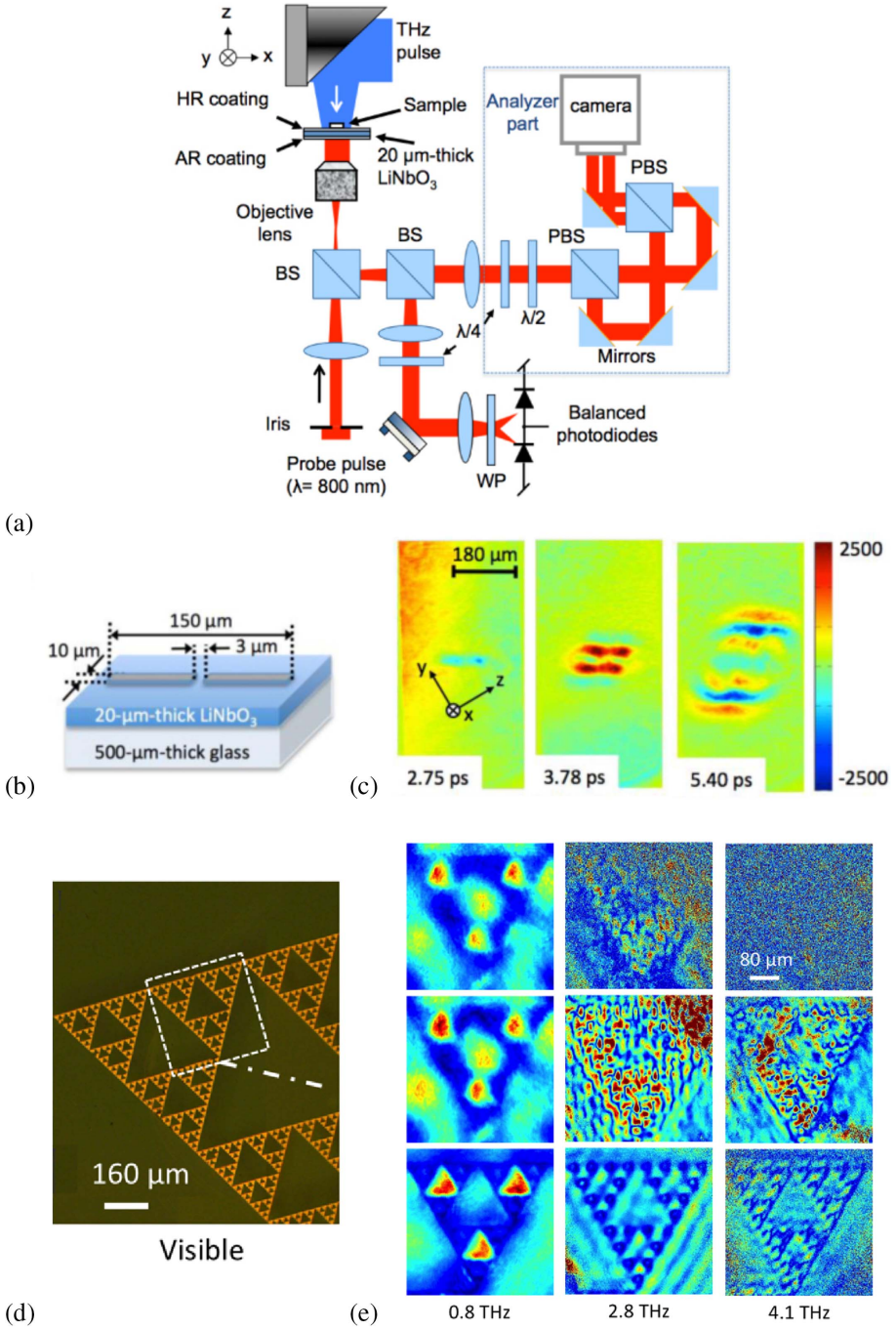

(a) Experimental setup of the EOS THz microscope with a CCD camera. (b), (c) Near-field imaging of a metallic antenna in the process of re-irradiating the incident THz pulse. Reprinted with permission [258]. Copyright 2011 Optical Society of America. (d) Demonstration of improved spatial resolution by imaging a Sierpinski fractal (e) without spectral filtering and a 10 μm crystal (top), with spectral filtering and a 10 μm crystal (middle), and with spectral filtering and a 1 μm crystal (bottom). Reprinted with permission from [259]. Copyright 2016 Optical Society of America.

filtered, and a 10× objective lens was used. A 100 nm thick gold Sierpinski fractal was patterned on top of 10 μm and 1 μm crystals [Fig. 24(d)] and imaged in Fig. 24(e). By reducing the crystal thickness and by using spectral filtering, the spatial resolution was increased. To enable real-time near-field EOS imaging, a detailed description of the needed components is reviewed in Ref. [170].

3.4c. Temporal Encoding in the Camera

To record the complete THz temporal waveform, an optical delay line is still necessary. In principle, one could use the methods described in Section 3.2. However, for EOS sampling, one of the spatial dimensions of the camera can be used to encode the temporal dimension of the waveform. This idea was first demonstrated in Refs. [263–265] by using a chirped optical probe beam. Since distinct wavelengths travel with different speeds inside the EOS crystal, their polarizations are differently affected by the THz radiation through the Pockels effect. This essentially encodes temporal information about the THz waveform into the spectrum of the optical probe. Therefore, by using a grating to disperse the optical spectrum into a linear detector array, the THz temporal waveform can be sampled without the use of an optical delay line.

In Ref. [266], Shan *et al.* demonstrated single shot measurement of the temporal waveform by introducing an angle between the optical probe beam and the THz pulse. Thus, different points in the transverse spatial profile of the optical probe beam experienced different temporal positions of the THz electric field. Again, a linear array of detectors was used to resolve the THz waveform in a single shot. In Ref. [267], Yasuda *et al.* used a similar non-collinear geometry with a CCD camera [Fig. 25(a)]. One dimension was used to encode the temporal THz waveform, while the second was used to image one spatial dimension [Fig. 25(b)]. In [163], 3D imaging using THz-CT (Section 2.4) was demonstrated by imaging a pharmaceutical tablet in only 6 min [Fig. 25(c)]. To obtain a 2D image, the sample can be moved in the second dimension [268]. This approach is attractive for many industrial applications where a conveyer belt is used. This was demonstrated for biomedical applications in Ref. [269]. There, pharmaceutical tablets moving on a conveyer belt were imaged. Furthermore, spectroscopic identification of the crystallinity of dental tissue was demonstrated, along with observation of the drying process of wet hair.

3.5. Section Summary and Future Directions

Even though THz cameras are in rapid development (see Section 4), the development of THz-TDS-based imaging systems is still of great importance, since they can provide additional/complementary spectroscopic information to reconstruct an image (Section 2.1). Furthermore, they feature outstanding SNR due to the lock-in technique. The ability of THz-TDS to measure both the amplitude and the phase of the THz pulse electric field allows for unique imaging modalities that simply cannot be achieved with conventional intensity-based THz cameras. For example, THz-TDS imaging can be used to map the complex refractive index and the conductivity of a sample, even at a subwavelength scale (near-field imaging).

As we saw in this section, the technical challenges to enable real-time THz-TDS imaging are intrinsically related to the THz-TDS setup. First, the mechanical linear optical delay line must be replaced to enable the acquisition of multiple THz pulses per second. Rotary optical delay lines in the form of curved mirrors in the optical path or prisms in the THz path are simple and cost-effective solutions. Ultimately, their speed is still limited by the motor or turbine rotation speeds and air turbulence, as well as by the need for costly high-speed electronics for signal processing. At the same time, non-mechanical solutions such as ASOPS, ECOPS, and OSCAT are attractive since

they can provide acquisition rates in the kilohertz range. Some of them are already commercially available, but ASOPS and ECOPS require the use of two synchronized femtosecond lasers, which essentially doubles the cost of the THz-TDS systems. In comparison, the OSCAT technique needs only one laser, at the expense of using dispersive fibers to generate the optical path differential.

The second problem that impedes real-time imaging is the fact that classical THz-TDS systems are built with single-pixel detectors. There are two major technologies to detect THz pulses: photoconductive antennas and EOS. For now, it seems that photoconductive antennas, while having a very high SNR, do not constitute the preferred approach for real-time THz imaging due to the necessity of slow raster scanning. So far, dense integration of multiple antennas on a single chip has proven to be problematic due to the electromagnetic crosstalk between them and the necessity of using multichannel lock-in systems (one lock-in per pixel). Additionally, interrogating multiple antennas at the same time also requires a powerful probe laser and intricate micro-optics for laser focusing. While several works demonstrated the fabrication of arrays of photoconductive antennas, we believe that the main application of photoconductive antennas will remain in the context of single-pixel imaging (Section 5) using beam-steering optics (Section 5.1), compressive sensing (Section 5.2), spectral encoding methods (Section 5.3), or other computational imaging techniques.

Figure 25

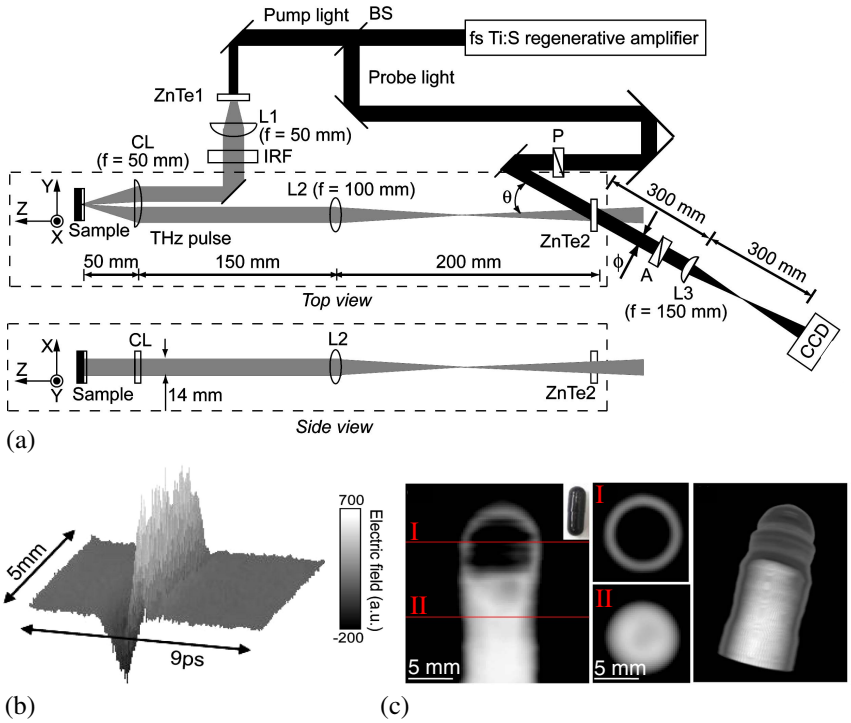

(a) EOS imaging setup using a non-collinear geometry and a CCD camera. (b) One dimension of a CCD camera records the temporal waveform, while the second one measures spatial information along one dimension. Reprinted from Opt. Commun. **267**, Yasuda *et al.*, "Real-time two-dimensional terahertz tomography of moving objects," 128–136 [267]. Copyright 2006, with permission from Elsevier. (c) 3D imaging of a pharmaceutical tablet acquired in 6 min using a THz-CT. Reprinted with permission from [163]. Copyright 2013 Optical Society of America.

In comparison, EOS has recently attracted much attention in the context of 2D real-time THz-TDS imaging. The fact that the technique records visible/infrared light means that conventional visible/infrared CMOS/CCD cameras can be used. EOS-based imaging still lacks in SNR compared to a photoconductive antenna detector with a lock-in amplifier, so further noise management within this technique is required. Moreover, there is a real interest in near-field EOS imaging since the crystals used to generate the EOS signal can also be used as sample substrates (contact-based near-field imaging). This interest is certainly driven by the recent development of efficient generation techniques with optical rectification and tilted-pulse excitation that allow reduction of crystal thickness, and, therefore, increase spatial resolution. In this context, EOS THz-TDS microscopes are within reach.

Finally, we would like to discuss two research directions that have emerged recently that may have important impact on THz-TDS systems in general, and THz-TDS imaging in particular. These are (1) THz quasi-time-domain spectroscopy systems (THz-QTDSs) and (2) CMOS-based electronic generation and detection of THz pulses. The THz-QTDS aims at replacing an expensive ultrafast laser by less expensive multimode laser diodes [270–272]. In short, a multimode laser beam comprising equally spaced spectral lines is focused onto a photoconductive antenna. In time domain, the result is a THz pulse train with a repetition rate that is determined by the mode spectral spacing [273]. In Ref. [274], imaging with a THz-QTDS system was demonstrated by using a 100 mW multimode laser diode at 662 nm, with mode spacing of 25 GHz and spectral emission bandwidths of 3 nm. In Ref. [275], a compact and cost-effective THz-QTDS system was proposed by mounting the laser diode directly onto a mechanical delay line extracted from a DVD drive. This prototype was fully controlled by a Raspberry Pi single-board computer with a sound card that fed the emitter antenna with a reference voltage, detected the current for digital software lock-in amplification, and controlled the stepper motor. In Ref. [276], a fiber-coupled THz-QTDS system was demonstrated using conventional telecom technology at 1550 nm. All these prototypes may pave the way for extremely affordable THz spectroscopy systems. However, the challenges for imaging applications using THz-QTDS are similar to those based on THz photoconductive antenna technology, namely, those related to the single-pixel nature of the detection device.

A second emerging idea for THz spectroscopy is the electronic generation and detection of THz pulses. Here, the main advantage is to completely avoid the use of lasers for THz pulse generation. These recent developments are based on CMOS processing technology, which may be beneficial toward mass fabrication of THz spectroscopy systems at lower costs. Two avenues are being considered for electronic generation of THz pulses. The first idea uses a technique similar to mode-locking in femtosecond lasers to dynamically shape pulses [277]. Using oscillatory CW sources on silicon, picosecond pulses are emitted by carefully controlling the amplitude and phase of the fundamental frequency and the multiple harmonics. The second idea is inspired by the spark gap transmitter, where an electromagnetic pulse is emitted by an antenna following a fast-rising/falling current switching [278]. Initially, an antenna stores a DC current in the form of magnetic energy, and, when the current is turned OFF, the antenna converts the energy into a radiated picosecond pulse. Similarly, an impulse is emitted following an ON switch. For now, the detection of these picosecond pulses has been demonstrated using a conventional THz-TDS system or using horn antenna detectors. Interestingly, in Ref. [279], an on-chip THz spectral detector is realized by measuring the scattered current density on a multiport antenna. The general concept is that different scattering modes are excited on the antenna depending on the excitation frequency. Therefore, the spectrum can be reconstituted by measuring the spatial current density and by using a one-time calibration

procedure. For now, these ideas of emission and detection of THz pulses using electronic means are limited to the sub-THz region.

4. THZ CAMERAS

Over the past decade, intensive research has been conducted to develop THz cameras similar to those available in the visible region of the spectrum. THz cameras must satisfy a number of requirements before deployment in industrial applications. First, they must operate at room temperatures while still retaining high sensitivity, thus forgoing the complexity associated with cumbersome and expensive cryogenic cooling systems. Second, to reduce the cost, the fabrication process of the THz cameras should be compatible with modern fabrication techniques, such as the CMOS process technology, which also allows scaling into high-resolution imaging arrays. Third, the size and weight of a THz camera along with its total power consumption should be small enough to facilitate the integration into industrial imaging systems. Finally, a THz camera should be sensitive enough to allow recording of THz videos at a high frame rate. This is especially important since powerful THz sources (particularly broadband sources) are still sparse. Ideally, the detector should be sensitive enough to record a THz image in passive imaging, i.e., without an active THz source. Ideally, THz cameras should be able to detect complex electric fields, while, for now, most THz cameras can detect only intensity. This, and the fact that cheap, high-power THz sources are still lacking, drive the competition between imaging using single point detection versus imaging using multipixel arrays.

In general, the performance of THz detectors can be characterized with two important figures of merit: the responsivity and the noise-equivalent power (NEP). The responsivity is the direct detector response (either in volts or amperes) to the incident THz power (in watts). It can be expressed in V/W or A/W, with the majority of THz imaging arrays employing voltage to characterize the THz signal. To measure the responsivity, one typically measures the total incident power using an etalon technique. In the case of THz cameras, assuming that the imaging array captures all the incident THz power, the responsivity per pixel can be assessed by summing the voltages of all the pixels and then dividing it by the total incident power. In general, higher responsivity is an indication of a better performing detector.

The NEP is a measure of the minimum detectable power. It is defined as the input power that results in a signal equal to the noise (SNR $= 1$) with a 1 Hz bandwidth output. It is measured in $\frac{\mathrm{W}}{\sqrt{\mathrm{Hz}}}$, and a lower NEP indicates a more sensitive detector. However, due to specific data acquisition conditions when using a camera, the minimum detectable power (in W) is often a better quantity to characterize the video mode operation. It corresponds to the lowest power that can be measured by a single pixel in a single frame. Clearly, this parameter depends on the frame rate, and a reduced frame rate can generally detect lower THz powers.

In this section, we review the two main classes of THz cameras that have been reported in the modern literature: THz thermal cameras and THz FET cameras.

4.1. THz Thermal Cameras

THz thermal cameras detect the heat generated by incident THz radiation. Depending on the detection principle of the heat, one usually distinguishes three types of thermal detectors of THz radiation: 1) Golay cells, 2) pyroelectric sensors, and 3) bolometers. In an imaging setup, they are commonly used with a modulated source, which is produced using an optical chopper, for example. While this allows reducing the ambient noise, it reduces the overall maximum frame rate that can be obtained at room temperature. The main advantage of thermal detectors is that they have very broad

spectral range of operation, something that is typically not obtainable with photon detectors.

In Golay cells, the generated heat is transferred to an expanding gas cell. The increased pressure is then optically measured by moving mirrors [58]. Since they rely on the mechanical movement of a membrane, Golay cells are slow detectors. Nevertheless, due to their simple operating principle, they are widely used to measure THz power. However, they are difficult to integrate into dense arrays of detectors. Consequently, THz imaging with Golay cells is often done in a single-pixel detection scheme [280]. Values for the NEP in Golay cells range between 0.1 and 10 $\mathrm{nW}/\sqrt{\mathrm{Hz}}$.

Pyroelectric sensors detect changes in the electrical polarizability of certain crystals caused by increase in the temperature. When an absorbing layer transfers the heat to the crystal, a temporary voltage is generated. Common pyroelectric crystals are triglycine sulfate (TGS), deuterated triglycine sulfate (DTGS), lithium tantalate ($LiTaO_3$), and barium titanate ($BaTiO_3$). Among these, TGS and DTGS have the highest sensitivities at THz frequencies [281], with typical responsivity and NEP of $\sim$1 kV/W and 1 $\mathrm{nW}/\sqrt{\mathrm{Hz}}$, respectively, at a modulation frequency of $\sim$10 Hz. Unlike Golay cells, pyroelectric detectors are commercially available as array cameras. For example, in Ref. [282], Yang *et al.* used a 124 × 124 pixel pyroelectric commercial camera to demonstrate THz imaging with a gas laser source at 1.89 THz (70 mW average power). Sensitivity of the pyroelectric detectors can be improved by reducing the crystal thickness and by increasing THz absorption in the crystal coating layer. Typical minimum detectable power for commercial pyroelectric cameras is in the range of 50–100 nW.

Another type of THz camera uses thermal bolometers as individual pixels. Because of the relatively high sensitivity and established fabrication technology, bolometer imaging arrays are currently considered prime candidates for real-time THz imaging.

The bolometer pixel operates by measuring changes in a temperature-dependent resistance. In Fig. 26(a), we have summarized the main constituents of a bolometer as described by Richards [283]. The radiation power P_{THZ} from the THz beam is incident onto an absorbing element (heat capacity C_A) connected via a thermal link (conductance G_L) to a heat sink (reservoir at temperature T_S). The temperature of the absorbing element T_A rises at a rate $dT_A/dt = P_{\mathrm{THz}}/C_A$ to the limiting value $T_A = T_S + \frac{P_{\mathrm{THz}}}{G_L}$, with the thermal time constant $\tau = C_A/G_L$. When the illumination is turned off, the temperature T_A relaxes back to T_s with the same time constant [Fig. 26(b)]. This

Figure 26

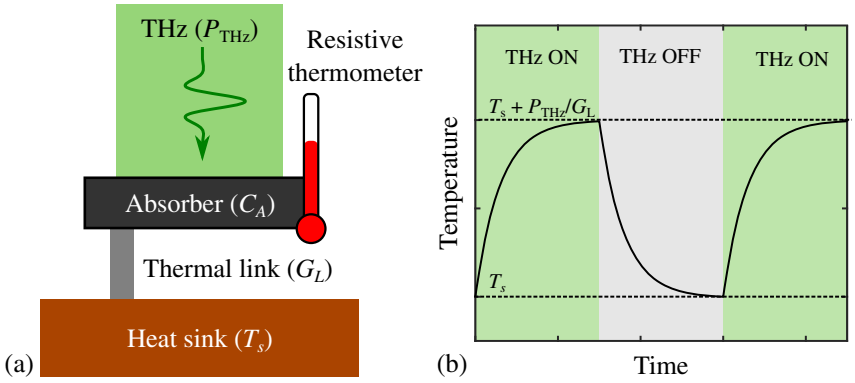

(a) Schematic representing the main components of the bolometer. (b) Rise and fall of the temperature in the absorber as a function of time.

temperature change is measured with a resistive thermometer (typically amorphous silicon or vanadium oxide) connected to the absorbing element.

Microbolometers are arrays of bolometers mounted onto readout integrated circuits (fabricated with CMOS process technology) for focal-plane camera operation. As the operation principle of microbolometers is not wavelength specific, commercial microbolometers designed for infrared radiation were first used for real-time THz imaging [284–287]. For example, in Ref. [285], Lee *et al.* used a commercial 320 × 240 pixel uncooled vanadium oxide (VO_x) microbolometer focal-plane array camera designed for 7.5–14 μm wavelengths. They used a quantum cascade laser at 4.3 THz (50 mW peak power) as a source to image the contents of a closed envelope. Since the camera was sensitive to both THz and infrared background radiation, three frames were necessary to obtain a THz image. The third frame (infrared signal only) was subtracted from the first frame (both infrared and THz signals), while the second frame was used as a buffer for the temperature to decay in the bolometer. This resulted in an overall frame rate of 20 frames per second (fps). In their following work, the authors also demonstrated stand-off real-time THz imaging at a distance of 25 m [288].

In more recent years, microbolometers were specifically designed to operate in the THz range. When cooled at cryogenic temperatures to remove background thermal noise, they can achieve remarkable NEP in the range of 10^{-16} $W/\sqrt{Hz}$ [71]. However, with proper design modifications, even at room temperatures, microbolometers can demonstrate high enough sensitivities to be suitable for a variety of industrial imaging applications. In Refs. [52,289], the authors at NEC corporation proposed to use a cavity structure to increase the sensitivity of a microbolometer THz camera of 320 × 240 pixels. Their device is schematically presented in Fig. 27(a) [290]. A thin metallic layer of TiAlV absorbed the THz radiation and induced changes in the resistance of the thermometer (VO_x film). Under the THz absorber layer, a thick metallic layer was placed, which reflects the unabsorbed THz radiation back into the bolometer. This geometry represents a resonating Fabry–Perot cavity between the bolometer and the reflector. A SiN_x layer was added to ensure the mechanical stability of the device and to match the effective cavity length with the THz wavelength. This addition led to an increase in the sensitivity in the sub-THz region, where the microbolometers are generally underperforming. They reported a minimum detectable power of 100 pW at 1 THz. Using optical rectification with tilted-pulse-front excitation in $LiNbO_3$, they demonstrated THz imaging of a dry leaf [Fig. 27(b)]. In Ref. [291], they used the microbolometer in conjunction with a diffraction grating to develop a real-time spectrometer that could operate at 15 fps.

In Refs. [54,292,293], the authors, affiliated with CEA-LETI, used an antenna to increase coupling of THz radiation to the amorphous silicon-based transducer in a bolometer [Fig. 27(c)]. Crossed bow-tie antennas were placed on top of a microbridge bolometer membrane. Both THz radiation polarizations were coupled through the dissipative currents in the load resistances located in the center of a bolometer. The antenna-coupled bolometer membrane was suspended on an 11 μm thick SiO_2 layer deposited over a metallic reflector to create a resonant cavity. In principle, the dimensions of the antenna and the cavity length can be tailored to any THz frequency. They achieved a minimum detectable power of 30 pW at 2.5 THz [quantum cascade laser (QCL) source]. Hidden objects under a shirt were imaged, and the field of view was increased with fast scanning optics [Fig. 27(d)].

Metamaterials have been investigated to increase the absorption of THz radiation [294–297]. In Ref. [298], Carranza *et al.* fabricated a 64 × 64 focal-plane array with metamaterial absorbers using a 180 nm CMOS process. Their main motivation was to exploit as much of the CMOS process technology as possible, thereby avoiding costly

postprocessing fabrication techniques. Thus, they integrated the readout electronics and the metamaterial absorber in the CMOS process. The metamaterial was designed to provide a broadband response centered around 2.5 THz. As for the sensor, they investigated two types of resistive thermometer. First, they patterned a VO_x sensor using postprocessing techniques, and they achieved a minimum NEP of 108 $pW/\sqrt{Hz}$ and a responsivity of 59 kV/W. Their second prototype used a silicon $p-n$ diode as the sensor. Although the diode is less sensitive to temperature changes, it can be patterned directly with the CMOS process. They obtained NEP of 10.4 $nW/\sqrt{Hz}$ and a responsivity of 274 V/W.

4.2. THz Field-Effect Transistor-Based Cameras

Rectification in the field-effect transistor (FET) is the second technological trend in THz cameras. Previous reviews on the topic can be found in Refs. [62,299,300,301]. The general idea is to use plasma wave excitations to enable response at frequencies considerably higher than the maximal transistor operation frequency (cut-off frequency). In the 1990s, using a direct analogy between the electron transport equation in 2D gated material and the hydrodynamic equations in shallow water, Dyakonov and Shur theoretically demonstrated that plasma waves in the FET channel could be used for THz detection [302]. Figure 28(a) schematically represents their proposed FET for THz detection. A DC voltage U_0 is applied between the gate and the source, while the incident THz radiation causes an alternating voltage U_a. Because of the asymmetry of the boundary conditions and due to the nonlinear properties of the plasma waves, a constant drain-to-source voltage $\Delta U \propto U_a^2$ is generated.

Figure 27

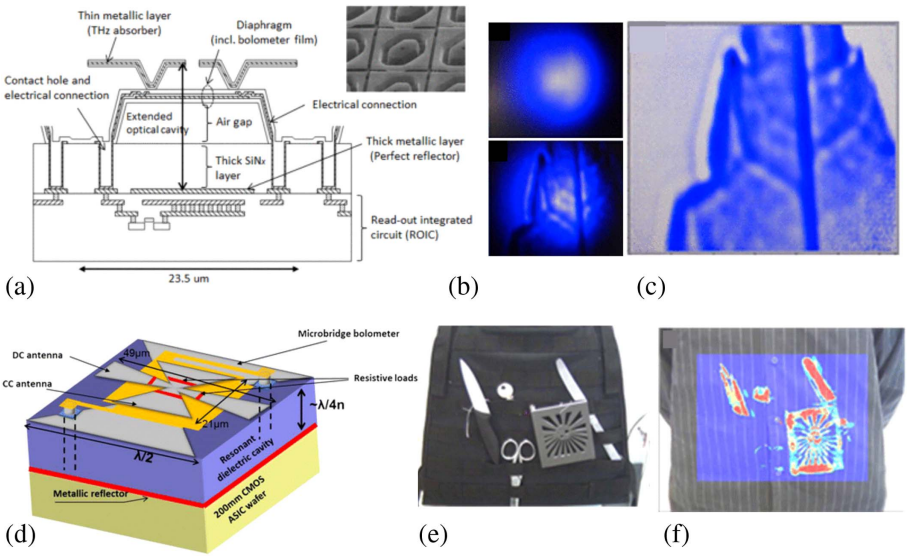

(a) Schematic representation of the cavity microbolometer developed in Ref. [290] (inset: micrograph). (b) Raw images without (top) and with (bottom) the dry leaf. (c) Corrected image for the non-uniform THz beam profile. © 2016 IEEE. Reprinted, with permission, from Nemoto *et al.*, IEEE Trans. Terahertz Sci. Technol. **6**, 175–182 (2016) [290]. (d) Schematic representation of the antenna-coupled bolometer developed in Ref. [54]. (e) Photograph of objects under a shirt that were (f) imaged with THz. Reprinted with permission from Simoens *et al.*, J. Infrared Millim. Terahertz Waves **36**, 961–985 (2015) [54]. Copyright 2015 Springer.

They predicted resonant (frequency-specific) and non-resonant (broadband) detection mechanisms, depending on the electron momentum relaxation time τ that defines the conductivity in the channel $\sigma = ne^2\tau/m$ (n, e, and m are the electron density, charge, and mass, respectively). Given an incident THz radiation at frequency ω, the resonant case occurs when $\omega\tau > 1$, that is to say, when the channel conductivity is large. In this case, provided that the channel length L is sufficiently small, the plasma waves reach the drain side of the channel, are reflected back, and create a standing wave. A wavelength-specific DC voltage is then developed between the drain and the source [302]:

$$\Delta U^R = \frac{e\tau^2}{L^2 m}\left[\frac{U_a^2}{4(\omega - m\omega_0)^2\tau^2 + 1}\right], \tag{31}$$

where $m = 1, 3, 5, 7, \ldots$. Experimental evidence of THz detection in the resonant regime was demonstrated with a III–V high-electron mobility transistor in Ref. [303].

In the non-resonant regime (when $\omega\tau < 1$), the plasma waves are overdamped and cannot fully reach the other side of the transistor channel. In this case, a DC photoresponse between the drain and the source still exists in the form of an exponential decay [300]:

$$\Delta U^{\mathrm{NR}} = \frac{U_a^2}{4U_0}[1 - \exp(-2x/l_c)], \tag{32}$$

where x is the distance from the source and l_c is the characteristic decay length (typically a few tens of nanometers [304]). This type of broadband detection occurs in silicon FETs.

The seminal work by Dyakonov and Shur sparked a series of experimental demonstrations of THz detection in FETs, first with III–V semiconductors [305–309], then, more recently, with InAs nanowire [310], graphene [311], and black phosphorus [312]. However, in the short term, the work on silicon-based FETs will probably have more impact on development of THz cameras thanks to the compatibility of silicon material with the standard CMOS-foundry process, thus enabling large scale array fabrication at lower costs.

THz detection with silicon FETs was first experimentally demonstrated in Refs. [313,314]. Their behavior was explained by using the non-resonant broadband detection mechanism of Dyakonov and Shur. In Ref. [61], it was shown that the NEP of silicon FETs (100 pW/$\sqrt{\mathrm{Hz}}$) was comparable to conventional THz detectors operating at room temperature (such as thermal detectors). In Ref. [315], using circuit theory, the authors described the non-resonant FET detection mechanism with the distributed resistive self-mixing concept, where the channel was modeled as a

Figure 28

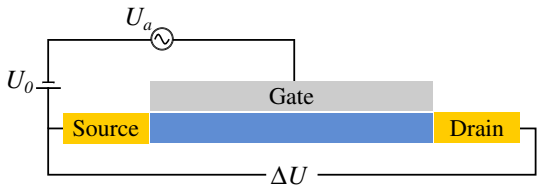

Schematic representation of the field-effect transistor used for THz detection. A DC voltage U_0 is applied between the gate and the source, while the incident THz radiation causes an alternating voltage U_a.

nonlinear resistance–capacitance (RC) transmission line [316]. This theoretical framework helped them to design an efficient 3×5 pixel array of FET detectors using 250 nm CMOS process technology [Fig. 29(a)]. Each pixel consisted of a patch antenna designed for 0.65 THz coupled to a FET detector and a voltage amplifier, achieving a minimal NEP value of 300 $\mathrm{pW}/\sqrt{\mathrm{Hz}}$. Using lock-in amplification, they imaged the inside of an envelope [Fig. 29(b)]. In Ref. [317], the same group demonstrated improvement in the image contrast by using a heterodyne detection scheme in transmission mode [Fig. 29(c)]. A reference THz source (local oscillator) was combined to the transmitted THz beam to image details of the inside of a tablet [Fig. 29(d)]. In Ref. [318], a similar heterodyne scheme was used in both transmission and reflection modalities with an antenna-coupled FET fabricated on 150 nm CMOS process technology [319].

In Ref. [304], Schuster *et al.* studied the performance of several THz FET detectors fabricated using 130 nm Si CMOS, with embedded bow-tie antennas of different geometries and configurations. They obtained record NEP (<10 $\mathrm{pW}/\sqrt{\mathrm{Hz}}$) and responsivity ($>5$ kV/W, without amplification) at 0.3 THz by reducing the size of a silicon substrate (to reduce absorption losses), by using a shorter channel length and by connecting the antenna to the gate and source (to avoid parasitic THz collection on the drain side). They also demonstrated imaging up to a frequency of 1.05 THz. In Ref. [320], multispectral THz imaging was demonstrated with silicon FETs fabricated

Figure 29

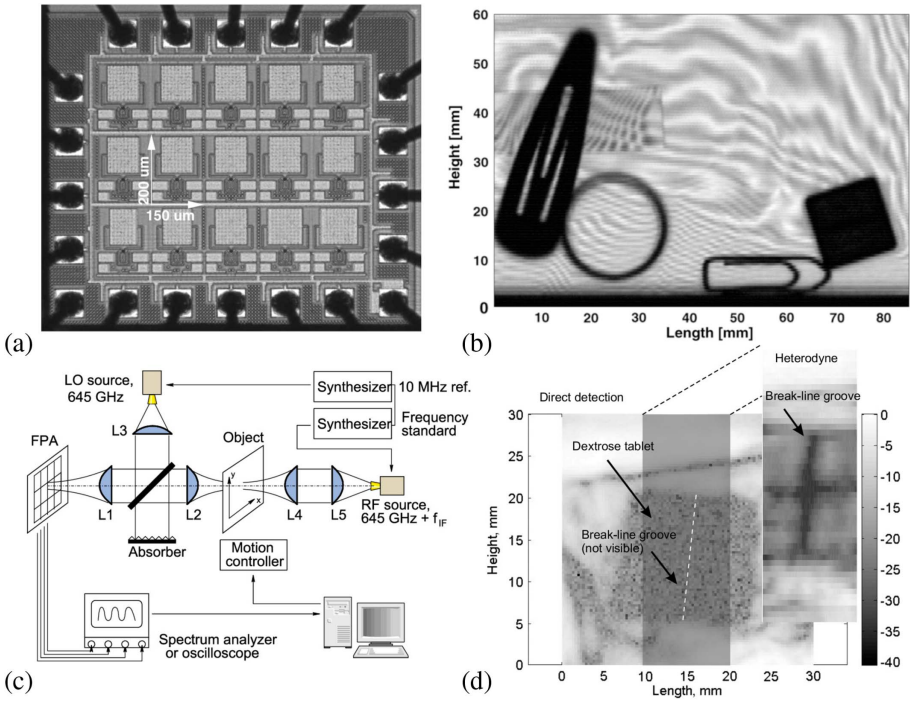

(a) Micrograph of the 3×5 array of FET developed in Ref. [315]. (b) THz radiation revealing the inside of an envelope. © 2009 IEEE. Reprinted, with permission, from Ojefors *et al.*, IEEE J. Solid-State Circuits **44**, 1968–1976 (2009) [315]. (c) Heterodyne detection scheme using a second source as a local oscillator [317]. (d) Image of a dextrose tablet wrapped in polyethylene foils. When compared to the direct detection mode, the heterodyne mode provides more contrast. Reprinted with permission from Glaab *et al.*, Appl. Phys. Lett. **96**, 042106 (2010) [317]. Copyright 2010 AIP Publishing LLC.

using a commercial 90 nm CMOS process. A record high frequency of 4.25 THz with a NEP of 110 pW/$\sqrt{\text{Hz}}$ was measured.

In the works reviewed above, the THz images were still obtained by mechanically scanning the sample, limiting the image acquisition time. However, the main advantage of using silicon FET is its compatibility with mainstream CMOS processing, which also enables on-chip integration with read-out electronics for mass fabrication of imaging arrays. Thus, in Refs. [63,321], Al Hadi and co-workers fabricated an array of 32×32 pixels using 65 nm CMOS process technology [Fig. 30(a)]. In addition to the ring antenna and the FET detector, each pixel included a reset circuit to clear the accumulated charges, an integration capacitor, and a differential amplifier. Each row was biased one at a time and the columns were consecutively selected with an external programmable logic device located inside the camera. The THz camera was packaged in a metal box with an integrated silicon lens for compact handheld applications [Fig. 30(b)]. The authors demonstrated 0.65 THz video recording using a focal-plane array configuration [Fig. 30(c)]. A digital still taken from the 24 fps video recording is presented in Fig. 30(e). The authors measured a minimum detectable power of 20 nW. Recently, Zdanevičius *et al.* were able to measure a minimal power of 1.4 nW at 30 fps [322]. The noise was reduced by using a parallel read-out architecture to simultaneously interrogate 48 pixels of their 24×24 pixel array.

Figure 30

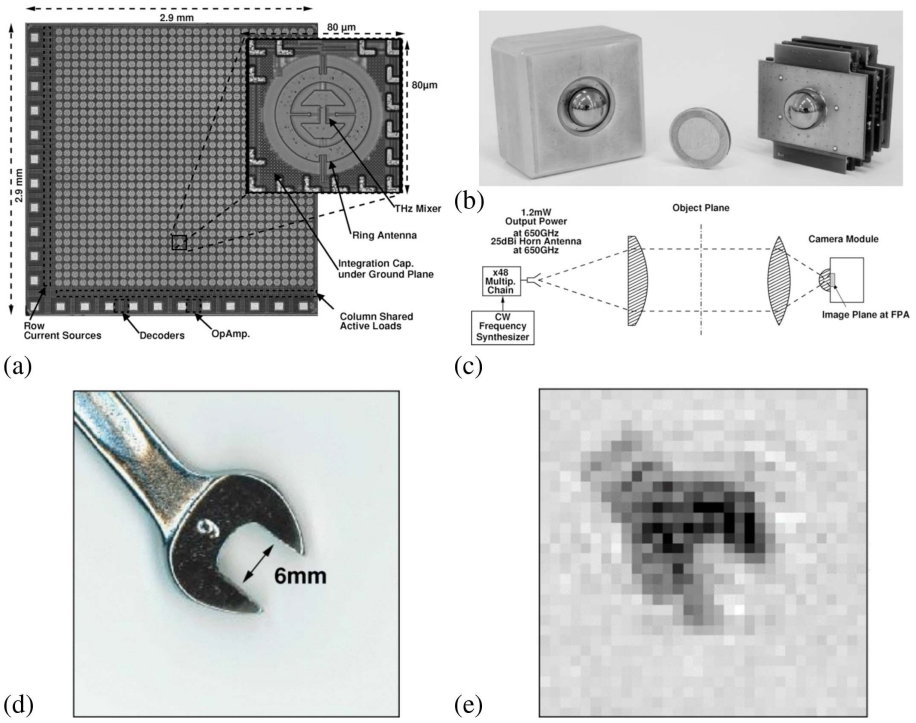

(a) Micrograph of the 32×32 focal-plane array developed in Ref. [63]. (b) Photograph of the THz camera device. (c) Transmission mode imaging setup in a focal-plane array configuration. (d) Photograph of a 6 mm wrench and (e) THz still image obtained from a 25 fps video stream at 650 GHz. © 2012 IEEE. Reprinted, with permission, from Hadi *et al.*, IEEE J. Solid-State Circuits **47**, 2999–3012 (2012) [63].

4.3. Section Summary and Future Directions

As we saw in this section, several requirements are necessary to enable mass deployment of THz cameras in various applications. They must operate at room temperature without the need of cryogenic cooling. Their fabrication must be compatible with modern standard process technologies, such as the CMOS process technology. Their size, their weight, and their power consumption should be relatively small for easy integration into optical systems. Finally, they should be sensitive enough to allow recording of a THz signal at high frame rate, eventually without any active THz source. In the past decade, two major types of THz cameras have attracted attention: THz thermal cameras and THz FET-based cameras.

The first demonstrated THz cameras recorded an image based on the heat generated by THz radiation. There are three types of thermal detectors. The Golay cell measures the pressure change induced by the thermal expansion of a gas. Because of their simple operating principle, they are routinely used to measure THz powers. However, they are difficult to integrate into dense arrays of detectors and do not constitute a valid choice for THz cameras. Pyroelectric sensors detect the generated electrical polarizability of certain crystals when they are heated. Unlike Golay cells, pyroelectric cameras are commercially available. However, their low sensitivity makes them less attractive for THz imaging.

Bolometers detect the change in a temperature-dependent resistance. The main components of a bolometer are the absorber that generates the heat, the resistive thermometer that outputs the voltage, and the thermal link that dissipates the heat to the heat sink. Microbolometers are arrays of bolometers mounted onto a read-out integrated circuit for focal-plane camera operation. Microbolometers can reach impressive sensitivities when cryogenically cooled due to the suppression of background thermal noise. However, room temperature operation with remarkable sensitivities (minimum detectable power of 100 pW) has been achieved thanks to recent advances in the design, such as the inclusion of a Fabry–Perot cavity, antennas, and metamaterials to increase the absorbed THz radiation.

THz FET-based cameras measure a rectified voltage after interaction of the THz radiation with a plasma wave in a transistor channel. The theoretical work predicted resonant (frequency-specific) and nonresonant (broadband) detection mechanisms. There were numerous demonstrations of THz FET-based detectors, using a variety of materials ranging from III–V semiconductors to graphene layers. However, in the short term, silicon-based FETs will probably have more impact on the development of THz cameras thanks to the compatibility of silicon material with the standard CMOS-foundry process. This key advantage could enable large-scale array fabrication at reduced costs. The behavior of silicon FET can be explained using the nonresonant broadband detection mechanism, as well as the distributed self-mixing concept where the channel is modeled as an RC transmission line. Record NEP in the range of $\mathrm{pW/Hz^{1/2}}$ was obtained by using a bow-tie antenna to couple the incident THz radiation at 0.3 THz, while broadband detection was used to measure frequencies up to 4.25 THz with an NEP of 100 $\mathrm{pW/Hz^{1/2}}$. As for camera operation, minimal detectable power in the range of 1–20 nW has been reported with up to 1024 pixels.

In addition to silicon-based FET cameras, future research directions include the development of a THz emitter on a silicon platform. This would enable all-silicon THz imaging systems attractive toward imager implementation at reduced costs. Several silicon-based THz sources have already been demonstrated in the literature: 0.19 mW at 0.28 THz [323], 0.81 mW at 0.34 THz [324], 1 mW at 0.53 THz [325], and 2 mW at 0.32 THz [326]. We expect increase in the power outputs and operation at higher THz frequencies. For THz imaging, there are several important advantages of using such

sources. These types of sources can be used as local oscillators in heterodyne detection schemes for coherent imaging [326], therefore increasing the image contrast. They could also allow fabrication of on-chip transceivers, where the close proximity of the emitter and detector allows subwavelength imaging in the near-field region [182]. Finally, distributed arrays of silicon emitters could allow dynamic electronic THz beam steering to increase the field of view of an imaging system [323].

We would like now to discuss on the potential of THz cameras and compare it with THz-TDS imaging systems. Although the development of THz cameras is crucial for many applications, we believe that it is not directly competing with THz-TDS imaging systems. While THz cameras provide non-discriminatory intensity-based imaging, we expect that amplitude-based THz-TDS imaging systems will develop into niche sectors, where the application will drive the system design. Indeed, as we saw in Section 2, the ability of THz-TDS to provide spectroscopic information in addition to THz imaging proves to be useful in various applications, for example, in quality control of large-area graphene or pharmaceutical applications.

5. THZ IMAGING WITH SINGLE-PIXEL DETECTORS

Historically, due to high cost and difficulty of manufacturing multipixel THz cameras/arrays, many techniques have been proposed to enable real-time THz imaging using single-pixel detectors. Such techniques are mature and can be used to build cost-effective industrial imaging systems. Additionally, they have a large modernization potential, as they could be greatly improved when substituting a single-pixel detector with 1D or 2D THz pixel arrays (when they would become commercially available). Finally, single-pixel imaging is often phase sensitive, allowing measurement of both amplitude and phase information of the electric field with very high SNR, which is one of its key advantages over intensity-only imaging using multipixel THz arrays. Therefore, even with an advent of multipixel THz arrays, further development of single-pixel techniques remains highly pertinent. In this section, we review the three most prominent single-pixel imaging techniques: 1) mechanical beam steering, 2) single-pixel imaging and compressive sensing, and 3) spectral/temporal encoding and Fourier optics.

5.1. Mechanical Beam Steering

In a conventional THz imaging system, the sample is positioned at the focal point of focusing optics. Then, using a single-pixel detector, the THz image is constructed by physically moving the sample in the focal plane (see Fig. 15). However, in many situations, sample displacement is not desirable or even possible. Instead of moving the sample, one can steer the THz beam over the sample. In principle, one could use spatial light modulation [327–330], special THz generation techniques [331–333], or a distributed array of THz emitters [323,334] to accomplish this task. However, most of the demonstrated applications for real-time THz imaging use mechanical beam steering. In the following, we review two main types of mechanical devices: (1) the oscillating mirror with an f-theta scanning lens and (2) the Gregorian reflector system.

5.1a. Oscillating Mirror with an f-Theta Scanning Lens

The f-theta lens is a specially designed lens that provides a flat image plane for a range of input angles [335–338]. Also known as a scanning lens, the f-theta lens is often used along with galvanometers to convert an incident angle into a linear position in the focal plane [Fig. 31(a)]. In Ref. [336], Katletz *et al.* combined flat mirrors mounted on a two-axis galvanometer and a rotationally symmetric f-theta scanning lens to steer the THz beam in two dimensions. A maximal scanning area of 100 mm × 100 mm

was collected in 1–2 min at the rate of 1 line/s, mainly limited by the speed of the galvanometer. However, since the system was based on THz-TDS, the movement of the delay line was still necessary. In Ref. [337], Yee *et al.* used similar beam steering with ECOPS to obtain the temporal dimension (see Section 3.2c). A time delay window of 52 ps was acquired in 1 ms, which led to the acquisition of 100 mm × 100 mm in 40 s. The authors also demonstrated 3D THz TOF imaging.

To avoid the need for a delay line, in Refs. [335,338], Ok *et al.* used a 210 GHz source with an output power of 75 mW to demonstrate applications in food quality inspection. In Ref. [335], a combination of a single-axis galvanometer and an *f*-theta lens were used to get the first spatial dimension, while the second was obtained with a linear translation stage (conveyer belt configuration). A 100 mm × 150 mm image was acquired in 15 s, limited again by the galvanometer speed. To further increase the acquisition rate, in Ref. [338], a polygonal mirror was designed and fabricated to replace the galvanometer [Fig. 31(b)]. With its four faces, one line can be acquired at 80 Hz, 4 times the rotor speed. To demonstrate food inspection, the authors buried crickets in noodle flour [Fig. 31(c)]. A transmission image of 288 mm × 207 mm was acquired in only 3.13 s [Fig. 31(d)] and compared with a conventional raster-scan image obtained in 42 min [Fig. 31(e)].

In Refs. [164,339], a fast two-axis scanning mirror was used to steer a 2.5 THz beam emitted from a THz QCL. The mirror could tilt in two directions and was placed at a focal length from a high-density polyethylene lens. The THz beam was scanned over a 40 mm diameter region by spiral scanning of the mirror. An image with 0.5 mm resolution was acquired in 1.1 s. THz computed tomography was demonstrated in 87 s by rotating the object by 180 deg in steps of 3 deg.

Figure 31

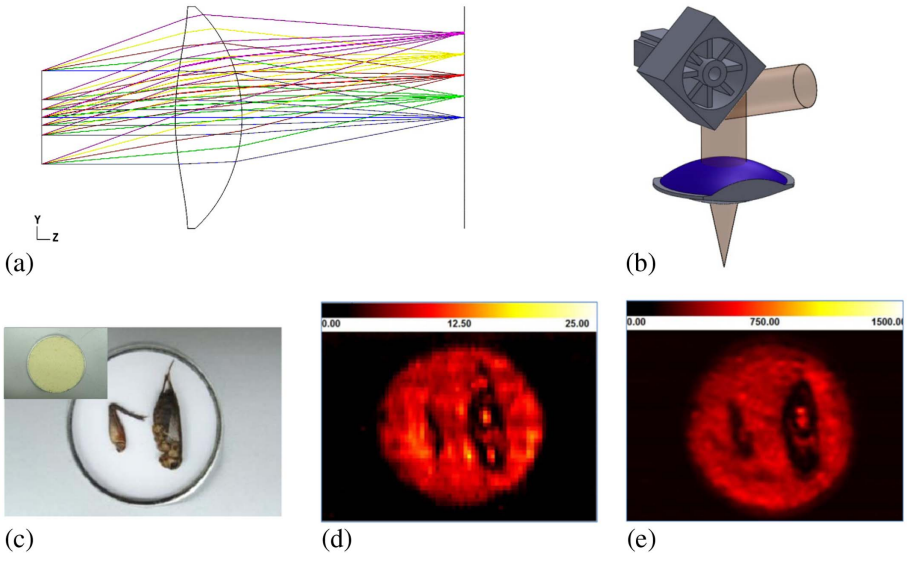

(a) *f*-theta scanning lens used in Ref. [335]. The colored lines correspond to an input angle and are focused on a single point in the focal plane. Adapted with permission from [335]. (b) Polygonal mirror used in Ref. [338] to replace the galvanometer. (c) Photographs of the crickets. Inset shows the crickets buried under the noodle flour. (d) Transmission image obtained in 3.13 s with the *f*-theta lens and the polygonal mirror and (e) obtained in 42 min with a conventional raster-scan. Adapted with permission from [338].

5.1b. Gregorian Reflector System

Security and defense are potential applications of THz imaging that has attracted much of attention recently. Since many textiles are transparent to THz, concealed objects can be detected without exposure to ionizing radiation. In the *f*-theta lens that we previously described, the field of view and the distance between the imaging optics and the sample were limited to a few centimeters, which is not sufficient for stand-off security applications. In this subsection, we review the Gregorian reflector system that addresses this problem.

Llombart and co-workers proposed in Refs. [340–342] to use a confocal ellipsoidal reflector system in reflection geometry to mechanically scan a sample with a THz beam. Their transceiver system was based on a previously developed frequency-modulated continuous wave (FMCW) radar at 675 GHz [343,344]. The scanning optics included two paraboloid reflectors sharing a common focal point, similar to a Gregorian telescope. Between the two reflectors, a planar mirror with a diameter of 13 cm was rotated by ± 2.5 deg in elevation and azimuth direction [Fig. 32(a)]. The mirror rotation allowed scanning of the sample on a 50 cm $\times$ 50 cm area. The paraboloid reflectors' characteristics were chosen to provide a 25 m stand-off distance for which the beam spot size was 1 cm. Imaging at 1 fps is enabled by a rotary mirror oscillating at 31.25 Hz. Imaging of hidden PVC pipes behind a subject's jacket was demonstrated [Figs. 32(b)–32(d)]. In Ref. [345], a bifocal Gregorian reflector system was proposed to increase the field of view without impacting the beam quality or imaging speed. Geometrical optics calculations were used to substitute the ellipsoidal reflectors by specially designed shaped surfaces, which were able to increase the field

Figure 32

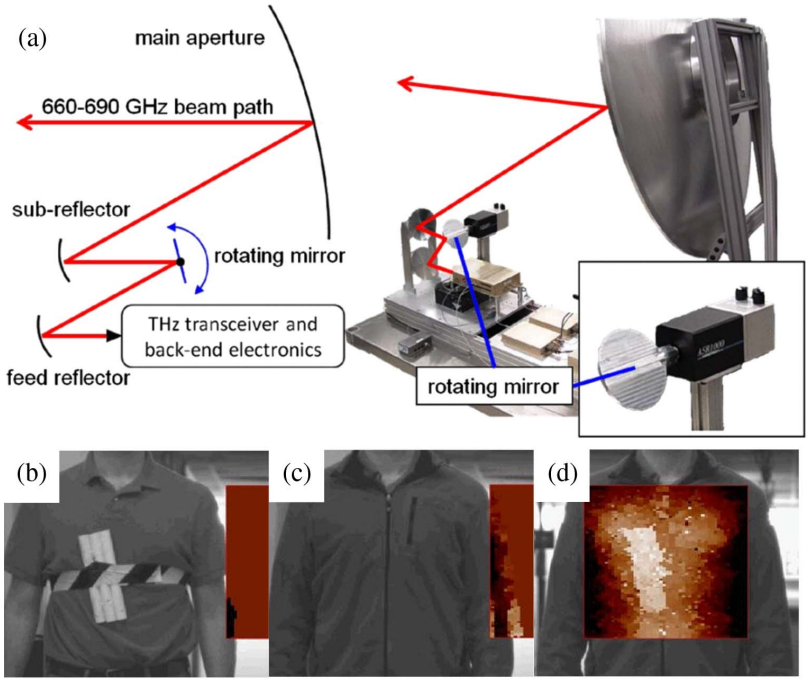

(a) Gregorian reflector system with a rotating mirror to scan the subject positioned at 25 m. (b), (c) Photograph of the hidden PVC pipes inside the subject's jacket. (d) THz image obtained in 1 s with the FMCW radar at 675 GHz. © 2011 IEEE. Reprinted, with permission, from Cooper *et al.*, IEEE Trans. Terahertz Sci. Technol. **1**, 169–182 (2011) [342].

of view by 50%. Finally, most recently, similar opto-mechanical devices are combined with THz cameras to provide meter-scale field of view at 25 fps [346,347].

5.2. Single-Pixel Imaging and Compressive Sensing

In the past, computational imaging techniques have been developed to enable imaging with single-pixel detectors. One such technique is compressive sensing. There, instead of directly imaging a sample, the detector performs a series of measurements of the transmitted intensity through a sample covered with different pixelated masks [Fig. 33(a)]. The measured data set can be mathematically described by using matrix–vector multiplication [348]:

$$\bar{y} = \Phi \bar{x}, \tag{33}$$

where $\bar{x}$ is the vectorized version of a sample (local sample transmission), $\bar{y}$ is the corresponding vector of measured intensities by a detector, and the matrix Φ contains the information about the concatenated collection of the vectorized masks.

For example, to mimic a raster-scan, an aperture can be moved in the object plane. Every position of the aperture can be described by a mask. In Fig. 33(b), we present 16 masks for a sample of 4×4 pixels. For each mask, a vectorized version of the aperture ($\bar{\phi}_{\mathrm{RS}}$) is constructed with values of 0 and 1 corresponding to opaque or transparent regions of the mask, respectively. The matrix Φ_{RS} is then constructed by stacking the vectors $\bar{\phi}_{\mathrm{RS}}$. For the raster-scan, the measurement matrix is simply an identity matrix [Fig. 33(c)]. However, the identity matrix corresponds to a very poor choice of Φ since the aperture blocks most of the light, and therefore the useful signal is buried in noise.

In fact, there are more judicious choices for the matrix Φ. One of the most commonly used sets of masks is derived from the Hadamard basis, which was shown to provide the best SNR [349]. In Fig. 33(d), we present the 16 Hadamard masks, while the corresponding Hadamard matrix is shown in Fig. 33(e). Other possible choices of Φ include the Fourier or wavelet basis.

In the measurement process within single-pixel imaging, Φ is predetermined and $\bar{y}$ is measured. The sample image $\bar{x}$ can then be recovered by performing the matrix inverse $\bar{x} = \Phi^{-1}\bar{y}$. Mathematically, the matrix inversion requires that the number of masks must be equal to the number of pixels in the object.

The compressive sensing theory proposes to use a number of masks smaller than the number of pixels, while employing a pseudo-inversion in place of a true matrix inversion. In general, images are compressible (sparse) under certain representations. In fact, this compression property is commonly used to reduce the size of images in computers. For example, JPEG compression uses the discrete cosine transform, which takes advantage of the difficulty of the human visual perception system to distinguish features with high spatial frequency components [350]. In JPEG compression, those frequencies are equated to zero in postprocessing *after* the image is taken with a digital camera.

In compressive sensing, the image is compressed directly *during* the measurement step [351,352], and it essentially allows reconstruction of an image with a number of measurements that is smaller than the number of pixels [353], which at first glance seems to defy the Nyquist requirement. In compressive sensing imaging, while Eq. (33) becomes under-determined and an infinite number of solutions is possible, the pseudo-inverse can still be defined, for example, in the least square sense so as to minimize the norm of the difference between the right and left parts of Eq. (33) [354].

In more detail, compressive sensing theory indicates that it is possible to recover an approximation of $\bar{x}$ from a number of measurements smaller than the image size, given

that the signal $\bar{x}$ is sparse under a certain representation [348]. To ensure robust signal recovery even when noise is introduced in the measurements, the sensing matrix Φ must respect the restricted isometry property [355]. This property ensures that column vectors taken from arbitrary subsets of a representation basis are almost orthogonal. For example, the measurement matrix Φ can take the form of random subsets of the Fourier, Hadamard, or wavelet basis. Remarkably, even random binary apertures derived from a Bernoulli distribution give satisfactory reconstruction results in most cases [351]. Furthermore, if Φ respects the restricted isometry property, then the object $\bar{x}$ can be reconstructed with high probability using just $M \geq O(K \log(N/K))$ random measurements, where K is the number of nonzero coefficients.

Then, if the measurement $\bar{y}$ originates from a highly sparse object $\bar{x}$, the compressive sensing problem can be formulated as searching for the sparsest signal $\bar{x}$ that produces $\bar{y}$. This leads to a minimization formulation with the l_0-norm:

Figure 33

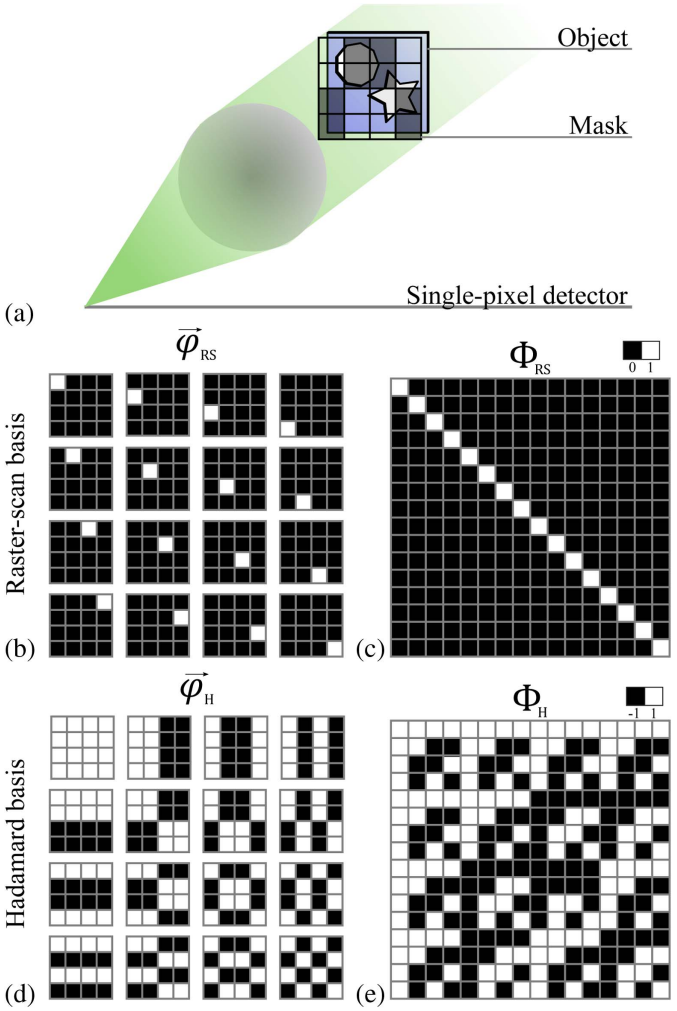

(a) Experimental setup for imaging with a single pixel using a mask aperture. (b) Raster-scan basis and set of 16 masks (φ^i_{RS}) for a 4×4 sample. (c) Measurement matrix Φ_{RS} constructed by concatenating the vectorized versions of the masks φ^i_{RS}. (c) Hadamard basis and set of 16 masks (φ^i_H) and (e) corresponding measurement matrix Φ_H.

$$\text{minimize } \|\bar{x}\|_0 \text{ subject to } \bar{y} = \Phi\bar{x}, \tag{34}$$

where $\|\bar{x}\|_0$ is the l_0-norm, i.e., the number of non-zeros in $\bar{x}$. However, such a minimization problem is NP-hard in general and, therefore, is computationally prohibitive [356]. A common alternative is to use the l_1-norm, for which tractable programming is possible:

$$\text{minimize } \|\bar{x}\|_1 \text{ subject to } \bar{y} = \Phi\bar{x}. \tag{35}$$

It can be shown that, if Φ satisfies the restricted isometry property, then Eq. (35) (l_1-norm) shares similar solutions with Eq. (34) (l_0-norm). This type of minimization is known as the basis pursuit [351,352,357]. Among the other types of optimization algorithms, we note the basis pursuit with inequality constraints, where a bound is added in the constraint to include additive noise:

$$\text{minimize } \|\bar{x}\|_1 \text{ subject to } \|\bar{y} - \Phi\bar{x}\|_2 < \varepsilon. \tag{36}$$

The greedy algorithms are alternatives to the optimization-based algorithms [358]. In these methods, the solution $\bar{x}$ is constructed iteratively by selecting columns of Φ depending on their correlation with the measurements $\bar{y}$. For example, in the orthogonal matching pursuit [359], the solution is found by selecting the column of Φ that is most correlated to a residual, defined by subtracting a partial estimate to the measurements $\bar{y}$. The CoSamp algorithm is also a commonly used greedy algorithm [360]. We note that many other types of algorithms can be used to solve the compressive sensing problem. Readers may find excellent reviews on this topic in Refs. [355,358,361].

In the following, we review compressive sensing in the context of THz imaging. Apart from assuming sparsity of the imaged object, the compressive sensing theory does not specify the nature of the measurement. The measured data can be amplitude, phase, intensity, and so on. Therefore, compressive sensing can also be used with incoherent measurements as is commonly done in the visible range. In the following, some works used incoherent measurements in the THz range (for example [362–364]). Others used the broadband amplitude and phase measurement obtained from a THz-TDS system to reconstruct an image per THz frequency (hyperspectral imaging) or used the complex spectral information to improve image quality.

5.2a. THz Imaging with Compressive Sensing

Chan *et al.* were the firsts to propose using compressive sensing theory for THz imaging [365,366]. In their first implementation [367], the measurements were performed in the Fourier plane, and the image was reconstructed using a 2D spatial inverse Fourier transform. The object mask was placed in the front focal plane of a lens and the detector was scanned in the back focal plane [Fig. 34(a)]. Using THz-TDS, both amplitude and phase at 0.2 THz were measured over an area of 64×64 mm, at 1 mm intervals (4096 pixels). Then, assuming sparsity of the image, they used the compressive sensing theory to select random points in the Fourier plane, therefore using a random subset of the Fourier basis function. Using the spectrally projected gradient algorithm [357], they demonstrated successful image reconstruction that used only 12% (500 pixels) of the original data points [Figs. 34(b) and 34(c)].

In the first experimental approach, it was still necessary to mechanically move a single-pixel detector in the Fourier plane. In their second experiment [366], the authors used a set of random binary metal masks in the object plane and a fixed single-pixel detector at the center of the Fourier plane [Fig. 34(d)]. The binary masks formed a basis from which a 1024 pixel image was reconstructed using as little as 300 (29%) measurements at a frequency of 0.1 THz. Thanks to the ability of THz-TDS to

measure both the amplitude and the phase of the THz electric field [368], the authors also demonstrated phase contrast imaging of a rectangular hole half-covered with transparent plastic tape. While the amplitude of the reconstructed image shows no difference between the plastic and the air regions [Fig. 34(e)], the phase image clearly demonstrates contrast between the two regions [Fig. 34(f)].

The prospect of reducing the number of measurements by using only a single-pixel detection scheme resulted in a spurt of activity in compressive sensing applied to THz imaging. In Ref. [369], instead of random binary metal masks, Shen *et al.* used a set of optimized masks calculated to approximate the Karhunen–Loeve transform [370]. They showed that, using the same number of masks, the optimized masks gave better images than random masks. Also, using a broadband THz spectrum, they demonstrated spectroscopic contrast of lactose monohydrate power and polyethylene, owing to the fact that lactose has absorption peaks at 0.54 and 1.38 THz.

In Ref. [371], the authors used additional constraints in the optimization algorithm to obtain images of better quality. Thus, they used the assumption that the phase is generally a piecewise slow-varying function in the object plane and that the object is piecewise homogeneous with a uniform thickness. Additionally, using the information across all the THz frequencies, they showed improvement in the quality of the reconstructed image.

In the abovementioned works, the metallic masks were manually placed in the object plane. In Ref. [372], Shen *et al.* used a spinning metallic disk with holes as a mask set [Figs. 35(a) and 35(b)]. They used a THz-TDS setup and they fixed the delay line to the position of the main peak in time domain. They showed reconstruction of a THz

Figure 34

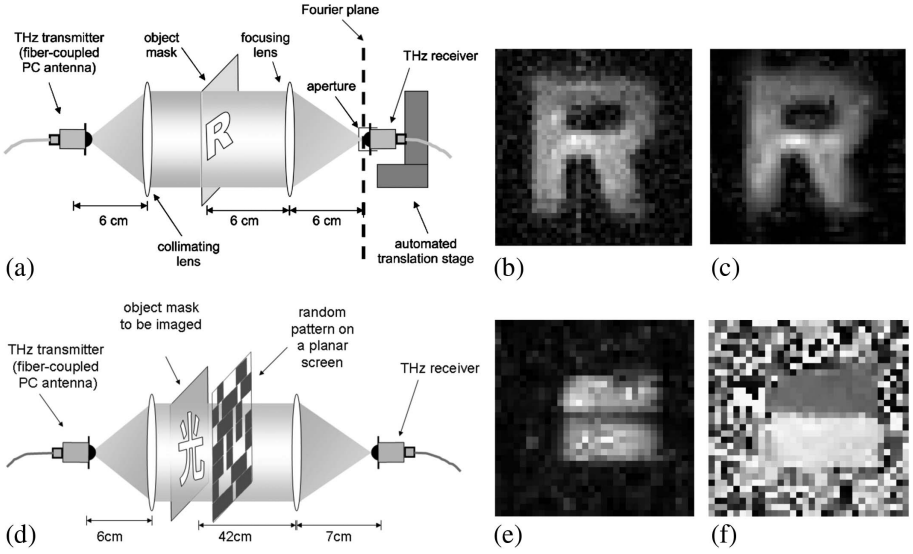

(a) Experimental setup for the Fourier transform compressive sensing reconstruction. (b) Reconstruction using 4096 measurements (100%) and (c) 500 measurements (12%) using compressive sensing. Reprinted with permission from [365]. Copyright 2008 Optical Society of America. (d) Experimental setup for the random binary masks compressive sensing reconstruction. Complex reconstruction of a 1024 pixels objects using 400 measurements (39%): (e) amplitude and (f) phase. Reprinted with permission from Chan *et al.*, Appl. Phys. Lett. **93**, 121105 (2008) [366]. Copyright 2008 AIP Publishing LLC.

image in 80 s by continuously rotating the mask at a speed of 5 deg/s [Figs. 35(c) and 35(d)]. They noted that the limitation in the acquisition speed was the SNR.

Three-dimensional imaging is also possible using single-pixel imaging. In Ref. [373], Jin *et al.* demonstrate pulse-echo reflectance tomography using compressive sensing applied to the scattering equation derived from the scalar wave equation [138]. In Ref. [165], THz-CT was performed using compressive sensing and the SART algorithm with Hadamard masks. In Ref. [137], Cho *et al.* demonstrated TPI using block-based compressed sensing. The general idea of the block-based approach, developed in Ref. [374], is to divide the original object into several regions and to simultaneously apply the same binary operator in each region. This results in a reduction of the computational burden associated with the conventional compressive sensing, which allows computation of the image directly during the acquisition.

5.2b. Optical Spatial Light Modulation and Near-Field Imaging

To forgo completely the use of mechanically moving parts, the current trend in THz imaging within compressive sensing modality is to use spatial light modulation (SLM). There are many methods to spatially modulate the THz beam, and intensive research on this subject is still ongoing (see, for example, reviews on THz modulation in Refs. [375–378]). The general idea is to modulate the amplitude/phase of the transmitted or reflected THz beam, thus simulating the action of a mask.

Optically based modulation for compressive sensing THz imaging has been reported in Ref. [328]. There, the THz beam was spatially modulated with an optically controlled SLM made of a computer controlled digital light processing (DLP) projector that redirected light from an incoherent 8 W mercury arc lamp onto a photosensitive semiconductor material. In particular, apertures were optically inscribed onto a high-resistive silicon wafer with a thickness of 500 μm. Within the silicon, the free carriers induced by the absorbed photons increase the conductivity and, hence, the absorption coefficient [379]. In Ref. [328], the reconstruction was made by raster-scanning a single aperture, which is not the efficient type of mask for compressive sensing imaging. In Refs. [380–382], the authors optically pumped Hadamard masks in the silicon wafer, while in Ref. [383], random masks were used on a germanium wafer.

Figure 35

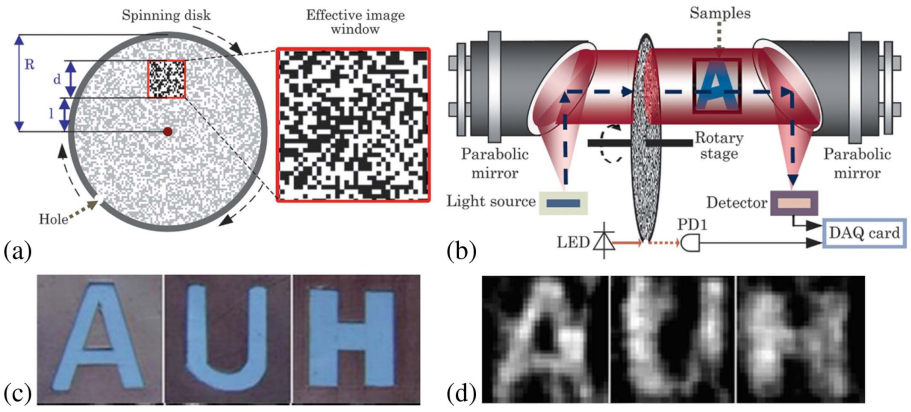

Real-time THz compressive sensing with a spinning disk. (a) Schematic of the spinning disk and (b) experimental setup. (c) Photograph of the sample and (d) reconstruction of a 32 × 32 pixel image using 160 measurements. Reprinted with permission from [372]. Copyright 2012 Optical Society of America.

In Ref. [364], using only intensity measurements, phase-sensitive imaging at 690 GHz was demonstrated with the PhaseLift algorithm presented in Ref. [384].

In Ref. [385], Stantchev *et al.* performed single-pixel near-field imaging using optically based modulation. They used an 800 nm, 100 fs optical pump onto a highly resistive 115 μm thick silicon wafer. The binary patterns were generated by reflecting the pump beam onto a digital micromirror device (DMD) [Fig. 36(a)]. Since the distance travelled by the THz beam in the silicon wafer was smaller than the wavelength, they were able to record an image before far-field Fraunhofer diffraction occurred. They demonstrated a resolution of 103 μm ($\sim\lambda/4$), significantly smaller than the 375 μm peak wavelength of the THz pulse [Figs. 36(b) and 36(c)]. Finally, by imaging a circuit board [Fig. 36(d)], they showed that the polarization of the THz pulse affected the resolution. They observed that the subwavelength conducting wires were more clearly observed when the THz radiation was parallel to the wires [Figs. 36(e) and 36(f)]. In Ref. [386], they used a similar THz near-field imaging system to map the photoconductivity of a graphene sheet.

In Ref. [387], the same group demonstrated that the thickness of the silicon plate plays a crucial role in determining the resolution of the reconstructed image. They experimentally demonstrated resolutions of 154, 100, and 9 μm ($\lambda/45$ at 0.75 THz) for thicknesses of 400, 110, and 6 μm, respectively [Figs. 37(a)–37(c)]. Then, they used adaptive sampling to further reduce the number of required measurements. Using the Haar wavelet decomposition [388], they performed a coarse edge identification to

Figure 36

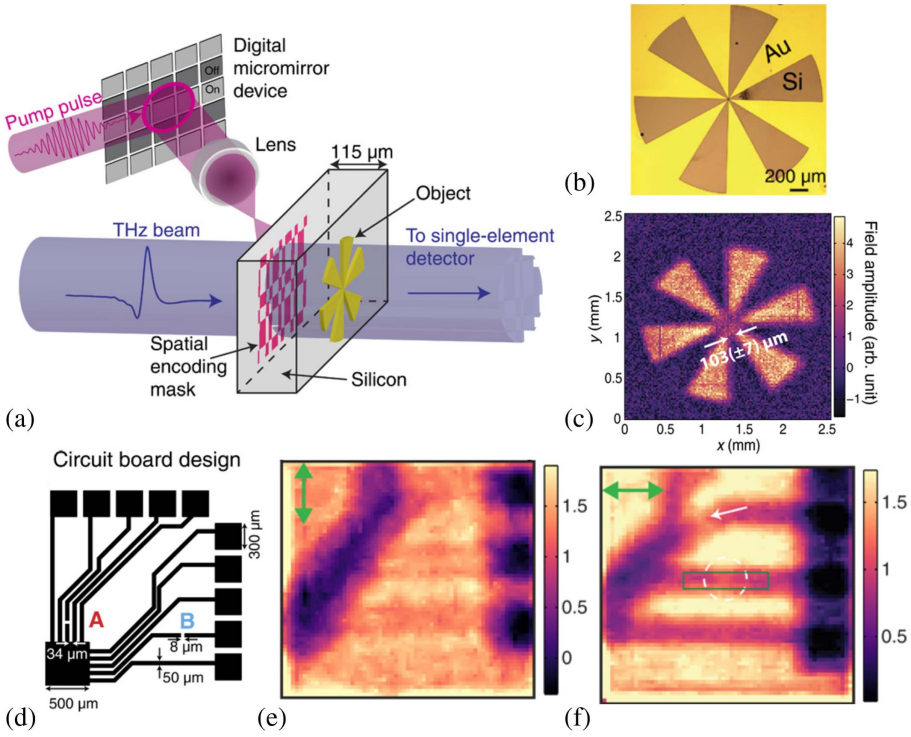

(a) Experimental setup using a silicon wafer and a digital micromirror device to generate the binary patterns. (b) Optical image of a metallic star and (c) reconstruction using Hadamard masks. (d) Schematic of a circuit board design. (e) Hadamard reconstruction of the region in (b) using vertical and (f) horizontal polarizations. Reproduced from [385] under the terms of the Creative Commons Attribution 4.0 License. With copyright permission.

determine where to sample with higher resolution. In Figs. 37(d)–37(f), comparison of their adaptive sampling algorithm with standard compressive sensing revealed that, with the same number of measurements, adaptive sampling outperforms compressive sensing by increasing the SNR.

5.2c. Metamaterial-Based SLM and Multiplexed Mask Encoding

Direct electronic SLM is desirable to reduce the complexity associated when adding a dedicated optical source to optically pump the semiconductor wafer [389]. In Ref. [390], instead of using an optically based SLM, Watts *et al.* introduced an active metamaterial SLM [Figs. 38(a) and 38(b)] originally reported in Refs. [391,392]. The metamaterial SLM was electrically controlled to allow phase-sensitive mask encoding. By measuring the phase of a detected signal with a lock-in amplifier, instead of simply measuring a binary mask, the authors were able to measure and symbolically represent negative and positive values with the in-phase and out-of-phase electrical signals. This allowed reducing the overall noise when using Hadamard masks. Furthermore, the metamaterial SLM allowed rapid changes of the binary masks. By displaying 45 masks for 22.4 ms each, they were able to demonstrate video recording at 1 fps [Figs. 38(c)–38(f)].

The possibility of using phase information in mask encoding and signal led to the idea of multiplexed mask encoding. The concept is summarized by the constellation

Figure 37

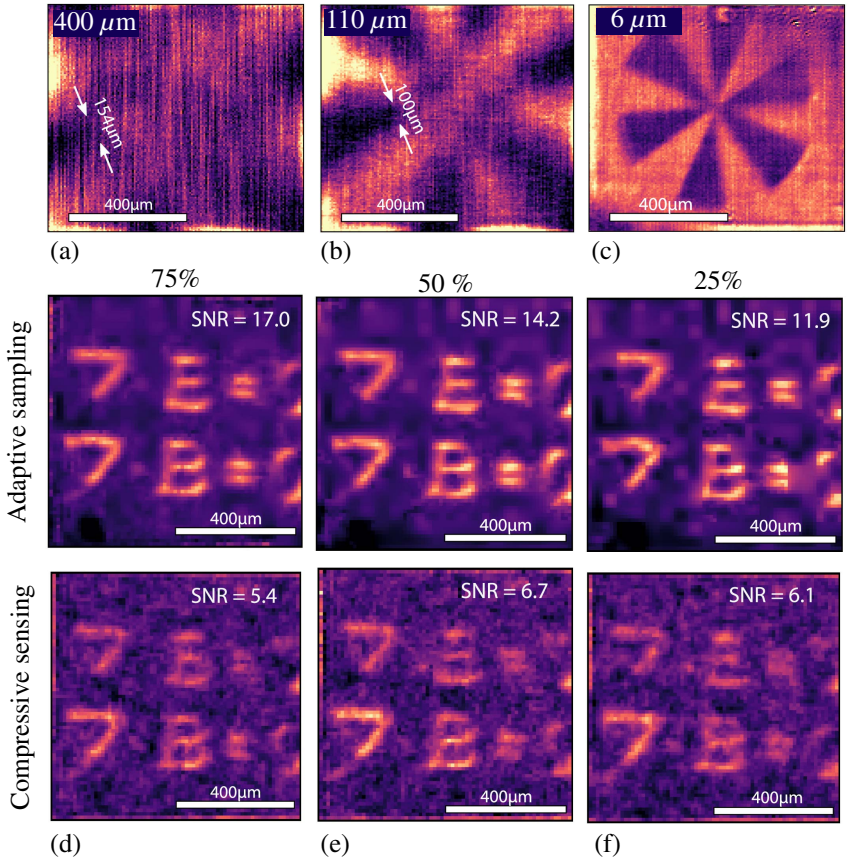

Improvement of the resolution by using thinner silicon wafer: (a) 400 μm, (b) 110 μm, and (c) 6 μm thick wafers. Comparison of reconstruction using adaptive sampling and compressive sensing, with (d) 75%, (e) 50%, and (f) 35% of the measurements required by the Nyquist theorem. Adapted with permission from [387].

diagrams in Figs. 39(a) and 39(b). Thus, in Ref. [390], Watts *et al.* used in-phase and out-of-phase electrical signals to encode symbolically $\{+1\}$ and $\{-1\}$ values in the mask [2-phase-shift keying in Fig. 39(a)]. As in any communications system, the idea can be extended by using electrical signals with different phase values to symbolically represent more states. Consequently, multiple masks can be encoded simultaneously to further reduce the acquisition time. In Ref. [363], Nadell *et al.* demonstrated the encoding of two masks in parallel using quadrature amplitude modulation [Fig. 39(b)]. In practice, they used square waves with phases: $\{\pi/4; 3\pi/4; -3\pi/4; -\pi/4\}$ to represent four possible combinations of symbols: $\{1, 1\}$, $\{-1, 1\}$, $\{-1, -1\}$, and $\{1, -1\}$, where the first index corresponds to the value of the first mask and the second index the value of the second mask. Then, by coherently measuring the phase of the signal, the authors could acquire two elements of $\bar{y}$ in the time that only one element can be acquired using conventional mask change. By comparing the obtained image of their quadrature amplitude modulation [Fig. 39(c)] to a conventional 2-phase-shift keying [Fig. 39(d)], they measured less than 5% difference in the averaged l_2-norm.

In Ref. [362], the same group demonstrated frequency-division multiplexing with metamaterials. The idea was to encode simultaneously different masks using square waves of different frequencies [Fig. 39(e)]. To avoid crosstalk, the frequencies were selected such that they were all mutually orthogonal:

$$\int_0^{\tau} g_m(t) g_n(t) \mathrm{d}t = 0 \quad \text{for } m \neq n, \tag{37}$$

Figure 38

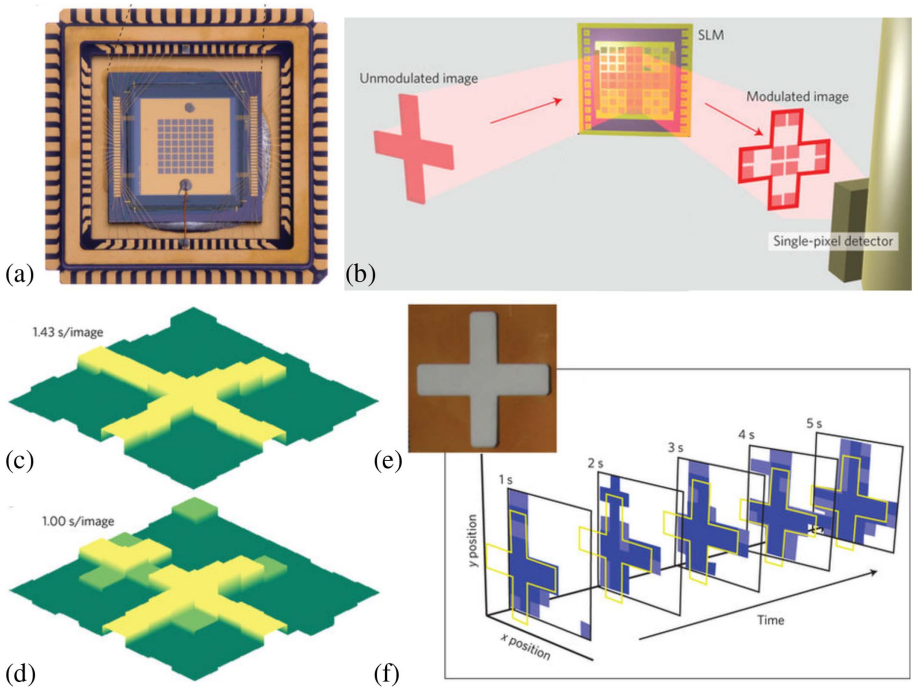

(a) Metamaterial SLM and (b) experimental setup. (c) Reconstructed object at 0.7 fps and (d) 1 fps of (e) a metallic cross. (f) Five frames of a 1 fps movie reconstructed with 45 masks displayed for 22.4 ms on the SLM. Reprinted by permission from Macmillan Publishers Ltd.: Watts *et al.*, Nat. Photonics **8**, 605–609 (2014) [390]. Copyright 2014.

where τ is the integration time of a lock-in amplifier and $g(t)$ is the square waveform. In Ref. [362], up to four frequencies were selected for the image reconstruction [Fig. 39(f)]. As the number of frequencies n_f increased, the total acquisition time decreased as $1/n_f$ [Fig. 39(g)].

In principle, both frequency and phase multiplexing can be used at the same time to increase the number of channels and reduce the overall acquisition time. Eventually, when the number of channels equals the total number of pixels, the image can be acquired in a one-shot process. In practice, as in any communications system, the total number of channels is limited by the noise floor. Consequently, as the acquisition time decreases, so does the overall SNR.

5.3. Spectral/Temporal Encoding and Fourier Optics

In this section, we review spectral/temporal encoding techniques, in which the information about the image structure is encoded into the spectrum/temporal waveform. These methods rely on the Fourier transform relationships, linking the time/frequency domains to the space/k-space domains (Fig. 40).

5.3a. Spectral and Temporal Encoding

A classic implementation of the space-to-time image transformation in the infrared/visible range is the serial time-encoded amplified (STEAM) system [393,394]. In the STEAM system developed in Ref. [393], spatial dispersers were used to encode spatial information into a broadband spectrum. Then, using a dispersion compensating fiber and Raman amplification, the spectrum of an optical pulse was mapped in time domain. A single-pixel photodetector was then used to reconstruct the 2D image at a laser repetition rate of 6.1 MHz, allowing for the real-time video acquisition of fast dynamic phenomena.

Figure 39

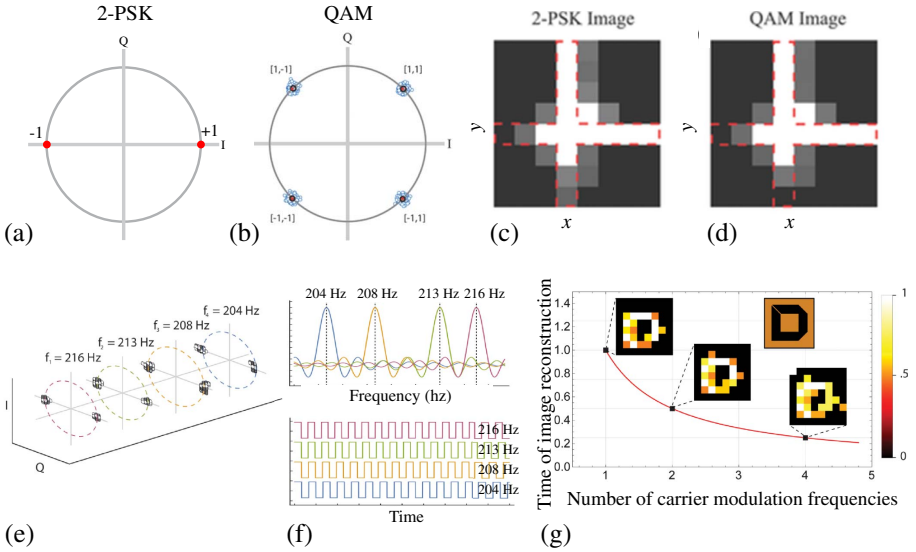

(a) Constellation diagram for the phase-shift key modulation with 2 states (2-PSK) and (b) 4 states (QAM). (c) Reconstruction of an inverted metallic cross using 2-PSK and (d) QAM. Adapted with permission from [390]. (e) Constellation diagram for frequency multiplexing. (f) The spectrum (top) and the square waveforms in the time domain (bottom) of the selected modulation frequencies. (g) Reduction of the time to reconstruct an image using an increasing number of carrier modulation frequencies and corresponding images. Adapted with permission from [362].

Similar to the spatial disperser used in the STEAM system [395], blazed diffraction gratings have been introduced in the THz range to map the spectrum in 1D space. In Ref. [396], Schuman *et al.* fabricated an aluminum blazed diffraction grating with a groove depth and period chosen to achieve an angular dispersion of 15 deg per 100 GHz. The authors selected the first diffractive order between 300 and 600 GHz since it achieved a high diffraction efficiency of 85%. The grating was then used in combination with an f-theta lens to ensure that the focal points of the individual frequencies were in the same plane, either in transmission [Fig. 41(a)] or in reflection geometry [Fig. 41(b)]. To calibrate the measurement, the THz detector was linearly scanned in the focal line, and a third-order polynomial was used to correlate the THz frequency with the spatial position [Fig. 41(c)]. Thus, by directly measuring the spectrum, a complete 1D line in the image can be acquired. In Fig. 41(d), metal letters attached to a sheet of paper were imaged in transmission and in reflection (inset) using blazed gratings. There, the horizontal axis has been acquired from the spectrum while the vertical axis was imaged by linearly scanning the object. It can be observed that the right side of the image exhibits better resolution than the left side, which can be directly attributed to the nonlinear frequency-to-space relationship measured in Fig. 41(c). A second grating perpendicular to the first one can be added to map the frequencies in 2D spatial coordinates [397,398]. In Ref. [399], the authors mapped a 60 cm × 60 cm area using 401 frequency points between 75 and 110 GHz.

In Ref. [400], Lee *et al.* demonstrated near-field imaging using spectral encoding with a metasurface. Gold cross-type mesh filters were fabricated via photolithography on a polyimide substrate [Fig. 42(a)]. These filters act as transmission bandpass filters in the frequency domain. By spatially patterning the meshes with varying geometrical dimensions, the authors designed a metasurface able to map the spatial positions in the THz spectrum. Then, they demonstrated two reconstruction techniques using either an angular scan of the object [Figs. 42(c)–42(e)] or a translation scan of a metallic slit [Figs. 42(f)–42(h)]. In the angular scan, the reconstruction was made with an inverse Radon transform, while in the translation scan, a collection of measurements represented the image directly in the spectrum. Using numerical simulations, they found that both reconstructions are sensitive to the Q factor of the mesh filter. For a uniform mesh distribution, the Q factor is defined as the ratio of the central wavelength to the bandwidth of the bandpass filter. Therefore, a larger Q factor characterizes a narrower bandpass filter. With the angular scan, due to the nature of the reconstruction, a lower Q factor caused a blur in the entire image. In the translation scan, the Q factor affected the y axis resolution, while the x resolution was determined by the width of the slit.

Figure 40

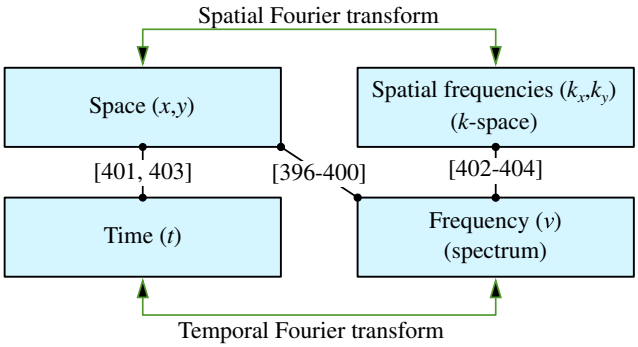

Schematic description of the spectral/temporal encoding. The references of Section 5.3 are indicated at the relative positions in the schematic.

An example of a space-to-time conversion imaging is demonstrated in Ref. [401]. With a THz-TDS system, Stübling *et al.* made a multipixel emitter unit by dividing a single THz pulse into multiple pulses using a set of polymer beam splitters [Fig. 43(a)]. On the detector side, specially designed mirrors were placed to redirect the individual pulses into a single-pixel THz photoconductive antenna. Then, a series of THz pulses appear in the time-domain measurement by scanning over a sufficiently large temporal window [Fig. 43(b)]. These pulses correspond to different spatial positions, as confirmed by the raster-scan above the emitter head [Fig. 43(c)]. Therefore, they can be used to reconstruct an image. As this configuration relies on scanning the optical delay line, the methods that we have described in Section 3.2 can be applied to reduce the acquisition time. Here, the authors used ASOPS in their system implementation.

5.3b. Fourier Optics and k-Space/Frequency Duality

By using Fourier optics relationships, the spatial frequencies can be encoded into the spectrum [402–404]. The concept here is to use a diffractive element to retrieve a linear relationship between the k-vector and the frequency. The simplest implementation uses a lens to do the encoding [Fig. 44(a)]. The Fourier optics theory states that a given field profile $S(x, y, \nu)$ at the front focal plane (object plane) of a convex lens is Fourier transformed at the back focal plane (Fourier plane) according to [166]

$$U(\xi, \eta, \nu) = \frac{\nu}{jcF} \iint \mathrm{d}x\mathrm{d}y S(x, y, \nu) \exp\left[-\frac{j2\pi\nu}{cF}(x\xi + y\eta)\right], \tag{38}$$

where F is the lens focal length, c is the speed of light, and ν is the frequency. The coordinates (x, y) and (ξ, η) are the spatial positions in the object plane and the Fourier plane, respectively. The original field distribution $S(x, y, \nu)$ can then be reconstructed by using the inverse Fourier transform:

Figure 41

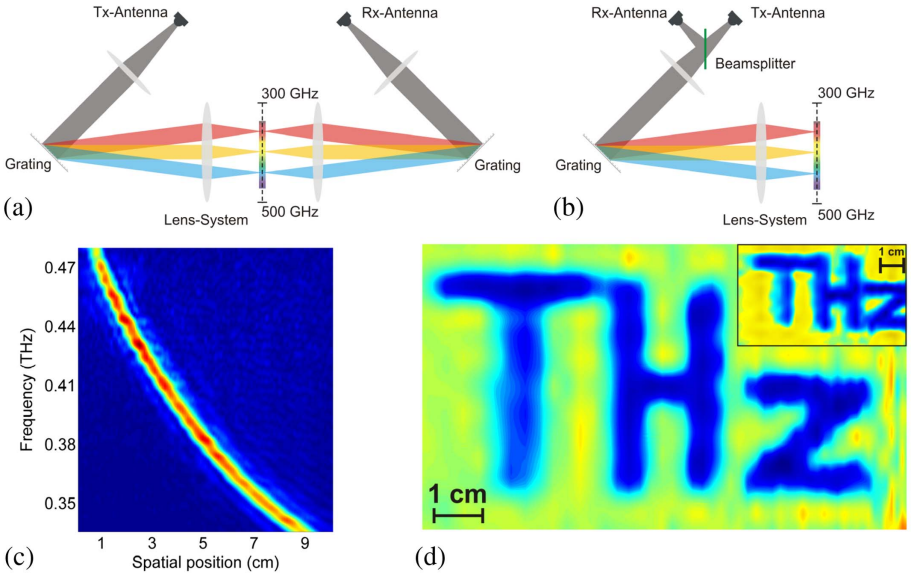

(a) Transmission and (b) reflection geometry with a blazed diffraction grating and an f-theta lens system. (c) Calibration measurement of the frequency as a function of the spatial position (d) Demonstration of THz imaging in transmission geometry. Inset: reflection geometry. Reprinted with permission from [396]. Copyright 2012 Optical Society of America.

$$S(x,y,\nu) = \frac{j\nu}{cF}\iint \mathrm{d}\xi\mathrm{d}\eta U(\xi,\eta,\nu)\exp\left[+\frac{j2\pi\nu}{cF}(x\xi+y\eta)\right]. \tag{39}$$

The spatial frequencies, also known as components of the k-space, are related to the (ξ,η) coordinates through

$$k_\xi = \frac{\xi\nu}{cF} \qquad k_\eta = \frac{\eta\nu}{cF}. \tag{40}$$

Since the spatial frequencies are proportional to the frequency ν, one can use the THz spectrum to scan along a line in the k-space. In other words, by fixing the detector in the Fourier plane at (ξ_0,η_0) and using a broadband source such as $\nu\in[\nu_{\min},\nu_{\max}]$, Eq. (40) can be combined to give

$$k_\eta = \frac{\eta_0}{\xi_0}k_\xi. \tag{41}$$

By changing the ratio η_0/ξ_0, the whole k-space can be sampled. The simplest way to change this ratio is to measure points along a circle of radius ρ_0 in the Fourier plane. Therefore, the 2D raster-scan [Fig. 44(b)] that provides a hyperspectral cube in the

Figure 42

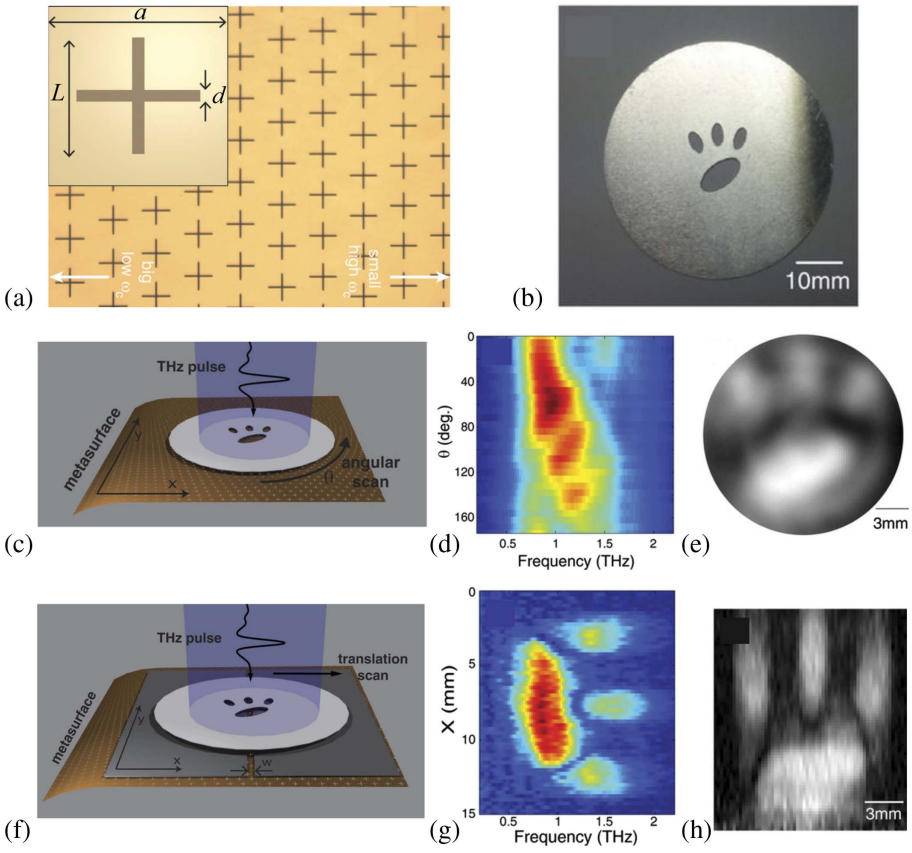

(a) Cross-type mesh-based metasurface with varying geometrical parameters. (b) Photograph of the sample. (c) Angular scan geometry, (d) THz spectrum as a function of the angle, and (e) reconstructed image with the radon transform. (f) Translational scan geometry, (g) THz spectrum as a function of the position of the slit, and (h) reconstructed image. Adapted from [400] under the terms of the Creative Commons Attribution 4.0 License. With copyright permission.

k-space [Fig. 44(c)] can be substituted by a 1D linear scan [Fig. 44(d)] along a circle, and the measured spectrum can be mapped into the radial dimension of the *k*-space [Fig. 44(e)].

This idea was demonstrated in the THz range by Lee *et al.* in Ref. [402]. In their implementation, they used a parabolic mirror as the diffractive element. An aperture of 5 mm diameter at 15 mm away from the optical axis was placed at the Fourier plane, while a second parabolic mirror focused the THz beam into a fixed single-pixel detector. Then, using a THz-TDS setup, they measured several spectra for different angular positions of the mask. They demonstrated reconstruction of a metallic object using 10–30 THz-TDS traces.

Figure 43

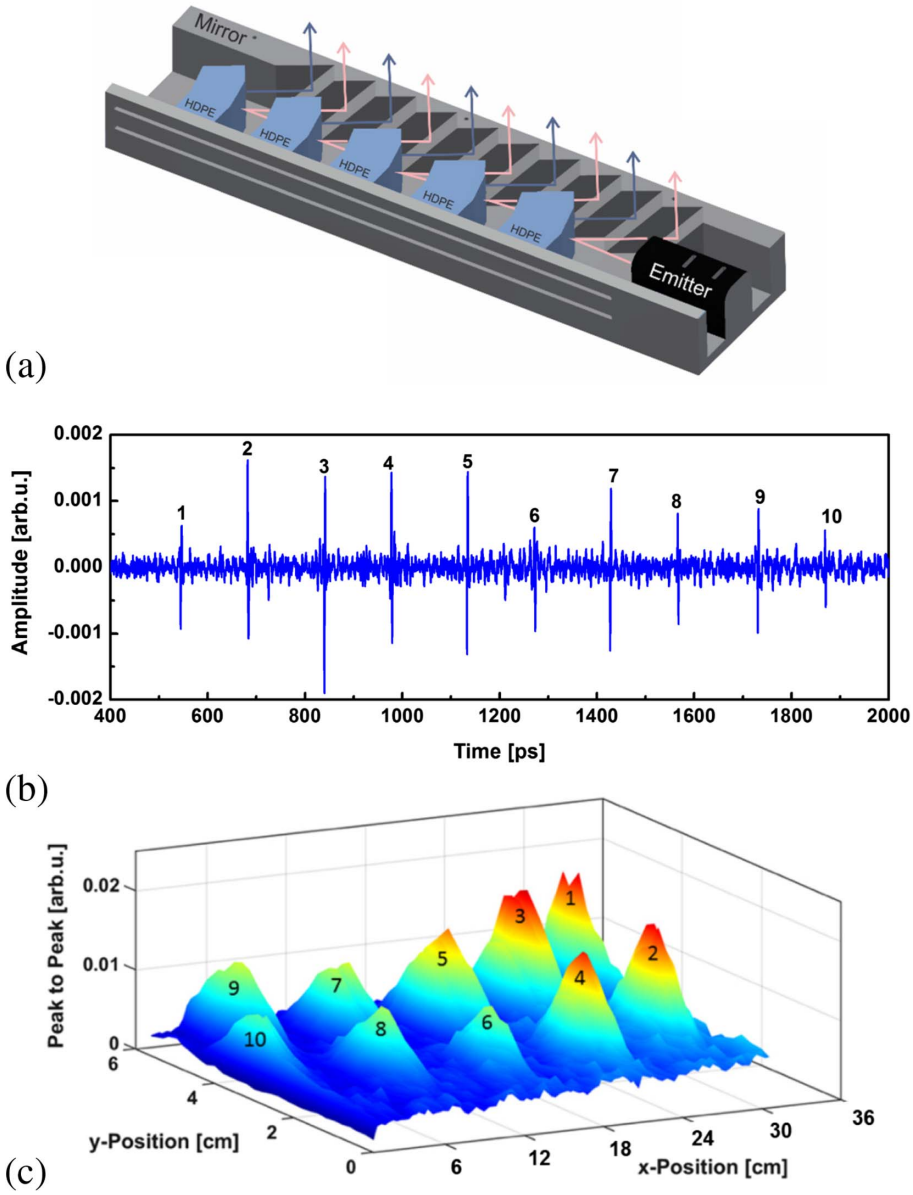

(a) The beam is divided into multiple spatial positions using beam splitters. (b) Time-domain measurement of the 10 pulses corresponding to the spatial positions in (d). Reprinted with permission from [401]. Copyright 2016 Optical Society of America.

In Ref. [403], the same group demonstrated similar spectral encoding using a slanted phase retarder made of Teflon at the position of the object. However, as in Ref. [402], mechanical rotation of the mask was necessary. Therefore, they also proposed to combine their approach with temporal encoding in k-space. For that purpose, they placed a mask in the Fourier plane that contained an angular pattern of holes, each containing additional phase retardation elements (Teflon disks of different thicknesses). The resultant long-time scan contained multiple THz pulses separated in time, each corresponding to a unique angular position in the k-space, which was then used to reconstruct the image.

In Ref. [404], Guerboukha *et al.* presented the rigorous mathematical theory behind the image reconstruction process reported in Refs. [402,403], as well as several novel imaging modes, which included amplitude- and phase-based modalities. They started by expressing the Fourier integral 39 in polar coordinates:

$$S(\vec{r},\nu) = \frac{j\nu}{cF}\iint \mathrm{d}\theta\rho\mathrm{d}\rho U(\vec{\rho},\nu)\exp\left[+\frac{j2\pi\nu}{cF}\vec{r}\cdot\vec{\rho}\right]. \tag{42}$$

In fact, the idea of spectral encoding implies that the integral over the radial coordinate $d\rho$ should somehow become an integral over the spectrum $d\nu$ in Eq. (42). Therefore, instead of the classic backward Fourier transform given Eq. (39), the authors rhoosed a new form of the reconstruction integral:

$$\tilde{S}(\vec{r}) = \iint \mathrm{d}\theta\nu\mathrm{d}\nu\left[\frac{j\rho_0^2}{cF\nu}\frac{U(\vec{\rho}_0,\nu)}{U_{\mathrm{ref}}(\nu)}\right]\exp\left[+\frac{j2\pi\nu}{cF}\vec{r}\cdot\vec{\rho}_0\right]. \tag{43}$$

Recognizing that the reconstruction $\tilde{S}(\vec{r})$ is different from the original object $S(\vec{r},\nu)$, the authors used in Eq. (43) a certain reference measurement $U_{\mathrm{ref}}(\nu)$ that allows attributing a physical meaning to the reconstruction $\tilde{S}(\vec{r})$. For example, in the case of

Figure 44

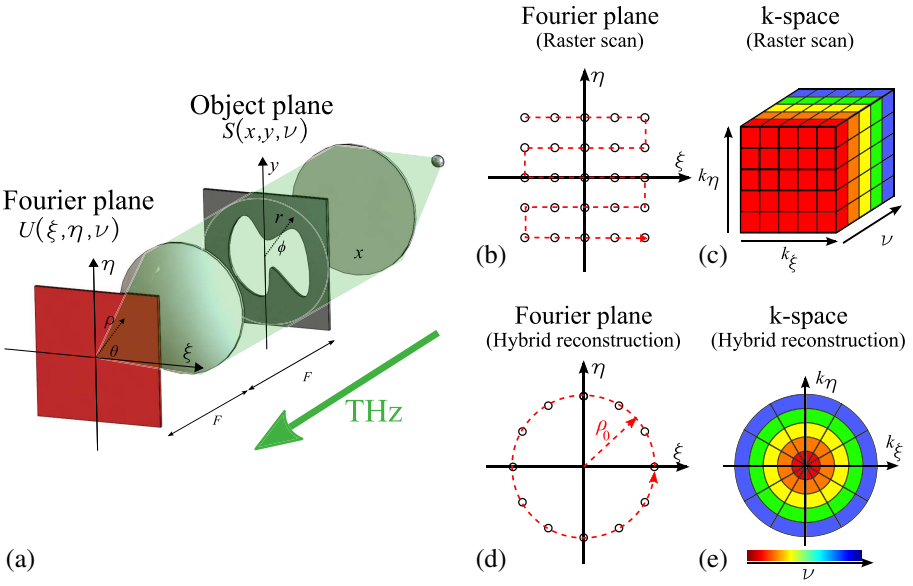

(a) General setup for k-space encoding using a lens. (b) Conventional raster-scan and (c) hyperspectral cube, and (d) circular scan and (e) k-space reconstruction using spectral encoding. Reprinted with permission from [404]. Copyright 2018 Optical Society of America.

amplitude imaging with binary metal masks (cut-outs in metal), the following reference was used:

$$U_{\text{ref}}(\nu) = \frac{jcF}{\nu} U(0,\nu), \tag{44}$$

where $U(0,\nu)$ is a measurement in the middle of the Fourier plane with the metal mask in place. Then, they mathematically showed that the reconstructed image according to the definition given by Eq. (43) is simply the original object normalized by the total area:

$$\tilde{S}(r,\phi) = \frac{S(r,\phi)}{\iint S(r,\phi)\mathrm{d}\phi r\mathrm{d}r}. \tag{45}$$

Figures 45(a)–45(f) present the experimental results when reconstructing a cut-out in the metal sheet in the form of a maple leaf (amplitude mask). The amplitude [Fig. 45(d)] and the phase [Fig. 45(e)] of the k-space reconstructed with the spectral encoding are comparable to those acquired with a raster scan [Figs. 45(a) and 45(b)]. However, the reconstructed object with the spectral encoding [Fig. 45(f)] required sampling of only 45 spatial positions, compared to the raster-scan with 4624 spatial positions [Fig. 45(c)].

Using the mathematical theory described above, the authors extended the idea to phase masks. As an example, they imaged a polymer plate (refractive index n_m) with a shallow 100 μm engraving. Interestingly, to enable imaging of phase masks, only the reference has to be modified in Eq. (43) as

$$U_{\text{ref}}(\nu) = jcFU(0,\nu), \tag{46}$$

where $U(0,\nu)$ is a measurement in the center of the Fourier plane using a polymer plate without the engraving. Then, the authors showed that the imaginary part of the reconstructed object using Eq. (43) is proportional to the optical path $\Delta(\vec{r}) = (n_m - 1)\, h(\vec{r})$ due to the engraving:

$$\mathrm{Im}\{\tilde{S}(\vec{r})\} = -\frac{2\pi}{c}\frac{S(\vec{r})}{\iint S(\vec{r})\mathrm{d}\vec{r}}\Delta(\vec{r}). \tag{47}$$

Therefore, by measuring a plate with [Fig. 45(g)] and without the engraving [Fig. 45(h)], they were able to directly map the height of the engraving [Fig. 45(i)].

Contrary to the spectral encoding techniques described in Section 5.3b, encoding an image into k-space requires no complex optical devices. Thus, a simple lens was used in Ref. [404] and the detector was simply positioned off-axis. In fact, instead of using a circular lens, one could use a cylindrical lens to perform 1D Fourier transform. Then, by simply scanning the object in the other dimension, every measured spectrum would provide a 1D line of the object. This type of configuration could be used in a conveyer belt system to obtain a 2D THz image.

The spatial resolution when using spectral encoding of the k-space can be directly derived from the Nyquist theorem that states that the minimal achievable resolution is $\delta x = 0.5/k_{\text{max}}$, where k_{max} is the maximal spatial frequency sampled in k-space. Therefore, the resolution of the image can be improved by measuring the larger k-space components located at the periphery of the limiting aperture (field of view) in the Fourier plane. When using spectral encoding of the k-space, Eq. (40) shows that $k_{\text{max}} = \nu_{\text{max}}\rho/cF$, with ν_{max} being the maximal THz frequency, ρ the radial position

of the detector (in the Fourier plane), and F the focal length. Therefore, the resolution becomes $\delta x = 0.5cF/\nu_{\max}\rho$ and can be increased by using a lens with a shorter focal lens, by positioning the detector at a larger radial position and by using spectrally broader THz source.

Finally, we would like to discuss the impact of the THz spectral encoding and Fourier optics on the broadband spectral information. One must recognize that fast reconstruction algorithms as presented above [see Eq. (43)] use spectral information to sample the k-space. Therefore, the reconstructed image is different from a hyperspectral image obtained, for example, using THz-TDS. Moreover, uneven power distribution in the pulse spectrum should be mitigated by acquisition of a reference spectrum of an empty system or a substrate (see, for example, the calibration step in Ref. [396] or the normalizations in Ref. [404]), which somewhat complicates the imaging procedure. Additionally, in the case of samples exhibiting significant frequency-dependent loss variations, image resolution might suffer due to effective loss of information at frequencies characterized by strong absorption. For example, for many dielectrics, one expects reduction of the maximal useful frequency value due to stronger sample absorption at higher frequencies. Inversely, if the sample has piecewise weakly dependent losses, then we expect excellent reconstruction results. For example, spectral encoding in Fourier space can be used together with a fast

Figure 45

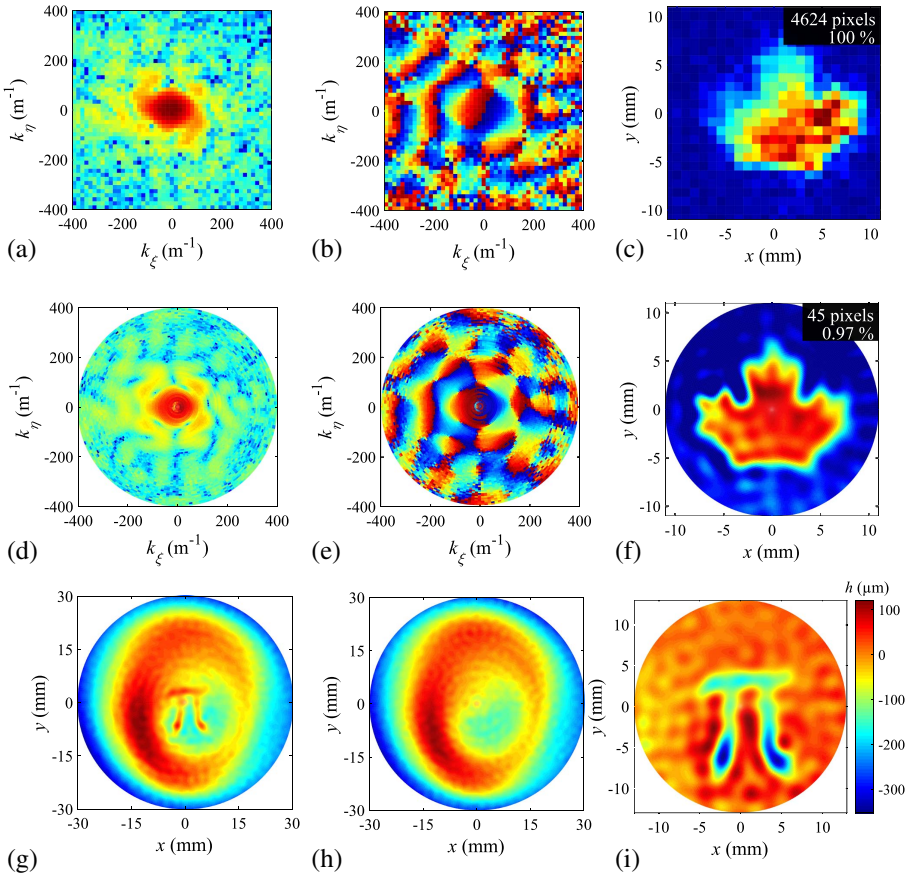

(a) General setup for k-space encoding using a lens. (b) Conventional raster-scan and (c) hyperspectral cube and (d) Circular scan and (e) k-space reconstruction using spectral encoding. Reprinted with permission from [404]. Copyright 2018 Optical Society of America.

Fourier transform algorithm to efficiently reconstruct amplitude variations at the edges between distinct materials. This case is already important for defense and mail screening applications.

5.4. Section Summary and Future Directions

In this section, we have reviewed three main techniques to enable THz imaging with single-pixel detectors: (1) mechanical beam steering, (2) single-pixel imaging and compressive sensing, and (3) spectral/temporal encoding and Fourier optics. Historically, these techniques have been developed to mitigate the high cost and difficulty of manufacturing multipixel THz cameras. Today, these techniques are mature enough to be an integral part of the cost-effective imaging systems. Furthermore, the single-pixel detectors used in such systems are often phase sensitive and can measure both amplitude and phase of the electric field with very high SNR. This is a key advantage when compared to THz cameras that commonly detect only the signal intensity. Therefore, even with the advent of THz cameras, we believe that development of the single-pixel imaging techniques will remain highly pertinent.

The first single-pixel imaging technique that we have reviewed is mechanical beam-steering. Historically, to obtain a THz image, the sample was positioned at the focal point of focusing optics and physically moved pixel by pixel. In many situations, sample displacement is not desirable or even possible. Instead of moving the sample, one can mechanically steer the THz beam over the sample. A combination of oscillating mirrors and an f-theta lens can provide a simple and cost-effective solution for short-range applications, for example, in industrial environments using conveyer belts. In comparison, the Gregorian reflector system is seen as a desirable candidate for large stand-off distances, for example, in the security and defense sector. Eventually, the future development of non-mechanical beam-steering technology would allow stable and rapid dynamic scans. This has already been explored using electrically controlled liquid crystal devices [327], optically pumped semiconductor wafers [328,330], special THz generation techniques [331–333], or distributed arrays of emitters [323,334]. In particular, in Ref. [323], Sengupta and Hajimiri fabricated a distributed array of active radiators in CMOS to generate a 0.28 THz beam. By tuning the relative phase of the 4×4 emitter array, the THz beam could be steered in two dimensions, over 80° in azimuth and elevation. Finally, we mention that the beam-steering technique is not strictly limited to single-pixel detectors. In fact, they could be used with THz cameras to increase the field of view.

In parallel, single-pixel imaging using compressive sensing has seen important development in the context of THz imaging. Within this method, the image is reconstructed by successive single-pixel measurements of a spatially modulated THz beam over the sample (aperture functions). Then, assuming that the object is naturally sparse, the compressive sensing theory can be used to reconstruct the image with a number of measurements smaller than the total number of pixels. As for real-time imaging, recent schemes involve the use of SLM. Spatial patterns can be optically encoded in a semiconductor wafer, which can also act as a substrate for near-field compressive sensing imaging. At the same time, electronic modulation allows for more complex pattern modulation. Notably, the simultaneous modulation of multiple masks can lead to major improvements in terms of acquisition rates. There, the different masks are encoded using sine waves of different phases and frequencies, to enable fast image acquisition through channel multiplexing and detection with a lock-in amplifier. Eventually, when the number of channels equals the total number of desired masks, the image can be acquired in a one-shot process. In practice, as in any communications system, the total number of channels is limited by the noise floor. Consequently, as the acquisition time decreases, so does the overall SNR. Finally, the developments in this

field are intimately related to the development of efficient SLM devices with near-unity modulation factor and low transmission/reflection losses, to reduce the overall integration time of the detector and enable even faster acquisition rates.

Finally, spectral encoding techniques take advantage of the relationships between time and space to encode the spatial information of a sample in the spectrum, the temporal waveform, or in the Fourier space. The idea here is to use a broadband pulse along with frequency-dependent diffraction devices to spread the frequencies over the sample. Then, the transmitted/reflected spectrum can be recorded using a single-pixel detector, for example, using a THz-TDS system. The diffraction device can be a diffraction grating, a specially designed metasurface, a series of polymer retarders, or just a common lens. If THz-TDS is used, one must be aware that the spatial dimensions are often traded for a 1D spectral dimension that is obtained by measuring the temporal waveform with an optical delay line. In this case, the spatial line acquisition rate is often determined by the speed of the optical delay line (see Section 3.2). In principle, as it is done in the visible range, one could also use THz cameras (Section 4) to directly measure the spectrum and therefore avoid the use of the optical delay line. In fact, in Section 3.4c, we saw demonstration of such a device, using temporal encoding, a camera, and EOS.

6. CONCLUSION

In conclusion, THz imaging uses the properties of THz waves to interrogate matter in unique ways. In the past 20 years, important technological developments have taken place to enable real-time high-resolution imaging. Today, research in THz imaging is steadily shifting from laboratory-based instrumentation to commercial products. In this context, we have reviewed THz imaging with an emphasis on the imaging modalities and tools that could enable high-resolution real-time imaging and its fundamental and industrial applications.

We started this review by detailing recent advances in some of the most promising THz imaging modalities. Particularly, in THz transmission and reflection spectroscopy, the complex refractive index of a material can be obtained using Fresnel coefficients, which leads to the determination of the complex permittivity and conductivity. In THz pulsed imaging, the temporal delay between several reflected THz pulses is used to image through layered structures. THz-CT exploits the ability of THz waves to penetrate matter to reconstruct a volumetric image of an object. In THz near-field imaging, apertures and scattering tips are used to enable subwavelength resolution, thus beating the diffraction limit.

We then focused our attention on three major research directions to enable real-time THz imaging: THz-TDS real-time imaging, THz cameras, and THz single-pixel imaging.

Many of the developed imaging techniques rely on THz-TDS systems that allow coherent measurement of the amplitude and phase of the pulsed THz electric field at the picosecond time scale. However, imaging with a THz-TDS system requires using relatively slow instrumentation that impedes real-time imaging. To speed up acquisition time of the THz signal, many modifications to the THz-TDS system subcomponents were proposed. Thus, to forgo the linear movement of the optical delay line, reflective or prism-based rotary delay lines have been developed. Alternatively, one can use asynchronous optical sampling, electronically controlled optical sampling, and optical sampling by cavity tuning, which are various techniques that can be used to avoid altogether the mechanical movement of a delay line. Additionally, we have mentioned that photoconductive antennas and EOS are currently the two key methods for coherent detection of THz pulses. While in their

simplest form both techniques offer single-pixel coherent detection, recently there was significant progress in realizing arrays of THz photoconductive antennas, as well as using infrared/visible cameras with EOS, thus greatly speeding up image acquisition times.

In parallel, intensive research has been conducted to develop THz cameras similar to those available in the visible region of the spectrum. Among their technical requirements for mass deployment, they should operate at room temperature, be compatible with standard fabrication technologies (such as CMOS process), have little weight, small size, and low power consumption, and offer high sensitivities (for high frame rate THz imaging even without an active THz source). Two major technological trends are being pursued to realize THz cameras that would respond to those criteria: THz thermal cameras and THz FET-based cameras. On one hand, THz thermal cameras measure the heat generated by the absorption of the THz radiation. Pyroelectric cameras and microbolometers have been used for THz imaging. In particular, microbolometers have achieved remarkable sensitivities at room temperature thanks to the inclusion of a Fabry–Perot cavity, coupling antennas, and metamaterial absorbers to increase the absorbed THz radiation. On the other hand, the THz FET-based cameras measure a rectified voltage after interaction of the THz radiation with a plasma wave in the transistor channel. Theoretical works predicted both frequency-specific (resonant) and broadband (non-resonant) detection mechanisms, which have been used to describe the behavior of THz-FET detectors of a variety of materials, ranging from III–V semiconductors to graphene layers. The silicon FET is an attractive candidate for THz cameras, since it is compatible with CMOS process technology, therefore enabling scaling into high-resolution arrays at reduced costs.

At the same time, we have emphasized that single-pixel detectors can be efficiently used for fast acquisition of THz images within the framework of fast mechanical steering and computational imaging. Mechanical beam-steering with oscillating mirrors and f-theta lenses allow rapid image acquisition using a conveyer belt arrangement, while a Gregorian reflector system can be used to construct an image at stand-off distances for security applications. Furthermore, in recent years, there were substantial developments in computational imaging, leading to a plethora of single-pixel imaging techniques that allow image reconstruction from a series of judicially designed single-pixel spectroscopic measurements. Thus, one can reconstruct an image by performing a series of single-pixel measurements with a series of aperture masks that partially conceal the image. By using the sparsity property of natural images, compressive sensing can reduce the number of measurements well below the limit imposed by the Nyquist theorem, resulting in reduced time acquisitions. By using SLM and advanced mask encoding methods, real-time THz single-pixel imaging is within reach, even in the near-field imaging context. Finally, taking advantage of the relationships between time and space, the spatial information about an object can be encoded in the spectrum or in the temporal waveform, using blazed diffraction gratings, specially designed metasurfaces of beam-splitting devices. Finally, by using the principles of Fourier optics with broadband pulses, the spatial frequency information about the imaged object can be efficiently reconstructed from the spectral data recorded in the k-space, thus leading to fast Fourier optics image modalities.

We would like to note that the three major research directions that we have reviewed in this work are not necessarily in direct competition with one another, nor are they mutually exclusive. In fact, they can profit from each other via development of hybrid systems. For example, intensity-sensitive THz cameras are important for various applications where object differentiation via simple absorption is prevalent. At the same time, phase-sensitive THz-TDS imaging is of great importance for material

characterization and finer measurements of local changes in material physical properties. At the same time, the hardware and computational techniques developed within the single-pixel imaging modality can be considerably enhanced or sped up by substituting single-pixel detectors with THz detector arrays.

To summarize, in this work, we presented a critical and comprehensive review of enabling hardware, instrumentation, algorithms, and potential applications in real-time high-resolution THz imaging. We believe that this review can serve a diverse community of fundamental and applied scientists as it covers extensively both practical aspects of imaging system designs, as well as fundamental physical and mathematical principles on which such designs are based. Finally, many practical applications of the imaging systems were presented, making this review of interest to a wider audience.

FUNDING

Canada Research Chairs I of Prof. Skorobogatiy in Ubiquitous THz photonics; Canada Foundation for Innovation (CFI); Natural Sciences and Engineering Research Council of Canada (NSERC); Fonds de Recherche du Québec—Nature et Technologies (FRQNT).

REFERENCES

1. S. S. Dhillon, M. S. Vitiello, E. H. Linfield, A. G. Davies, M. C. Hoffmann, J. Booske, C. Paoloni, M. Gensch, P. Weightman, G. P. Williams, E. Castro-Camus, D. R. S. Cumming, F. Simoens, I. Escorcia-Carranza, J. Grant, S. Lucyszyn, M. Kuwata-Gonokami, K. Konishi, M. Koch, C. A. Schmuttenmaer, T. L. Cocker, R. Huber, A. G. Markelz, Z. D. Taylor, V. P. Wallace, J. Axel Zeitler, J. Sibik, T. M. Korter, B. Ellison, S. Rea, P. Goldsmith, K. B. Cooper, R. Appleby, D. Pardo, P. G. Huggard, V. Krozer, H. Shams, M. Fice, C. Renaud, A. Seeds, A. Stöhr, M. Naftaly, N. Ridler, R. Clarke, J. E. Cunningham, and M. B. Johnston, "The 2017 terahertz science and technology roadmap," J. Phys. D **50**, 043001 (2017).
2. D. M. Mittleman, "Perspective: terahertz science and technology," J. Appl. Phys. **122**, 230901 (2017).
3. J. Federici and L. Moeller, "Review of terahertz and subterahertz wireless communications," J. Appl. Phys. **107**, 111101 (2010).
4. T. Kleine-Ostmann and T. Nagatsuma, "A review on terahertz communications research," J. Infrared Millim. Terahertz Waves **32**, 143–171 (2011).
5. H. J. Song and T. Nagatsuma, "Present and future of terahertz communications," IEEE Trans. Terahertz Sci. Technol. **1**, 256–263 (2011).
6. I. F. Akyildiz, J. M. Jornet, and C. Han, "Terahertz band: next frontier for wireless communications," Phys. Commun. **12**, 16–32 (2014).
7. T. Nagatsuma, G. Ducournau, and C. C. Renaud, "Advances in terahertz communications accelerated by photonics," Nat. Photonics **10**, 371–379 (2016).
8. D. M. Mittleman, "Twenty years of terahertz imaging," Opt. Express **26**, 9417–9431 (2018).
9. A. Redo-Sanchez, N. Laman, B. Schulkin, and T. Tongue, "Review of terahertz technology readiness assessment and applications," J. Infrared Millim. Terahertz Waves **34**, 500–518 (2013).
10. M. Yin, S. Tang, and M. Tong, "The application of terahertz spectroscopy to liquid petrochemicals detection: a review," Appl. Spectrosc. Rev. **51**, 379–396 (2016).
11. M. Haaser, Y. Karrout, C. Velghe, Y. Cuppok, K. C. Gordon, M. Pepper, J. Siepmann, T. Rades, P. F. Taday, and C. J. Strachan, "Application of terahertz

pulsed imaging to analyse film coating characteristics of sustained-release coated pellets," Int. J. Pharm. **457**, 521–526 (2013).
12. J. Sibik and J. A. Zeitler, "Direct measurement of molecular mobility and crystallisation of amorphous pharmaceuticals using terahertz spectroscopy," Adv. Drug Deliv. Rev. **100**, 147–157 (2016).
13. R. J. Falconer and A. G. Markelz, "Terahertz spectroscopic analysis of peptides and proteins," J. Infrared Millim. Terahertz Waves **33**, 973–988 (2012).
14. S. Fan, Y. He, B. S. Ung, and E. Pickwell-MacPherson, "The growth of biomedical terahertz research," J. Phys. D **47**, 374009 (2014).
15. L. Xie, Y. Yao, and Y. Ying, "The application of terahertz spectroscopy to protein detection: a review," Appl. Spectrosc. Rev. **49**, 448–461 (2014).
16. T. Bowman, M. El-Shenawee, and L. Campbell, "Terahertz imaging of excised breast tumor tissue on paraffin sections," IEEE Trans. Antennas Propag. **63**, 2088–2097 (2015).
17. M. Kawase, "Application of terahertz waves to food science," Food Sci. Technol. Res. **18**, 601–609 (2012).
18. J. Qin, Y. Ying, and L. Xie, "The detection of agricultural products and food using terahertz spectroscopy: a review," Appl. Spectrosc. Rev. **48**, 439–457 (2013).
19. K. Wang, D. W. Sun, and H. Pu, "Emerging non-destructive terahertz spectroscopic imaging technique: principle and applications in the agri-food industry," Trends Food Sci. Technol. **67**, 93–105 (2017).
20. H.-B. Liu, H. Zhong, N. Karpowicz, Y. Chen, and X.-C. Zhang, "Terahertz spectroscopy and imaging for defense and security applications," Proc. IEEE **95**, 1514–1527 (2007).
21. S. R. Murrill, E. L. Jacobs, S. K. Moyer, C. E. Halford, S. T. Griffin, F. C. De Lucia, D. T. Petkie, C. C. Franck, F. C. De Lucia, D. T. Petkie, and C. C. Franck, "Terahertz imaging system performance model for concealed-weapon identification," Appl. Opt. **47**, 1286–1297 (2008).
22. J. B. Jackson, J. Bowen, G. Walker, J. Labaune, G. Mourou, M. Menu, and K. Fukunaga, "A survey of terahertz applications in cultural heritage conservation science," IEEE Trans. Terahertz Sci. Technol. **1**, 220–231 (2011).
23. A. Cosentino, "Terahertz and cultural heritage science: examination of art and archaeology," Technologies **4**, 1–13 (2016).
24. A. Maestrini, B. Thomas, H. Wang, C. Jung, J. Treuttel, Y. Jin, G. Chattopadhyay, I. Mehdi, and G. Beaudin, "Schottky diode-based terahertz frequency multipliers and mixers," C. R. Phys. **11**, 480–495 (2010).
25. A. Dobroiu, M. Yamashita, Y. N. Ohshima, Y. Morita, C. Otani, and K. Kawase, "Terahertz imaging system based on a backward-wave oscillator," Appl. Opt. **43**, 5637–5646 (2004).
26. M. Mineo and C. Paoloni, "Corrugated rectangular waveguide tunable backward wave oscillator for terahertz applications," IEEE Trans. Electron Devices **57**, 1481–1484 (2010).
27. W. He, L. Zhang, D. Bowes, H. Yin, K. Ronald, A. D. R. Phelps, and A. W. Cross, "Generation of broadband terahertz radiation using a backward wave oscillator and pseudospark-sourced electron beam," Appl. Phys. Lett. **107**, 133501 (2015).
28. S. Kumar, "Recent progress in terahertz quantum cascade lasers," IEEE J. Sel. Top. Quantum Electron. **17**, 38–47 (2011).
29. A. Valavanis, J. Zhu, J. Freeman, L. Li, L. Chen, A. G. Davies, E. H. Linfield, and P. Dean, "Terahertz quantum cascade lasers with >1 W output powers," Electron. Lett. **50**, 309–311 (2014).

30. M. A. Belkin and F. Capasso, "New frontiers in quantum cascade lasers: high performance room temperature terahertz sources," Phys. Scr. **90**, 118002 (2015).
31. X. Wang, C. Shen, T. Jiang, Z. Zhan, Q. Deng, W. Li, W. Wu, N. Yang, W. Chu, and S. Duan, "High-power terahertz quantum cascade lasers with ~0.23 W in continuous wave mode," AIP Adv. **6**, 075210 (2016).
32. K. A. McIntosh, E. R. Brown, K. B. Nichols, O. B. McMahon, W. F. Dinatale, and T. M. Lyszczarz, "Terahertz photomixing with diode lasers in low-temperature-grown GaAs," Appl. Phys. Lett. **67**, 3844–3846 (1995).
33. S. Preu, G. H. Dhler, S. Malzer, L. J. Wang, and A. C. Gossard, "Tunable, continuous-wave terahertz photomixer sources and applications," J. Appl. Phys. **109**, 061301 (2011).
34. T. Ishibashi, Y. Muramoto, T. Yoshimatsu, and H. Ito, "Unitraveling-carrier photodiodes for terahertz applications," IEEE J. Sel. Top. Quantum Electron. **20**, 79–88 (2014).
35. Y. J. Ding, "Progress in terahertz sources based on difference-frequency generation," J. Opt. Soc. Am. B **31**, 2696–2711 (2014).
36. K. Kawase, M. Sato, T. Taniuchi, and H. Ito, "Coherent tunable THz-wave generation from $LiNbO_3$ with monolithic grating coupler," Appl. Phys. Lett. **68**, 2483–2485 (1996).
37. K. Kawase, H. Minamide, K. Imai, J. I. Shikata, and H. Ito, "Injection-seeded terahertz-wave parametric generator with wide tunability," Appl. Phys. Lett. **80**, 195–197 (2002).
38. S. Hayashi and K. Kawase, "Terahertz wave parametric sources," in *Recent Optical and Photonic Technologies* (2010), Vol. **1**, pp. 109–124.
39. H. Minamide, S. Hayashi, K. Nawata, T. Taira, J. I. Shikata, and K. Kawase, "Kilowatt-peak terahertz-wave generation and sub-femtojoule terahertz-wave pulse detection based on nonlinear optical wavelength-conversion at room temperature," J. Infrared Millim. Terahertz Waves **35**, 25–37 (2014).
40. D. H. Auston, K. P. Cheung, and P. R. Smith, "Picosecond photoconducting Hertzian dipoles," Appl. Phys. Lett. **45**, 284–286 (1984).
41. P. R. Smith, D. H. Auston, and M. C. Nuss, "Subpicosecond photoconducting dipole antennas," IEEE J. Quantum Electron. **24**, 255–260 (1988).
42. C. Fattinger and D. Grischkowsky, "Terahertz beams," Appl. Phys. Lett. **54**, 490–492 (1989).
43. X. C. Zhang and D. H. Auston, "Optoelectronic measurement of semiconductor surfaces and interfaces with femtosecond optics," J. Appl. Phys. **71**, 326–338 (1992).
44. X.-C. Zhang and D. H. Auston, "Optically induced THz electromagnetic radiation from planar photoconducting structures," J. Electromagn. Waves Appl. **6**, 85–106 (1992).
45. P. U. Jepsen, R. H. Jacobsen, and S. R. Keiding, "Generation and detection of terahertz pulses from biased semiconductor antennas," J. Opt. Soc. Am. B **13**, 2424–2436 (1996).
46. Y. C. Shen, P. C. Upadhya, E. H. Linfield, H. E. Beere, and A. G. Davies, "Ultrabroadband terahertz radiation from low-temperature-grown GaAs photoconductive emitters," Appl. Phys. Lett. **83**, 3117–3119 (2003).
47. A. Rice, Y. Jin, X. F. Ma, X. Zhang, D. Bliss, J. Larkin, and M. Alexander, "Terahertz optical rectification from ⟨110⟩ zinc-blende crystals," Appl. Phys. Lett. **64**, 1324–1326 (1994).
48. A. Schneider, M. Neis, M. Stillhart, B. Ruiz, R. U. A. Khan, and P. Günter, "Generation of terahertz pulses through optical rectification in organic DAST crystals: theory and experiment," J. Opt. Soc. Am. B **23**, 1822–1835 (2006).

49. K. L. Yeh, M. C. Hoffmann, J. Hebling, and K. A. Nelson, "Generation of 10 μJ ultrashort terahertz pulses by optical rectification," Appl. Phys. Lett. **90**, 171121 (2007).
50. C. P. Hauri, C. Ruchert, C. Vicario, and F. Ardana, "Strong-field single-cycle THz pulses generated in an organic crystal," Appl. Phys. Lett. **99**, 161116 (2011).
51. C. Vicario, M. Jazbinsek, A. V. Ovchinnikov, O. V. Chefonov, S. I. Ashitkov, M. B. Agranat, and C. P. Hauri, "High efficiency THz generation in DSTMS, DAST and OH1 pumped by Cr:forsterite laser," Opt. Express **23**, 4573–4580 (2015).
52. N. Oda, "Uncooled bolometer-type terahertz focal plane array and camera for real-time imaging," Comptes Rendus Phys. **11**, 496–509 (2010).
53. D. Dufour, L. Marchese, M. Terroux, H. Oulachgar, F. Généreux, M. Doucet, L. Mercier, B. Tremblay, C. Alain, P. Beaupré, N. Blanchard, M. Bolduc, C. Chevalier, D. D'Amato, Y. Desroches, F. Duchesne, L. Gagnon, S. Ilias, H. Jerominek, F. Lagacé, J. Lambert, F. Lamontagne, L. Le Noc, A. Martel, O. Pancrati, J. E. Paultre, T. Pope, F. Provençal, P. Topart, C. Vachon, S. Verreault, and A. Bergeron, "Review of terahertz technology development at INO," J. Infrared Millim. Terahertz Waves **36**, 922–946 (2015).
54. F. Simoens, J. Meilhan, and J.-A. Nicolas, "Terahertz real-time imaging uncooled arrays based on antenna-coupled bolometers or FET developed at CEA-Leti," J. Infrared Millim. Terahertz Waves **36**, 961–985 (2015).
55. Q. Li, S.-H. Ding, R. Yao, and Q. Wang, "Real-time terahertz scanning imaging by use of a pyroelectric array camera and image denoising," J. Opt. Soc. Am. A **27**, 2381–2386 (2010).
56. S.-H. Ding, Q. Li, Y.-D. Li, and Q. Wang, "Continuous-wave terahertz digital holography by use of a pyroelectric array camera," Opt. Lett. **36**, 1993–1995 (2011).
57. E. Hack, L. Valzania, G. Gäumann, M. Shalaby, C. P. Hauri, and P. Zolliker, "Comparison of thermal detector arrays for off-axis THz holography and real-time THz imaging," Sensors **16**, 1–11 (2016).
58. M. J. E. Golay, "The theoretical and practical sensitivity of the pneumatic infra-red detector," Rev. Sci. Instrum. **20**, 816–820 (1949).
59. R. Han, Y. Zhang, Y. Kim, D. Y. Kim, H. Shichijo, E. Afshari, and K. K. O, "Active terahertz imaging using Schottky diodes in CMOS: array and 860-GHz pixel," IEEE J. Solid-State Circuits **48**, 2296–2308 (2013).
60. S.-P. Han, H. Ko, N. Kim, W.-H. Lee, K. Moon, I.-M. Lee, E. S. Lee, D. H. Lee, W. Lee, S.-T. Han, S.-W. Choi, and K. H. Park, "Real-time continuous-wave terahertz line scanner based on a compact 1×240 InGaAs Schottky barrier diode array detector," Opt. Express **22**, 28977–28983 (2014).
61. R. Tauk, F. Teppe, S. Boubanga, D. Coquillat, W. Knap, Y. M. Meziani, C. Gallon, F. Boeuf, T. Skotnicki, C. Fenouillet-Beranger, D. K. Maude, S. Rumyantsev, and M. S. Shur, "Plasma wave detection of terahertz radiation by silicon field effects transistors: responsivity and noise equivalent power," Appl. Phys. Lett. **89**, 253511 (2006).
62. W. Knap, M. Dyakonov, D. Coquillat, F. Teppe, N. Dyakonova, J. Łusakowski, K. Karpierz, M. Sakowicz, G. Valusis, D. Seliuta, I. Kasalynas, A. Fatimy, Y. M. Meziani, and T. Otsuji, "Field effect transistors for terahertz detection: physics and first imaging applications," J. Infrared Millim. Terahertz Waves **30**, 1319–1337 (2009).
63. R. Al Hadi, H. Sherry, J. Grzyb, Y. Zhao, W. Forster, H. M. Keller, A. Cathelin, and A. Kaiser, and U. R. Pfeiffer, "A 1 k-pixel video camera for 0.7-1.1 terahertz imaging applications in 65-nm CMOS," IEEE J. Solid-State Circuits **47**, 2999–3012 (2012).

64. Q. Wu and X. C. Zhang, "Free-space electro-optic sampling of terahertz beams," Appl. Phys. Lett. **67**, 3523–3525 (1995).
65. P. U. Jepsen, C. Winnewisser, M. Schall, and V. Schyja, "Detection of THz pulses by phase retardation in lithium tantalate," Phys. Rev. E **53**, R3052–R3054 (1996).
66. A. Nahata, D. H. Auston, T. F. Heinz, and C. Wu, "Coherent detection of freely propagating terahertz radiation by electro-optic sampling," Appl. Phys. Lett. **68**, 150–152 (1996).
67. Q. Wu, T. D. Hewitt, and X.-C. Zhang, "Two-dimensional electro-optic imaging of THz beams," Appl. Phys. Lett. **69**, 1026–1028 (1996).
68. Z. G. Lu, P. Campbell, and X.-C. Zhang, "Free-space electro-optic sampling with a high-repetition-rate regenerative amplified laser," Appl. Phys. Lett. **71**, 593–595 (1997).
69. J. Dai, X. Xie, and X. C. Zhang, "Detection of broadband terahertz waves with a laser-induced plasma in gases," Phys. Rev. Lett. **97**, 8–11 (2006).
70. J. Dai, J. Liu, and X. C. Zhang, "Terahertz wave air photonics: terahertz wave generation and detection with laser-induced gas plasma," IEEE J. Sel. Top. Quantum Electron. **17**, 183–190 (2011).
71. F. Sizov and A. Rogalski, "THz detectors," Prog. Quantum Electron. **34**, 278–347 (2010).
72. M. Hangyo, "Development and future prospects of terahertz technology," Jpn. J. Appl. Phys. **54**, 120101 (2015).
73. T. Otsuji, "Trends in the research of modern terahertz detectors: plasmon detectors," IEEE Trans. Terahertz Sci. Technol. **5**, 1110–1120 (2015).
74. B. B. Hu and M. C. Nuss, "Imaging with terahertz waves," Opt. Lett. **20**, 1716–1718 (1995).
75. T. Löffler, K. Siebert, S. Czasch, T. Bauer, and H. G. Roskos, "Visualization and classification in biomedical terahertz pulsed imaging," Phys. Med. Biol. **47**, 3847–3852 (2002).
76. A. J. Fitzgerald, "Classification of terahertz-pulsed imaging data from excised breast tissue," J. Biomed. Opt. **17**, 016005 (2012).
77. J. P. Guillet, B. Recur, L. Frederique, B. Bousquet, L. Canioni, I. Manek-Hönninger, P. Desbarats, and P. Mounaix, "Review of terahertz tomography techniques," J. Infrared Millim. Terahertz Waves **35**, 382–411 (2014).
78. A. Ushakov, P. Chizhov, V. Bukin, A. Savel'ev, and S. Garnov, "Broadband in-line terahertz 2D imaging: comparative study with time-of-flight, cross-correlation, and Fourier transform data processing," J. Opt. Soc. Am. B **35**, 1159–1164 (2018).
79. L. Zhang, Y. Zhang, C. Zhang, Y. Zhao, and X. Liu, "Terahertz multiwavelength phase imaging without 2π ambiguity," Opt. Lett. **31**, 3668–3670 (2006).
80. P. A. Chizhov, A. A. Ushakov, V. V. Bukin, and S. V. Garnov, "Measurement of spatio-temporal field distribution of THz pulses in electro-optic crystal by interferometry method," Quantum Electron. **45**, 434–436 (2015).
81. R. W. McGowan, R. A. Cheville, and D. Grischkowsky, "Direct observation of the Gouy phase shift in THz impulse ranging," Appl. Phys. Lett. **76**, 670–672 (2000).
82. P. Kužel, H. Němec, F. Kadlec, C. Kadlec, P. Kuzel, H. Nemec, F. Kadlec, and C. Kadlec, "Gouy shift correction for highly accurate refractive index retrieval in time-domain terahertz spectroscopy," Opt. Express **18**, 15338–15348 (2010).
83. L. Duvillaret, F. Garet, and J.-L. Coutaz, "A reliable method for extraction of material parameters in terahertz time-domain spectroscopy," IEEE J. Sel. Top. Quantum Electron. **2**, 739–746 (1996).

84. J. F. O'Hara, W. Withayachumnankul, and I. Al-Naib, "A review on thin-film sensing with terahertz waves," J. Infrared Millim. Terahertz Waves **33**, 245–291 (2012).
85. T. D. Dorney, R. G. Baraniuk, and D. M. Mittleman, "Material parameter estimation with terahertz time-domain spectroscopy," J. Opt. Soc. Am. A **18**, 1562–1571 (2001).
86. M. Hangyo, T. Nagashima, and S. Nashima, "Spectroscopy by pulsed terahertz radiation," Meas. Sci. Technol. **13**, 1727–1738 (2002).
87. P. H. Bolivar, M. Brucherseifer, J. G. Rivas, R. Gonzalo, I. Ederra, A. Reynolds, M. Holker, and P. de Maagt, "Measurement of the dielectric constant and loss tangent of high dielectric constant materials at terahertz frequencies," IEEE Trans. Microw. Theory Tech. **51**, 1062–1066 (2003).
88. W. Withayachumnankul, B. Ferguson, T. Rainsford, S. P. Mickan, and D. Abbott, "Simple material parameter estimation via terahertz time-domain spectroscopy," Electron. Lett. **41**, 800–801 (2005).
89. I. Pupeza, R. Wilk, and M. Koch, "Highly accurate optical material parameter determination with THz time-domain spectroscopy," Opt. Express **15**, 4335–4350 (2007).
90. M. Naftaly and R. E. Miles, "Terahertz time-domain spectroscopy for material characterization," Proc. IEEE **95**, 1658–1665 (2007).
91. S. P. Mickan and X.-C. Zhang, "T-ray sensing and imaging," Int. J. High Speed Electron. Syst. **13**, 601–676 (2003).
92. S. Atakaramians, V. S. Afshar, T. M. Monro, and D. Abbott, "Terahertz dielectric waveguides," Adv. Opt. Photon. **5**, 169–215 (2013).
93. A. Markov, H. Guerboukha, and M. Skorobogatiy, "Hybrid metal wire-dielectric terahertz waveguides: challenges and opportunities," J. Opt. Soc. Am. B **31**, 2587–2600 (2014).
94. H. Guerboukha, G. Yan, O. Skorobogata, and M. Skorobogatiy, "Silk foam terahertz waveguides," Adv. Opt. Mater. **2**, 1181–1192 (2014).
95. T. Ma, A. Markov, L. Wang, and M. Skorobogatiy, "Graded index porous optical fibers —dispersion management in terahertz range," Opt. Express **23**, 7856–7869 (2015).
96. J. Li, K. Nallappan, H. Guerboukha, and M. Skorobogatiy, "3D printed hollow core terahertz Bragg waveguides with defect layers for surface sensing applications," Opt. Express **25**, 4126–4144 (2017).
97. P. U. Jepsen, U. Møller, and H. Merbold, "Investigation of aqueous alcohol and sugar solutions with reflection terahertz time-domain spectroscopy," Opt. Express **15**, 14717–14737 (2007).
98. L. Thrane, R. H. Jacobsen, P. U. Jepsen, and S. R. Keiding, "THz reflection spectroscopy of liquid water," Chem. Phys. Lett. **240**, 330–333 (1995).
99. U. Møller, D. G. Cooke, K. Tanaka, and P. U. Jepsen, "Terahertz reflection spectroscopy of Debye relaxation in polar liquids," J. Opt. Soc. Am. B **26**, A113–A125 (2009).
100. P. U. Jepsen and B. M. Fischer, "Dynamic range in terahertz time-domain transmission and reflection spectroscopy," Opt. Lett. **30**, 29–31 (2005).
101. P. U. Jepsen, J. K. Jensen, and U. Møller, "Characterization of aqueous alcohol solutions in bottles with THz reflection spectroscopy," Opt. Express **16**, 9318–9331 (2008).
102. M. Naftaly and R. Dudley, "Methodologies for determining the dynamic ranges and signal-to-noise ratios of terahertz time-domain spectrometers," Opt. Lett. **34**, 1213–1215 (2009).
103. R. M. Woodward, B. E. Cole, V. P. Wallace, R. J. Pye, D. D. Arnone, E. H. Linfield, and M. Pepper, "Terahertz pulse imaging in reflection geometry of human skin cancer and skin tissue," Phys. Med. Biol. **47**, 3853–3863 (2002).

104. F. A. Hegmann, O. Ostroverkhova, and D. G. Cooke, "Probing organic semiconductors with terahertz pulses," in *Photophysics of Molecular Materials* (Wiley, 2006), pp. 367–428.
105. J. Lloyd-Hughes and T. I. Jeon, "A review of the terahertz conductivity of bulk and nano-materials," J. Infrared Millim. Terahertz Waves **33**, 871–925 (2012).
106. M. C. Nuss, D. H. Auston, and F. Capasso, "Direct subpicosecond measurement of carrier mobility of photoexcited electrons in gallium arsenide," Phys. Rev. Lett. **58**, 2355–2358 (1987).
107. M. C. Beard, G. M. Turner, and C. A. Schmuttenmaer, "Transient photoconductivity in GaAs as measured by time-resolved terahertz spectroscopy," Phys. Rev. B **62**, 15764–15777 (2000).
108. R. Ulbricht, E. Hendry, J. Shan, T. F. Heinz, and M. Bonn, "Carrier dynamics in semiconductors studied with time-resolved terahertz spectroscopy," Rev. Mod. Phys. **83**, 543–586 (2011).
109. K. S. Novoselov, "Electric field effect in atomically thin carbon films," Science **306**, 666–669 (2004).
110. A. K. Geim and K. S. Novoselov, "The rise of graphene," Nat. Mater. **6**, 183–191 (2007).
111. A. C. Ferrari, F. Bonaccorso, V. Fal'ko, K. S. Novoselov, S. Roche, P. Bøggild, S. Borini, F. H. L. Koppens, V. Palermo, N. Pugno, J. A. Garrido, R. Sordan, A. Bianco, L. Ballerini, M. Prato, E. Lidorikis, J. Kivioja, C. Marinelli, T. Ryhänen, A. Morpurgo, J. N. Coleman, V. Nicolosi, L. Colombo, A. Fert, M. Garcia-Hernandez, A. Bachtold, G. F. Schneider, F. Guinea, C. Dekker, M. Barbone, Z. Sun, C. Galiotis, A. N. Grigorenko, G. Konstantatos, A. Kis, M. Katsnelson, L. Vandersypen, A. Loiseau, V. Morandi, D. Neumaier, E. Treossi, V. Pellegrini, M. Polini, A. Tredicucci, G. M. Williams, B. H. Hong, J.-H. Ahn, J. Min Kim, H. Zirath, B. J. van Wees, H. van der Zant, L. Occhipinti, A. Di Matteo, I. A. Kinloch, T. Seyller, E. Quesnel, X. Feng, K. Teo, N. Rupesinghe, P. Hakonen, S. R. T. Neil, Q. Tannock, T. Löfwander, and J. Kinaret, "Science and technology roadmap for graphene, related two-dimensional crystals, and hybrid systems," Nanoscale **7**, 4598–4810 (2015).
112. P. Bøggild, D. M. A. Mackenzie, P. R. Whelan, D. H. Petersen, J. D. Buron, A. Zurutuza, J. Gallop, L. Hao, and P. U. Jepsen, "Mapping the electrical properties of large-area graphene," 2D Mater. **4**, 042003 (2017).
113. P. A. George, J. Strait, J. Dawlaty, S. Shivaraman, M. Chandrashekhar, F. Rana, and M. G. Spencer, "Ultrafast optical-pump terahertz-probe spectroscopy of the carrier relaxation and recombination dynamics in epitaxial graphene," Nano Lett. **8**, 4248–4251 (2008).
114. J. L. Tomaino, A. D. Jameson, J. W. Kevek, M. J. Paul, A. M. van der Zande, R. A. Barton, P. L. McEuen, E. D. Minot, and Y.-S. Lee, "Terahertz imaging and spectroscopy of large-area single-layer graphene," Opt. Express **19**, 141–146 (2011).
115. J. L. Tomaino, A. D. Jameson, M. J. Paul, J. W. Kevek, A. M. Van Der Zande, R. A. Barton, H. Choi, P. L. McEuen, E. D. Minot, and Y. S. Lee, "High-contrast imaging of graphene via time-domain terahertz spectroscopy," J. Infrared Millim. Terahertz Waves **33**, 839–845 (2012).
116. M. J. Paul, J. L. Tomaino, J. W. Kevek, T. Deborde, Z. J. Thompson, E. D. Minot, and Y. S. Lee, "Terahertz imaging of inhomogeneous electrodynamics in single-layer graphene embedded in dielectrics," Appl. Phys. Lett. **101**, 091109 (2012).
117. J. D. Buron, D. H. Petersen, P. Bøggild, D. G. Cooke, M. Hilke, J. Sun, E. Whiteway, P. F. Nielsen, O. Hansen, A. Yurgens, and P. U. Jepsen, "Graphene conductance uniformity mapping," Nano Lett. **12**, 5074–5081 (2012).

118. J. D. Buron, F. Pizzocchero, P. U. Jepsen, D. H. Petersen, J. M. Caridad, B. S. Jessen, T. J. Booth, and P. Bøggild, "Graphene mobility mapping," Sci. Rep. **5**, 12305 (2015).
119. J. D. Buron, D. M. A. Mackenzie, D. H. Petersen, A. Pesquera, A. Centeno, P. Bøggild, A. Zurutuza, and P. U. Jepsen, "Terahertz wafer-scale mobility mapping of graphene on insulating substrates without a gate," Opt. Express **23**, 30721–30729 (2015).
120. D. M. Mittleman, S. Hunsche, L. Boivin, and M. C. Nuss, "T-ray tomography," Opt. Lett. **22**, 904–906 (1997).
121. J. A. Zeitler, P. F. Taday, D. A. Newnham, M. Pepper, K. C. Gordon, and T. Rades, "Terahertz pulsed spectroscopy and imaging in the pharmaceutical setting—a review," J. Pharm. Pharmacol. **59**, 209–223 (2007).
122. Y.-C. Shen, "Terahertz pulsed spectroscopy and imaging for pharmaceutical applications: a review," Int. J. Pharm. **417**, 48–60 (2011).
123. M. Haaser, K. C. Gordon, C. J. Strachan, and T. Rades, "Terahertz pulsed imaging as an advanced characterisation tool for film coatings—a review," Int. J. Pharm. **457**, 510–520 (2013).
124. A. J. Fitzgerald, B. E. Cole, and P. F. Taday, "Nondestructive analysis of tablet coating thicknesses using terahertz pulsed imaging," J. Pharm. Sci. **94**, 177–183 (2005).
125. L. Ho, R. Müller, M. Römer, K. C. Gordon, J. Heinämäki, P. Kleinebudde, M. Pepper, T. Rades, Y. C. Shen, C. J. Strachan, P. F. Taday, and J. A. Zeitler, "Analysis of sustained-release tablet film coats using terahertz pulsed imaging," J. Control. Release **119**, 253–261 (2007).
126. R. K. May, M. J. Evans, S. Zhong, I. Warr, L. F. Gladden, Y. Shen, and J. A. Zeitler, "Terahertz in-line sensor for direct coating thickness measurement of individual tablets during film coating in real-time," J. Pharm. Sci. **100**, 1535–1544 (2011).
127. R. K. May, K. Su, L. Han, S. Zhong, J. A. Elliott, L. F. Gladden, M. Evans, Y. Shen, and J. A. Zeitler, "Hardness and density distributions of pharmaceutical tablets measured by terahertz pulsed imaging," J. Pharm. Sci. **102**, 2179–2186 (2013).
128. P. Bawuah, A. Pierotic Mendia, P. Silfsten, P. Pääkkönen, T. Ervasti, J. Ketolainen, J. A. Zeitler, and K. E. Peiponen, "Detection of porosity of pharmaceutical compacts by terahertz radiation transmission and light reflection measurement techniques," Int. J. Pharm. **465**, 70–76 (2014).
129. K. Su, Y. C. Shen, and J. A. Zeitler, "Terahertz sensor for non-contact thickness and quality measurement of automobile paints of varying complexity," IEEE Trans. Terahertz Sci. Technol. **4**, 432–439 (2014).
130. A. J. L. Adam, P. C. M. Planken, S. Meloni, and J. Dik, "Terahertz imaging of hidden paint layers on canvas," in *34th International Conference Infrared, Millimeter, Terahertz Waves (IRMMW-THz)* (2009), Vol. **17**, pp. 904–906.
131. K. Fukunaga and M. Picollo, "Terahertz spectroscopy applied to the analysis of artists' materials," Appl. Phys. A **100**, 591–597 (2010).
132. C. Seco-Martorell, V. López-Domínguez, G. Arauz-Garofalo, A. Redo-Sanchez, J. Palacios, and J. Tejada, "Goya's artwork imaging with terahertz waves," Opt. Express **21**, 17800–17805 (2013).
133. E. Abraham and K. Fukunaga, "Terahertz imaging applied to the examination of artistic objects," Stud. Conserv. **60**, 343–352 (2015).
134. C. L. Koch-Dandolo, T. Filtenborg, K. Fukunaga, J. Skou-Hansen, and P. U. Jepsen, "Reflection terahertz time-domain imaging for analysis of an 18th century neoclassical easel painting," Appl. Opt. **54**, 5123–5129 (2015).

135. A. Redo-Sanchez, B. Heshmat, A. Aghasi, S. Naqvi, M. Zhang, J. Romberg, and R. Raskar, "Terahertz time-gated spectral imaging for content extraction through layered structures," Nat. Commun. **7**, 12665 (2016).
136. A. Aghasi and J. Romberg, "Convex cardinal shape composition," SIAM J. Imaging Sci. **8**, 2887–2950 (2015).
137. S.-H. Cho, S.-H. Lee, C. Nam-Gung, S.-J. Oh, J.-H. Son, H. Park, and C.-B. Ahn, "Fast terahertz reflection tomography using block-based compressed sensing," Opt. Express **19**, 16401–16409 (2011).
138. S. Wang and X.-C. Zhang, "Pulsed terahertz tomography," J. Phys. D **37**, R1–R36 (2004).
139. V. P. Wallace, E. Macpherson, J. A. Zeitler, and C. Reid, "Three-dimensional imaging of optically opaque materials using nonionizing terahertz radiation," J. Opt. Soc. Am. A **25**, 3120–3133 (2008).
140. B. Ferguson, S. Wang, D. Gray, D. Abbot, and X.-C. Zhang, "T-ray computed tomography," Opt. Lett. **27**, 1312–1314 (2002).
141. B. Ferguson, S. H. Wang, D. Gray, D. Abbott, and X. C. Zhang, "Towards functional 3D T-ray imaging," Phys. Med. Biol. **47**, 3735–3742 (2002).
142. A. Brahm, M. Kunz, S. Riehemann, G. Notni, and A. Tünnermann, "Volumetric spectral analysis of materials using terahertz-tomography techniques," Appl. Phys. B **100**, 151–158 (2010).
143. A. C. Kak and M. Stanley, "Algorithms for reconstruction with nondiffracting sources," in *Principles of Computerized Tomographic Imaging* (IEEE, 1999), pp. 49–112.
144. B. Recur, A. Younus, S. Salort, P. Mounaix, B. Chassagne, P. Desbarats, J.-P. Caumes, and E. Abraham, "Investigation on reconstruction methods applied to 3D terahertz computed tomography," Opt. Express **19**, 5105–5117 (2011).
145. A. Brahm, M. Tymoshchuk, F. Wichmann, S. Merx, G. Notni, and A. Tünnermann, "Wavelet based identification of substances in terahertz tomography measurements," J. Infrared Millim. Terahertz Waves **35**, 974–986 (2014).
146. M. Bessou, B. Chassagne, J.-P. Caumes, C. Pradère, P. Maire, M. Tondusson, and E. Abraham, "Three-dimensional terahertz computed tomography of human bones," Appl. Opt. **51**, 6738–6744 (2012).
147. B. Recur, J. P. Guillet, I. Manek-Hönninger, J. C. Delagnes, W. Benharbone, P. Desbarats, J. P. Domenger, L. Canioni, and P. Mounaix, "Propagation beam consideration for 3D THz computed tomography," Opt. Express **20**, 5817–5829 (2012).
148. B. Recur, H. Balacey, J. Bou Sleiman, J. B. Perraud, J.-P. Guillet, A. Kingston, and P. Mounaix, "Ordered subsets convex algorithm for 3D terahertz transmission tomography," Opt. Express **22**, 23299–23309 (2014).
149. A. Bitman, S. Goldring, I. Moshe, and Z. Zalevsky, "Computed tomography using broadband Bessel THz beams and phase contrast," Opt. Lett. **39**, 1925–1928 (2014).
150. E. Abraham, A. Younus, C. Aguerre, P. Desbarats, and P. Mounaix, "Refraction losses in terahertz computed tomography," Opt. Commun. **283**, 2050–2055 (2010).
151. S. Mukherjee, J. Federici, P. Lopes, and M. Cabral, "Elimination of Fresnel reflection boundary effects and beam steering in pulsed terahertz computed tomography," J. Infrared Millim. Terahertz Waves **34**, 539–555 (2013).
152. A. Brahm, A. Wilms, M. Tymoshchuk, C. Grossmann, G. Notni, and A. Tünnermann, "Optical effects at projection measurements for terahertz tomography," Opt. Laser Technol. **62**, 49–57 (2014).

153. J.-P. Caumes, A. Younus, S. Salort, B. Chassagne, B. Recur, A. Ziéglé, A. Dautant, and E. Abraham, "Terahertz tomographic imaging of XVIIIth Dynasty Egyptian sealed pottery," Appl. Opt. **50**, 3604–3608 (2011).
154. M. Bessou, H. Duday, J. P. Caumes, S. Salort, B. Chassagne, A. Dautant, A. Ziéglé, and E. Abraham, "Advantage of terahertz radiation versus X-ray to detect hidden organic materials in sealed vessels," Opt. Commun. **285**, 4175–4179 (2012).
155. E. Abraham, M. Bessou, A. Ziéglé, M. C. Hervé, L. Szentmiklósi, Z. S. Kasztovszky, Z. Kis, and M. Menu, "Terahertz, X-ray and neutron computed tomography of an Eighteenth Dynasty Egyptian sealed pottery," Appl. Phys. A **117**, 963–972 (2014).
156. J. B. Perraud, A. F. Obaton, J. Bou-Sleiman, B. Recur, H. Balacey, F. Darracq, J. P. Guillet, and P. Mounaix, "Terahertz imaging and tomography as efficient instruments for testing polymer additive manufacturing objects," Appl. Opt. **55**, 3462–3467 (2016).
157. P. Hillger, A. Schluter, R. Jain, S. Malz, J. Grzyb, and U. Pfeiffer, "Low-cost 0.5 THz computed tomography based on silicon components," in *International Conference on Infrared, Millimeter, Terahertz Waves (IRMMW-THz)* (IEEE, 2017).
158. D. Coquillat, V. Nodjiadjim, A. Duhant, M. Triki, O. Strauss, A. Konczykowska, M. Riet, N. Dyakonova, and W. Knap, "High-speed InP-based double heterojunction bipolar transistors and varactors for three-dimensional terahertz computed tomography," in *International Conference on Infrared, Millimeter, and Terahertz Waves (IRMMW-THz)* (IEEE, 2017).
159. Q. Li, Y. Da Li, S. H. Ding, and Q. Wang, "Terahertz computed tomography using a continuous-wave gas laser," J. Infrared Millim. Terahertz Waves **33**, 548–558 (2012).
160. T. Kashiwagi, K. Nakade, Y. Saiwai, H. Minami, T. Kitamura, C. Watanabe, K. Ishida, S. Sekimoto, K. Asanuma, T. Yasui, Y. Shibano, M. Tsujimoto, T. Yamamoto, B. Marković, J. Mirković, R. A. Klemm, and K. Kadowaki, "Computed tomography image using sub-terahertz waves generated from a high- T_c superconducting intrinsic Josephson junction oscillator," Appl. Phys. Lett. **104**, 082603 (2014).
161. S. R. Tripathi, Y. Sugiyama, K. Murate, K. Imayama, and K. Kawase, "Terahertz wave three-dimensional computed tomography based on injection-seeded terahertz wave parametric emitter and detector," Opt. Express **24**, 6433–6440 (2016).
162. B. Li, D. Wang, X. Zhou, L. Rong, H. Huang, M. Wan, and Y. Wang, "Terahertz computed tomography in three-dimensional using a pyroelectric array detector," Proc. SPIE **10233**, 102331F (2017).
163. M. Jewariya, E. Abraham, T. Kitaguchi, Y. Ohgi, M. Minami, T. Araki, and T. Yasui, "Fast three-dimensional terahertz computed tomography using real-time line projection of intense terahertz pulse," Opt. Express **21**, 2423–2433 (2013).
164. N. Rothbart, H. Richter, M. Wienold, L. Schrottke, H. T. Grahn, and H. W. Hubers, "Fast 2-D and 3-D terahertz imaging with a quantum-cascade laser and a scanning mirror," IEEE Trans. Terahertz Sci. Technol. **3**, 617–624 (2013).
165. T. Mohr, A. Herdt, and W. Elsässer, "2D tomographic terahertz imaging using a single pixel detector," Opt. Express **26**, 3353–3367 (2018).
166. J. W. Goodman, *Introduction to Fourier Optics*, 2nd ed. (McGraw-Hill, 1996).
167. T. Yuan, J. Z. Xu, and X. C. Zhang, "Development of terahertz wave microscopes," Infrared Phys. Technol. **45**, 417–425 (2004).
168. W. Withayachumnankul, G. M. Png, X. Yin, S. Atakaramians, I. Jones, H. Lin, B. S. Y. Ung, J. Balakrishnan, B. W. H. Ng, B. Ferguson, S. P. Mickan,

B. M. Fischer, and D. Abbott, "T-ray sensing and imaging," Proc. IEEE **95**, 1528–1558 (2007).
169. A. J. L. Adam, "Review of near-field terahertz measurement methods and their applications: how to achieve sub-wavelength resolution at THz frequencies," J. Infrared Millim. Terahertz Waves **32**, 976–1019 (2011).
170. F. Blanchard, A. Doi, T. Tanaka, and K. Tanaka, "Real-time, subwavelength terahertz imaging," Annu. Rev. Mater. Res. **43**, 237–259 (2013).
171. N. N. Zinov'ev and A. V. Andrianov, "Confocal terahertz imaging," Appl. Phys. Lett. **95**, 011114 (2009).
172. M. A. Salhi, I. Pupeza, and M. Koch, "Confocal THz laser microscope," J. Infrared Millim. Terahertz Waves **31**, 358–366 (2010).
173. U. S. de Cumis, J.-H. Xu, L. Masini, R. Degl'Innocenti, P. Pingue, F. Beltram, A. Tredicucci, M. S. Vitiello, P. A. Benedetti, H. E. Beere, and D. A. Ritchie, "Terahertz confocal microscopy with a quantum cascade laser source," Opt. Express **20**, 21924–21931 (2012).
174. M. Flammini, C. Bonsi, C. Ciano, V. Giliberti, E. Pontecorvo, P. Italia, E. DelRe, and M. Ortolani, "Confocal terahertz imaging of ancient manuscripts," J. Infrared Millim. Terahertz Waves **38**, 435–442 (2017).
175. H. H. Nguyen Pham, S. Hisatake, O. V. Minin, T. Nagatsuma, and I. V. Minin, "Enhancement of spatial resolution of terahertz imaging systems based on terajet generation by dielectric cube," APL Photon. **2**, 056106 (2017).
176. L. Yue, B. Yan, J. N. Monks, R. Dhama, Z. Wang, O. V. Minin, and I. V. Minin, "A millimetre-wave cuboid solid immersion lens with intensity-enhanced amplitude mask apodization," J. Infrared Millim. Terahertz Waves **39**, 546–552 (2018).
177. Y. Yang, H. Liu, M. Yang, B. Cui, and W. Zhang, "Dielectric sphere-coupled THz super-resolution imaging," Appl. Phys. Lett. **113**, 031105 (2018).
178. N. V. Chernomyrdin, A. O. Schadko, S. P. Lebedev, V. L. Tolstoguzov, V. N. Kurlov, I. V. Reshetov, I. E. Spektor, M. Skorobogatiy, S. O. Yurchenko, and K. I. Zaytsev, "Solid immersion terahertz imaging with sub-wavelength resolution," Appl. Phys. Lett. **110**, 221109 (2017).
179. N. V. Chernomyrdin, A. S. Kucheryavenko, G. S. Kolontaeva, G. M. Katyba, I. N. Dolganova, P. A. Karalkin, D. S. Ponomarev, V. N. Kurlov, I. V. Reshetov, M. Skorobogatiy, V. V. Tuchin, and K. I. Zaytsev, "Reflection-mode continuous-wave 0.15 λ -resolution terahertz solid immersion microscopy of soft biological tissues," Appl. Phys. Lett. **113**, 111102 (2018).
180. A. J. L. Adam, J. M. Brok, P. C. M. Planken, M. A. Seo, and D. S. Kim, "THz near-field measurements of metal structures," C. R. Phys. **9**, 161–168 (2008).
181. M. A. Seo, A. J. L. Adam, J. H. Kang, J. W. Lee, S. C. Jeoung, Q. H. Park, P. C. M. Planken, and D. S. Kim, "Fourier-transform terahertz near-field imaging of one-dimensional slit arrays: mapping of electric-field-, magnetic-field-, and Poynting vectors," Opt. Express **15**, 11781–11789 (2007).
182. J. Grzyb, B. Heinemann, and U. R. Pfeiffer, "Solid-state terahertz superresolution imaging device in 130-nm SiGe BiCMOS technology," IEEE Trans. Microw. Theory Tech. **65**, 4357–4372 (2017).
183. K. Ahi and M. Anwar, "Developing terahertz imaging equation and enhancement of the resolution of terahertz images using deconvolution," Proc. SPIE **9856**, 98560N (2016).
184. K. Ahi, "Mathematical modeling of THz point spread function and simulation of THz imaging systems," IEEE Trans. Terahertz Sci. Technol. **7**, 747–754 (2017).

185. O. Mitrofanov, M. Lee, J. W. P. Hsu, I. Brener, R. Harel, J. F. Federici, J. D. Wynn, L. N. Pfeiffer, and K. W. West, "Collection-mode near-field imaging with 0.5-THz pulses," IEEE J. Sel. Top. Quantum Electron. **7**, 600–607 (2001).
186. S. Hunsche, M. Koch, I. Brener, and M. Nuss, "THz near-field imaging," Opt. Commun. **150**, 22–26 (1998).
187. Q. Chen, Z. Jiang, G. X. Xu, and X.-C. Zhang, "Near-field terahertz imaging with a dynamic aperture," Opt. Lett. **25**, 1122–1124 (2000).
188. O. Mitrofanov, M. Lee, J. W. P. Hsu, L. N. Pfeiffer, K. W. West, J. D. Wynn, and J. F. Federici, "Terahertz pulse propagation through small apertures," Appl. Phys. Lett. **79**, 907–909 (2001).
189. J. F. Federici, O. Mitrofanov, M. Lee, J. W. P. Hsu, I. Brener, R. Harel, J. D. Wynn, L. N. Pfeiffer, and K. W. West, "Terahertz near-field imaging," Phys. Med. Biol. **47**, 3727–3734 (2002).
190. H. A. Bethe, "Theory of diffraction by small holes," Phys. Rev. **66**, 163–182 (1944).
191. C. J. Bouwkamp, "On the diffraction of electromagnetic waves by small circular disks and holes," Philips Res. Rep. **5**, 401–422 (1950).
192. K. Ishihara, T. Ikari, H. Minamide, J. I. Shikata, K. Ohashi, H. Yokoyama, and H. Ito, "Terahertz near-field imaging using enhanced transmission through a single subwavelength aperture," Jpn. J. Appl. Phys. **44**, L929–L931 (2005).
193. K. Ishihara, K. Ohashi, T. Ikari, H. Minamide, H. Yokoyama, J. I. Shikata, and H. Ito, "Terahertz-wave near-field imaging with subwavelength resolution using surface-wave-assisted bow-tie aperture," Appl. Phys. Lett. **89**, 201120 (2006).
194. A. J. Macfaden, J. L. Reno, I. Brener, and O. Mitrofanov, "3 μm aperture probes for near-field terahertz transmission microscopy," Appl. Phys. Lett. **104**, 011110 (2014).
195. O. Mitrofanov, I. Brener, T. S. Luk, and J. L. Reno, "Photoconductive terahertz near-field detector with a hybrid nanoantenna array cavity," ACS Photon. **2**, 1763–1768 (2015).
196. N. C. J. Van Der Valk and P. C. M. Planken, "Electro-optic detection of sub-wavelength terahertz spot sizes in the near field of a metal tip," Appl. Phys. Lett. **81**, 1558–1560 (2002).
197. H. T. Chen, R. Kersting, and G. C. Cho, "Terahertz imaging with nanometer resolution," Appl. Phys. Lett. **83**, 3009–3011 (2003).
198. A. J. Huber, F. Keilmann, J. Wittborn, J. Aizpurua, and R. Hillenbrand, "Terahertz near-field nanoscopy of nanodevices," Nano Lett. **8**, 3766–3770 (2008).
199. M. Yamashita, K. Kawase, and C. Otani, "Imaging of large-scale integrated circuits using laser terahertz emission microscopy," Opt. Express **13**, 115–120 (2005).
200. P. Klarskov, H. Kim, V. L. Colvin, and D. M. Mittleman, "Nanoscale laser terahertz emission microscopy," ACS Photon. **4**, 2676–2680 (2017).
201. T. L. Cocker, V. Jelic, M. Gupta, S. J. Molesky, J. A. J. Burgess, G. D. L. Reyes, L. V. Titova, Y. Y. Tsui, M. R. Freeman, and F. A. Hegmann, "An ultrafast terahertz scanning tunnelling microscope," Nat. Photonics **7**, 620–625 (2013).
202. T. L. Cocker, D. Peller, P. Yu, J. Repp, and R. Huber, "Tracking the ultrafast motion of a single molecule by femtosecond orbital imaging," Nature **539**, 263–267 (2016).
203. Y.-S. Lee, "Generation and detection of broadband terahertz pulses," in *Principles of Terahertz Science and Technology* (Springer, 2009), Vol. **2**, pp. 51–116.
204. Y. C. Shen, P. C. Upadhya, H. E. Beere, E. H. Linfield, A. G. Davies, I. S. Gregory, C. Baker, W. R. Tribe, and M. J. Evans, "Generation and detection

of ultrabroadband terahertz radiation using photoconductive emitters and receivers," Appl. Phys. Lett. **85**, 164–166 (2004).
205. N. T. Yardimci, S.-H. Yang, C. W. Berry, and M. Jarrahi, "High-power terahertz generation using large-area plasmonic photoconductive emitters," IEEE Trans. Terahertz Sci. Technol. **5**, 223–229 (2015).
206. M. Jarrahi, "Advanced photoconductive terahertz optoelectronics based on nano-antennas and nano-plasmonic light concentrators," IEEE Trans. Terahertz Sci. Technol. **5**, 391–397 (2015).
207. M. Ashida, "Ultra-broadband terahertz wave detection using photoconductive antenna," Jpn. J. Appl. Phys. **47**, 8221–8225 (2008).
208. P. U. Jepsen, D. G. Cooke, and M. Koch, "Terahertz spectroscopy and imaging—modern techniques and applications," Laser Photon. Rev. **5**, 124–166 (2011).
209. C. W. Berry, N. Wang, M. R. Hashemi, M. Unlu, and M. Jarrahi, "Significant performance enhancement in photoconductive terahertz optoelectronics by incorporating plasmonic contact electrodes," Nat. Commun. **4**, 1622 (2013).
210. N. T. Yardimci and M. Jarrahi, "High sensitivity terahertz detection through large-area plasmonic nano-antenna arrays," Sci. Rep. **7**, 42667 (2017).
211. J. R. Freeman, H. E. Beere, and D. A. Ritchie, "Generation and detection of terahertz radiation," in *Terahertz Spectroscopy and Imaging* (Springer, 2012), pp. 1–28.
212. A. Nahata, A. S. Weling, and T. F. Heinz, "A wideband coherent terahertz spectroscopy system using optical rectification and electro-optic sampling," Appl. Phys. Lett. **69**, 2321–2323 (1996).
213. J. Hebling, G. Almasi, I. Kozma, and J. Kuhl, "Velocity matching by pulse front tilting for large area THz-pulse generation," Opt. Express **10**, 1161–1166 (2002).
214. A. G. Stepanov, J. Hebling, and J. Kuhl, "Efficient generation of subpicosecond terahertz radiation by phase-matched optical rectification using ultrashort laser pulses with tilted pulse fronts," Appl. Phys. Lett. **83**, 3000–3002 (2003).
215. J. Hebling, K.-L. Yeh, M. C. Hoffmann, B. Bartal, and K. A. Nelson, "Generation of high-power terahertz pulses by tilted-pulse-front excitation and their application possibilities," J. Opt. Soc. Am. B **25**, B6–B19 (2008).
216. H. Hirori, A. Doi, F. Blanchard, and K. Tanaka, "Single-cycle terahertz pulses with amplitudes exceeding 1 MV/cm generated by optical rectification in $LiNbO_3$," Appl. Phys. Lett. **98**, 091106 (2011).
217. M. J. Khan, J. C. Chen, and S. Kaushik, "Optical detection of terahertz radiation by using nonlinear parametric upconversion," Opt. Lett. **32**, 3248–3250 (2007).
218. R. Guo, S. Ohno, H. Minamide, T. Ikari, and H. Ito, "Highly sensitive coherent detection of terahertz waves at room temperature using a parametric process," Appl. Phys. Lett. **93**, 021106 (2008).
219. K. Murate, Y. Taira, S. R. Tripathi, S. Hayashi, K. Nawata, H. Minamide, and K. Kawase, "A high dynamic range and spectrally flat terahertz spectrometer based on optical parametric processes in $LiNbO_3$," IEEE Trans. Terahertz Sci. Technol. **4**, 523–526 (2014).
220. M. Mohara, K. Shimura, K. Aiko, N. Shiramizu, K. Murate, and K. Kawase, "Pharmaceutical tablet inspection with injection-seeded terahertz parametric generation technique," in *International Conference on Infrared, Millimeter, Terahertz Waves (IRMMW-THz)* (IEEE, 2016).
221. L. Liu and N. G. Chen, "Double-pass rotary mirror array for fast scanning optical delay line," Appl. Opt. **45**, 5426–5431 (2006).
222. P.-L. Hsiung, X. Li, C. Chudoba, I. Hartl, T. H. Ko, and J. G. Fujimoto, "High-speed path-length scanning with a multiple-pass cavity delay line," Appl. Opt. **42**, 640–648 (2003).

223. X. Liu, M. J. Cobb, and X. Li, "Rapid scanning all-reflective optical delay line for real-time optical coherence tomography," Opt. Lett. **29**, 80–82 (2004).
224. K. Locharoenrat and I. Hsu, "Optical delay line for rapid scanning low-coherence reflectometer," Int. J. Inf. Electron. Eng. **2**, 904–906 (2012).
225. D. C. Edelstein, R. B. Romney, and M. Scheuermann, "Rapid programmable 300 ps optical delay scanner and signal-averaging system for ultrafast measurements," Rev. Sci. Instrum. **62**, 579–583 (1991).
226. J. Xu and X.-C. Zhang, "Circular involute stage," Opt. Lett. **29**, 2082–2084 (2004).
227. G. J. Kim, S. G. Jeon, J.-I. Kim, and Y. S. Jin, "Terahertz pulse detection using rotary optical delay line," Jpn. J. Appl. Phys. **46**, 7332–7335 (2007).
228. G. J. Kim, S. G. Jeon, J.-I. Kim, and Y. S. Jin, "High speed scanning of terahertz pulse by a rotary optical delay line," Rev. Sci. Instrum. **79**, 106102 (2008).
229. M. Skorobogatiy, "Linear rotary optical delay lines," Opt. Express **22**, 11812–11833 (2014).
230. H. Guerboukha, A. Markov, H. Qu, and M. Skorobogatiy, "Time resolved dynamic measurements at THz frequencies using a rotary optical delay line," IEEE Trans. Terahertz Sci. Technol. **5**, 564–572 (2015).
231. J. Ballif, R. Gianotti, P. Chavanne, R. Walti, and R. Salathé, "Rapid and scalable scans at 21 m/s in optical low-coherence reflectometry," Opt. Lett. **22**, 757–759 (1997).
232. J. Szydlo, N. Delachenal, R. Gianotti, R. Wälti, H. Bleuler, and R. Salathé, "Air-turbine driven optical low-coherence reflectometry at 28.6-kHz scan repetition rate," Opt. Commun. **154**, 1–4 (1998).
233. T. Probst, A. Rehn, S. F. Busch, S. Chatterjee, M. Koch, and M. Scheller, "Cost-efficient delay generator for fast terahertz imaging," Opt. Lett. **39**, 4863–4866 (2014).
234. R. J. Kneisler, F. E. Lytle, G. J. Fiechtner, Y. Jiang, G. B. King, and N. M. Laurendeau, "Asynchronous optical sampling: a new combustion diagnostic for potential use in turbulent, high-pressure flames," Opt. Lett. **14**, 260–262 (1989).
235. G. J. Fiechtner, G. B. King, N. M. Laurendeau, and F. E. Lytle, "Measurements of atomic sodium in flames by asynchronous optical sampling: theory and experiment," Appl. Opt. **31**, 2849–2864 (1992).
236. T. Yasui, E. Saneyoshi, and T. Araki, "Asynchronous optical sampling terahertz time-domain spectroscopy for ultrahigh spectral resolution and rapid data acquisition," Appl. Phys. Lett. **87**, 061101 (2005).
237. C. Janke, M. Först, M. Nagel, H. Kurz, and A. Bartels, "Asynchronous optical sampling for high-speed characterization of integrated resonant terahertz sensors," Opt. Lett. **30**, 1405–1407 (2005).
238. A. Bartels, R. Cerna, C. Kistner, A. Thoma, F. Hudert, C. Janke, and T. Dekorsy, "Ultrafast time-domain spectroscopy based on high-speed asynchronous optical sampling," Rev. Sci. Instrum. **78**, 035107 (2007).
239. O. Kliebisch, D. C. Heinecke, and T. Dekorsy, "Ultrafast time-domain spectroscopy system using 10 GHz asynchronous optical sampling with 100 kHz scan rate," Opt. Express **24**, 29930–29940 (2016).
240. S. Kray, F. Spöler, T. Hellerer, and H. Kurz, "Electronically controlled coherent linear optical sampling for optical coherence tomography," Opt. Express **18**, 9976–9990 (2010).
241. Y. Kim and D.-S. Yee, "High-speed terahertz time-domain spectroscopy based on electronically controlled optical sampling," Opt. Lett. **35**, 3715–3717 (2010).
242. R. J. B. Dietz, N. Vieweg, T. Puppe, A. Zach, B. Globisch, T. Göbel, P. Leisching, and M. Schell, "All fiber-coupled THz-TDS system with kHz

measurement rate based on electronically controlled optical sampling," Opt. Lett. **39**, 6482–6485 (2014).
243. D. Stehr, C. M. Morris, C. Schmidt, and M. S. Sherwin, "High-performance fiber-laser-based terahertz spectrometer," Opt. Lett. **35**, 3799–3801 (2010).
244. T. Hochrein, R. Wilk, M. Mei, R. Holzwarth, N. Krumbholz, and M. Koch, "Optical sampling by laser cavity tuning," Opt. Express **18**, 1613–1617 (2010).
245. R. Wilk, T. Hochrein, M. Koch, M. Mei, and R. Holzwarth, "OSCAT: novel technique for time-resolved experiments without moveable optical delay lines," J. Infrared Millim. Terahertz Waves **32**, 596–602 (2011).
246. R. Wilk, T. Hochrein, M. Koch, M. Mei, and R. Holzwarth, "Terahertz spectrometer operation by laser repetition frequency tuning," J. Opt. Soc. Am. B **28**, 592–594 (2011).
247. A. Brahm, A. Wilms, R. J. B. Dietz, T. Göbel, M. Schell, G. Notni, and A. Tünnermann, "Multichannel terahertz time-domain spectroscopy system at 1030 nm excitation wavelength," Opt. Express **22**, 12982–12993 (2014).
248. A. Brahm, M. Muller, C. Gerth, and G. Notni, "Development of a multichannel lock-in amplifier for terahertz time-domain systems," in *International Conference on Infrared, Millimeter, Terahertz Waves (IRMMW-THz)* (IEEE, 2012).
249. B. Pradarutti, R. Müller, W. Freese, G. Matthäus, S. Riehemann, G. Notni, S. Nolte, and A. Tünnermann, "Terahertz line detection by a microlens array coupled photoconductive antenna array," Opt. Express **16**, 18443–18450 (2008).
250. K. Nallappan, J. Li, H. Guerboukha, A. Markov, B. Petrov, D. Morris, and M. Skorobogatiy, "A dynamically reconfigurable terahertz array antenna for 2D-imaging applications," in *Photonics North (PN)* (IEEE, 2017).
251. Z. Jiang and X. C. Zhang, "2D measurement and spatio-temporal coupling of few-cycle THz pulses," Opt. Express **5**, 243–248 (1999).
252. Z. Jiang, X. G. Xu, and X.-C. Zhang, "Improvement of terahertz imaging with a dynamic subtraction technique," Appl. Opt. **39**, 2982–2987 (2000).
253. F. Miyamaru, T. Yonera, M. Tani, and M. Hangyo, "Terahertz two-dimensional electrooptic sampling using high speed complementary metal-oxide semiconductor camera," Jpn. J. Appl. Phys. **43**, L489 (2004).
254. B. Pradarutti, R. Müller, G. Matthäus, C. Brückner, S. Riehemann, G. Notni, S. Nolte, and A. Tünnermann, "Multichannel balanced electro-optic detection for terahertz imaging," Opt. Express **15**, 17652–17660 (2007).
255. X. Wang, Y. Cui, W. Sun, J. Ye, and Y. Zhang, "Terahertz real-time imaging with balanced electro-optic detection," Opt. Commun. **283**, 4626–4632 (2010).
256. N. C. J. van der Valk, T. Wenckebach, and P. C. M. Planken, "Full mathematical description of electro-optic detection in optically isotropic crystals," J. Opt. Soc. Am. B **21**, 622–631 (2004).
257. X. Wang, Y. Cui, W. Sun, J. Ye, and Y. Zhang, "Terahertz polarization real-time imaging based on balanced electro-optic detection," J. Opt. Soc. Am. A **27**, 2387–2393 (2010).
258. F. Blanchard, A. Doi, T. Tanaka, H. Hirori, H. Tanaka, Y. Kadoya, and K. Tanaka, "Real-time terahertz near-field microscope," Opt. Express **19**, 8277–8284 (2011).
259. F. Blanchard and K. Tanaka, "Improving time and space resolution in electro-optic sampling for near-field terahertz imaging," Opt. Lett. **41**, 4645–4648 (2016).
260. A. Doi, F. Blanchard, H. Hirori, and K. Tanaka, "Near-field THz imaging of free induction decay from a tyrosine crystal," Opt. Express **18**, 18419–18424 (2010).

261. F. Blanchard, K. Ooi, T. Tanaka, A. Doi, and K. Tanaka, "Terahertz spectroscopy of the reactive and radiative near-field zones of split ring resonator," Opt. Express **20**, 19395–19403 (2012).
262. A. Doi, F. Blanchard, T. Tanaka, and K. Tanaka, "Improving spatial resolution of real-time terahertz near-field microscope," J. Infrared Millim. Terahertz Waves **32**, 1043–1051 (2011).
263. Z. Jiang and X. C. Zhang, "Electro-optic measurement of THz field pulses with a chirped optical beam," Appl. Phys. Lett. **72**, 1945–1947 (1998).
264. Z. Jiang and X.-C. Zhang, "Single-shot spatiotemporal terahertz field imaging," Opt. Lett. **23**, 1114–1116 (1998).
265. Z. Jiang and X. C. Zhang, "Measurement of spatio-temporal terahertz field distribution by using chirped pulse technology," IEEE J. Quantum Electron. **36**, 1214–1222 (2000).
266. J. Shan, A. S. Weling, E. Knoesel, L. Bartels, M. Bonn, A. Nahata, G. A. Reider, and T. F. Heinz, "Single-shot measurement of terahertz electromagnetic pulses by use of electro-optic sampling," Opt. Lett. **25**, 426–428 (2000).
267. T. Yasuda, T. Yasui, T. Araki, and E. Abraham, "Real-time two-dimensional terahertz tomography of moving objects," Opt. Commun. **267**, 128–136 (2006).
268. T. Yasui, K. Sawanaka, A. Ihara, E. Abraham, M. Hashimoto, and T. Araki, "Real-time terahertz color scanner for moving objects," Opt. Express **16**, 1208–1221 (2008).
269. M. Schirmer, M. Fujio, M. Minami, J. Miura, T. Araki, and T. Yasui, "Biomedical applications of a real-time terahertz color scanner," Biomed. Opt. Express **1**, 354–366 (2010).
270. O. Morikawa, M. Tonouchi, and M. Hangyo, "Sub-THz spectroscopic system using a multimode laser diode and photoconductive antenna," Appl. Phys. Lett. **75**, 3772–3774 (1999).
271. I. S. Gregory, W. R. Tribe, M. J. Evans, T. D. Drysdale, D. R. S. Cumming, and M. Missous, "Multi-channel homodyne detection of continuous-wave terahertz radiation," Appl. Phys. Lett. **87**, 034106 (2005).
272. K. Shibuya, M. Tani, and M. Hangyo, "Compact and inexpensive continuous-wave sub-THz imaging system using a fiber-coupled multimode laser diode," in *31st International Conference on Infrared Millimeter Waves and 14th International Conference on Terahertz Electronics (IRMMW-THz)* (IEEE, 2006).
273. M. Scheller and M. Koch, "Terahertz quasi time domain spectroscopy," Opt. Express **17**, 17723–17733 (2009).
274. M. Scheller, S. F. Dürrschmidt, M. Stecher, and M. Koch, "Terahertz quasi-time-domain spectroscopy imaging," Appl. Opt. **50**, 1884–1888 (2011).
275. T. Probst, A. Rehn, and M. Koch, "Compact and low-cost THz QTDS system," Opt. Express **23**, 21972–21982 (2015).
276. R. B. Kohlhaas, A. Rehn, S. Nellen, M. Koch, M. Schell, R. J. B. Dietz, and J. C. Balzer, "Terahertz quasi time-domain spectroscopy based on telecom technology for 1550 nm," Opt. Express **25**, 12851–12859 (2017).
277. X. Wu and K. Sengupta, "Dynamic waveform shaping with picosecond time widths," IEEE J. Solid-State Circuits **52**, 389–405 (2017).
278. M. M. Assefzadeh and A. Babakhani, "Broadband oscillator-free THz pulse generation and radiation based on direct digital-to-impulse architecture," IEEE J. Solid-State Circuits **52**, 2905–2919 (2017).
279. X. Wu and K. Sengupta, "On-chip THz spectroscope exploiting electromagnetic scattering with multi-port antenna," IEEE J. Solid-State Circuits **51**, 3049–3062 (2016).

280. N. Karpowicz, H. Zhong, J. Xu, K.-I. Lin, J.-S. Hwang, and X.-C. Zhang, "Comparison between pulsed terahertz time-domain imaging and continuous wave terahertz imaging," Semicond. Sci. Technol. **20**, S293–S299 (2005).
281. Y.-S. Lee, "Continuous-wave terahertz sources and detectors," in *Principles of Terahertz Science and Technology* (Springer, 2009), pp. 117–157.
282. J. Yang, S. Ruan, and M. Zhang, "Real-time, continuous-wave terahertz imaging by a pyroelectric camera," Chin. Opt. Lett. **6**, 29–31 (2008).
283. P. L. Richards, "Bolometers for infrared and millimeter waves," J. Appl. Phys. **76**, 1–24 (1994).
284. A. W. Lee and Q. Hu, "Real-time, continuous-wave terahertz imaging by use of a microbolometer focal-plane array," Opt. Lett. **30**, 2563–2565 (2005).
285. A. W. M. Lee, B. S. Wil, S. Kumar, Q. Hu, and J. L. Reno, "Real-time imaging using a 4.3-THz quantum cascade laser and a 320×240 microbolometer focal-plane array," IEEE Photon. Technol. Lett. **18**, 1415–1417 (2006).
286. B. N. Behnken, G. Karunasiri, D. R. Chamberlin, P. R. Robrish, and J. Faist, "Real-time imaging using a 28 THz quantum cascade laser and uncooled infrared microbolometer camera," Opt. Lett. **33**, 440–442 (2008).
287. M. A. Dem'yanenko, D. G. Esaev, B. A. Knyazev, G. N. Kulipanov, and N. A. Vinokurov, "Imaging with a 90 frames/s microbolometer focal plane array and high-power terahertz free electron laser," Appl. Phys. Lett. **92**, 131116 (2008).
288. A. W. M. Lee, Q. Qin, S. Kumar, B. S. Williams, Q. Hu, and J. L. Reno, "Real-time terahertz imaging over a standoff distance (>25 meters)," Appl. Phys. Lett. **89**, 141125 (2006).
289. N. Oda, S. Kurashina, M. Miyoshi, K. Doi, T. Ishi, T. Sudou, T. Morimoto, H. Goto, and T. Sasaki, "Microbolometer terahertz focal plane array and camera with improved sensitivity in the sub-terahertz region," J. Infrared Millim. Terahertz Waves **36**, 947–960 (2015).
290. N. Nemoto, N. Kanda, R. Imai, K. Konishi, M. Miyoshi, S. Kurashina, T. Sasaki, N. Oda, and M. Kuwata-Gonokami, "High-sensitivity and broadband, real-time terahertz camera incorporating a micro-bolometer array with resonant cavity structure," IEEE Trans. Terahertz Sci. Technol. **6**, 175–182 (2016).
291. N. Kanda, K. Konishi, N. Nemoto, K. Midorikawa, and M. Kuwata-Gonokami, "Real-time broadband terahertz spectroscopic imaging by using a high-sensitivity terahertz camera," Sci. Rep. **7**, 42540 (2017).
292. D.-T. Nguyen, F. Simoens, J.-L. Ouvrier-Buffet, J. Meilhan, and J.-L. Coutaz, "Broadband THz uncooled antenna-coupled microbolometer array—electromagnetic design, simulations and measurements," IEEE Trans. Terahertz Sci. Technol. **2**, 299–305 (2012).
293. F. Simoens and J. Meilhan, "Terahertz real-time imaging uncooled array based on antenna- and cavity-coupled bolometers," Philos. Trans. R. Soc. London A **372**, 0111 (2014).
294. F. Alves, B. Kearney, D. Grbovic, N. V. Lavrik, and G. Karunasiri, "Strong terahertz absorption using SiO_2/Al based metamaterial structures," Appl. Phys. Lett. **100**, 111104 (2012).
295. B. Kearney, F. Alves, D. Grbovic, and G. Karunasiri, "Al/SiO_x/Al single and multiband metamaterial absorbers for terahertz sensor applications," Opt. Eng. **52**, 013801 (2013).
296. W. Withayachumnankul, C. M. Shah, C. Fumeaux, B. S. Y. Ung, W. J. Padilla, M. Bhaskaran, D. Abbott, and S. Sriram, "Plasmonic resonance toward terahertz perfect absorbers," ACS Photon. **1**, 625–630 (2014).
297. K. Fan, J. Y. Suen, X. Liu, and W. J. Padilla, "All-dielectric metasurface absorbers for uncooled terahertz imaging," Optica **4**, 601–604 (2017).

298. I. E. Carranza, J. P. Grant, J. Gough, and D. Cumming, "Terahertz metamaterial absorbers implemented in CMOS technology for imaging applications: scaling to large format focal plane arrays," IEEE J. Sel. Top. Quantum Electron. **23**, 4700508 (2017).
299. W. Knap, S. Rumyantsev, M. S. Vitiello, D. Coquillat, S. Blin, N. Dyakonova, M. Shur, F. Teppe, A. Tredicucci, and T. Nagatsuma, "Nanometer size field effect transistors for terahertz detectors," Nanotechnology **24**, 214002 (2013).
300. W. Knap and M. I. Dyakonov, "Field effect transistors for terahertz applications," in *Handbook of Terahertz Technology for Imaging, Sensing and Communications* (Elsevier, 2013), pp. 121–155.
301. A. Lisauskas, M. Bauer, S. Boppel, M. Mundt, B. Khamaisi, E. Socher, R. Venckevičius, L. Minkevičius, I. Kašalynas, D. Seliuta, G. Valušis, V. Krozer, and H. G. Roskos, "Exploration of terahertz imaging with silicon MOSFETs," J. Infrared Millim. Terahertz Waves **35**, 63–80 (2014).
302. M. I. Dyakonov and M. S. Shur, "Plasma wave electronics: novel terahertz devices using two dimensional electron fluid," IEEE Trans. Electron Devices **43**, 1640–1645 (1996).
303. J. Q. Lü and M. S. Shur, "Terahertz detection by high-electron-mobility transistor: enhancement by drain bias," Appl. Phys. Lett. **78**, 2587–2588 (2001).
304. F. Schuster, D. Coquillat, H. Videlier, M. Sakowicz, F. Teppe, L. Dussopt, B. Giffard, T. Skotnicki, and W. Knap, "Broadband terahertz imaging with highly sensitive silicon CMOS detectors," Opt. Express **19**, 7827–7832 (2011).
305. W. Knap, Y. Deng, S. Rumyantsev, J. Q. Lü, M. S. Shur, C. A. Saylor, and L. C. Brunel, "Resonant detection of subterahertz radiation by plasma waves in a submicron field-effect transistor," Appl. Phys. Lett. **80**, 3433–3435 (2002).
306. T. Otsuji, M. Hanabe, and O. Ogawara, "Terahertz plasma wave resonance of two-dimensional electrons in InGaP/InGaAs/GaAs high-electron-mobility transistors," Appl. Phys. Lett. **85**, 2119–2121 (2004).
307. M. Lee, M. C. Wanke, and J. L. Reno, "Millimeter wave mixing using plasmon and bolometric response in a double-quantum-well field-effect transistor," Appl. Phys. Lett. **86**, 033501 (2005).
308. A. El Fatimy, F. Teppe, N. Dyakonova, W. Knap, D. Seliuta, G. Valušis, A. Shchepetov, Y. Roelens, S. Bollaert, A. Cappy, and S. Rumyantsev, "Resonant and voltage-tunable terahertz detection in InGaAs/InP nanometer transistors," Appl. Phys. Lett. **89**, 131926 (2006).
309. V. I. Gavrilenko, E. V. Demidov, K. V. Marem'yanin, S. V. Morozov, W. Knap, and J. Lusakowski, "Electron transport and detection of terahertz radiation in a GaN/AlGaN submicrometer field-effect transistor," Semiconductors **41**, 232–234 (2007).
310. M. S. Vitiello, D. Coquillat, L. Viti, D. Ercolani, F. Teppe, A. Pitanti, F. Beltram, L. Sorba, W. Knap, and A. Tredicucci, "Room-temperature terahertz detectors based on semiconductor nanowire field-effect transistors," Nano Lett. **12**, 96–101 (2011).
311. L. Vicarelli, M. S. Vitiello, D. Coquillat, A. Lombardo, A. C. Ferrari, W. Knap, M. Polini, V. Pellegrini, and A. Tredicucci, "Graphene field-effect transistors as room-temperature terahertz detectors," Nat. Mater. **11**, 865–871 (2012).
312. L. Viti, J. Hu, D. Coquillat, W. Knap, A. Tredicucci, A. Politano, and M. S. Vitiello, "Black phosphorus terahertz photodetectors," Adv. Mater. **27**, 5567–5572 (2015).
313. W. Knap, F. Teppe, Y. Meziani, N. Dyakonova, J. Lusakowski, F. Boeuf, T. Skotnicki, D. Maude, S. Rumyantsev, and M. S. Shur, "Plasma wave detection of sub-terahertz and terahertz radiation by silicon field-effect transistors," Appl. Phys. Lett. **85**, 675–677 (2004).

314. N. Pala, F. Teppe, D. Veksler, Y. Deng, M. S. Shur, and R. Gaska, "Nonresonant detection of terahertz radiation by silicon-on-insulator MOSFETs," Electron. Lett. **41**, 447–449 (2005).
315. E. Öjefors, U. R. Pfeiffer, A. Lisauskas, and H. G. Roskos, "A 0.65 THz focal-plane array in a quarter-micron CMOS process technology," IEEE J. Solid-State Circuits **44**, 1968–1976 (2009).
316. A. Lisauskas, U. Pfeiffer, E. Öjefors, P. H. Bolvar, D. Glaab, and H. G. Roskos, "Rational design of high-responsivity detectors of terahertz radiation based on distributed self-mixing in silicon field-effect transistors," J. Appl. Phys. **105**, 114511 (2009).
317. D. Glaab, S. Boppel, A. Lisauskas, U. Pfeiffer, E. Öjefors, and H. G. Roskos, "Terahertz heterodyne detection with silicon field-effect transistors," Appl. Phys. Lett. **96**, 042106 (2010).
318. S. Boppel, A. Lisauskas, A. Max, V. Krozer, and H. G. Roskos, "CMOS detector arrays in a virtual 10-kilopixel camera for coherent terahertz real-time imaging," Opt. Lett. **37**, 536–538 (2012).
319. S. Boppel, A. Lisauskas, V. Krozer, and H. G. Roskos, "Performance and performance variations of sub-1 THz detectors fabricated with 0.15 μm CMOS foundry process," Electron. Lett. **47**, 661–662 (2011).
320. M. Bauer, R. Venckevičius, I. Kašalynas, S. Boppel, M. Mundt, A. Lisauskas, G. Valušis, and V. Krozer, "Antenna-coupled field-effect transistors for multi-spectral terahertz imaging up to 4. 25 THz," Opt. Express **22**, 19235–19241 (2014).
321. H. Sherry, J. Grzyb, Y. Zhao, R. Al Hadi, A. Cathelin, A. Kaiser, and U. Pfeiffer, "A 1kpixel CMOS camera chip for 25 fps real-time terahertz imaging applications," in *IEEE International Solid-State Circuits Conference* (2012), Vol. **55**, pp. 252–253.
322. J. Zdanevičius, M. Bauer, S. Boppel, V. Palenskis, A. Lisauskas, V. Krozer, and H. G. Roskos, "Camera for high-speed THz imaging," J. Infrared Millim. Terahertz Waves **36**, 986–997 (2015).
323. K. Sengupta and A. Hajimiri, "A 0.28 THz power-generation and beam-steering array in CMOS based on distributed active radiators," IEEE J. Solid-State Circuits **47**, 3013–3031 (2012).
324. Y. Tousi and E. Afshari, "A high-power and scalable 2-D phased array for terahertz CMOS integrated systems," IEEE J. Solid-State Circuits **50**, 597–609 (2015).
325. U. R. Pfeiffer, Y. Zhao, J. Grzyb, R. Al Hadi, N. Sarmah, W. Förster, H. Rücker, and B. Heinemann, "A 0.53 THz reconfigurable source module with up to 1 mW radiated power for diffuse illumination in terahertz imaging applications," IEEE J. Solid-State Circuits **49**, 2938–2950 (2014).
326. C. Jiang, A. Mostajeran, R. Han, M. Emadi, H. Sherry, A. Cathelin, and E. Afshari, "A fully integrated 320 GHz coherent imaging transceiver in 130 nm SiGe BiCMOS," IEEE J. Solid-State Circuits **51**, 2596–2609 (2016).
327. B. Scherger, M. Reuter, M. Scheller, K. Altmann, N. Vieweg, R. Dabrowski, J. A. Deibel, and M. Koch, "Discrete terahertz beam steering with an electrically controlled liquid crystal device," J. Infrared Millim. Terahertz Waves **33**, 1117–1122 (2012).
328. S. Busch, B. Scherger, M. Scheller, and M. Koch, "Optically controlled terahertz beam steering and imaging," Opt. Lett. **37**, 1391–1393 (2012).
329. J. Neu, R. Beigang, and M. Rahm, "Metamaterial-based gradient index beam steerers for terahertz radiation," Appl. Phys. Lett. **103**, 041109 (2013).
330. M. I. B. Shams, Z. Jiang, S. M. Rahman, L. J. Cheng, J. L. Hesler, P. Fay, and L. Liu, "A 740-GHz dynamic two-dimensional beam-steering and forming antenna based on photo-induced reconfigurable Fresnel zone plates," IEEE Trans. Terahertz Sci. Technol. **7**, 310–319 (2017).

331. K. Maki and C. Otani, "Terahertz beam steering and frequency tuning by using the spatial dispersion of ultrafast laser pulses," Opt. Express **16**, 10158–10169 (2008).
332. H. Füser and M. Bieler, "Terahertz beam steering by optical coherent control," Appl. Phys. Lett. **102**, 251109 (2013).
333. B. C. Smith, J. F. Whitaker, and S. C. Rand, "Steerable THz pulses from thin emitters via optical pulse-front tilt," Opt. Express **24**, 20755–20762 (2016).
334. K. Sengupta and A. Hajimiri, "Mutual synchronization for power generation and beam-steering in CMOS with on-chip sense antennas near 200 GHz," IEEE Trans. Microw. Theory Tech. **63**, 2867–2876 (2015).
335. G. Ok, K. Park, H. J. Kim, H. S. Chun, and S.-W. Choi, "High-speed terahertz imaging toward food quality inspection," Appl. Opt. **53**, 1406–1412 (2014).
336. S. Katletz, M. Pfleger, H. Pühringer, N. Vieweg, B. Scherger, B. Heinen, M. Koch, and K. Wiesauer, "Efficient terahertz en-face imaging," Opt. Express **19**, 23042–23053 (2011).
337. D.-S. Yee, K. H. Jin, J. S. Yahng, H.-S. Yang, C. Y. Kim, and J. C. Ye, "High-speed terahertz reflection three-dimensional imaging using beam steering," Opt. Express **23**, 5027–5034 (2015).
338. G. Ok, K. Park, H. S. Chun, H.-J. Chang, N. Lee, and S.-W. Choi, "High-performance sub-terahertz transmission imaging system for food inspection," Biomed. Opt. Express **6**, 1929–1941 (2015).
339. M. Wienold, T. Hagelschuer, N. Rothbart, L. Schrottke, K. Biermann, H. T. Grahn, and H. W. Hübers, "Real-time terahertz imaging through self-mixing in a quantum-cascade laser," Appl. Phys. Lett. **109**, 011102 (2016).
340. N. Llombart, R. J. Dengler, and K. B. Cooper, "Terahertz antenna system for a near-video-rate radar imager [Antenna Applications]," IEEE Antennas Propag. Mag. **52**(5), 251–259 (2010).
341. N. Llombart, K. B. Cooper, R. J. Dengler, T. Bryllert, and P. H. Siegel, "Confocal ellipsoidal reflector system for a mechanically scanned active terahertz imager," IEEE Trans. Antennas Propag. **58**, 1834–1841 (2010).
342. K. B. Cooper, R. J. Dengler, N. Llombart, B. Thomas, G. Chattopadhyay, and P. H. Siegel, "THz imaging radar for standoff personnel screening," IEEE Trans. Terahertz Sci. Technol. **1**, 169–182 (2011).
343. K. B. Cooper, R. J. Dengler, G. Chattopadhyay, E. Schlecht, J. Gill, A. Skalare, I. Mehdi, and P. H. Siegel, "A high-resolution imaging radar at 580 GHz," IEEE Microw. Wireless. Compon. Lett. **18**, 64–66 (2008).
344. K. B. Cooper, R. J. Dengler, N. Llombart, T. Bryllert, G. Chattopadhyay, E. Schlecht, J. Gill, C. Lee, A. Skalare, I. Mehdi, and P. H. Siegel, "Penetrating 3-D imaging at 4- and 25-m range using a submillimeter-wave radar," IEEE Trans. Microw. Theory Tech. **56**, 2771–2778 (2008).
345. A. Garcia-Pino, N. Llombart, B. Gonzalez-Valdes, and O. Rubinos-Lopez, "A bifocal ellipsoidal Gregorian reflector system for THz imaging applications," IEEE Trans. Antennas Propag. **60**, 4119–4129 (2012).
346. E. Heinz, T. May, D. Born, G. Zieger, K. Peiselt, V. Zakosarenko, T. Krause, A. Krüger, M. Schulz, F. Bauer, and H.-G. Meyer, "Progress in passive submillimeter-wave video imaging," Proc. SPIE **9078**, 907808 (2014).
347. E. Heinz, T. May, D. Born, G. Zieger, S. Anders, V. Zakosarenko, H. G. Meyer, and C. Schäffel, "Passive 350 GHz video imaging systems for security applications," J. Infrared Millim. Terahertz Waves **36**, 879–895 (2015).
348. M. F. Duarte, M. A. Davenport, D. Takhar, J. N. Laska, T. Sun, K. F. Kelly, and R. G. Baraniuk, "Single-pixel imaging via compressive sampling," IEEE Signal Process. Mag. **25**(2), 83–91 (2008).

349. M. Harwit and N. J. A. Sloane, *Hadamard Transform Optics* (Elsevier, 1979).
350. Study Group VIII, International Telecommunication Union, "Terminal equipment and protocols for telematic services," ITU-T T.83 (11/1994) (ITU, 1988).
351. D. L. Donoho, "Compressed sensing," IEEE Trans. Inf. Theory **52**, 1289–1306 (2006).
352. E. J. Candès, J. Romberg, and T. Tao, "Robust uncertainty principles: exact signal reconstruction from highly incomplete frequency information," IEEE Trans. Inf. Theory **52**, 489–509 (2006).
353. M. Lustig, D. Donoho, and J. M. Pauly, "Sparse MRI: the application of compressed sensing for rapid MR imaging," Magn. Reson. Med. **58**, 1182–1195 (2007).
354. Y. Zhang, "Theory of compressive sensing via ℓ_1-minimization: a non-RIP analysis and extensions," J. Oper. Res. Soc. China **1**, 79–105 (2013).
355. E. J. Candes and M. B. Wakin, "An introduction to compressive sampling," IEEE Signal Process. Mag. **25**(2), 21–30 (2008).
356. M. Fornasier and H. Rauhut, "Compressive sensing," in *Handbook of Mathematical Methods in Imaging* (Springer, 2011), pp. 187–228.
357. E. van den Berg and M. P. Friedlander, "Probing the Pareto frontier for basis pursuit solutions," SIAM J. Sci. Comput. **31**, 890–912 (2009).
358. M. F. Duarte and Y. C. Eldar, "Structured compressed sensing: from theory to applications," IEEE Trans. Signal Process. **59**, 4053–4085 (2011).
359. Y. C. Pati, R. Rezaiifar, and P. S. Krishnaprasad, "Orthogonal matching pursuit: recursive function approximation with applications to wavelet decomposition," in *27th Asilomar Conference on Signals, Systems and Computers* (1993), pp. 40–44.
360. D. Needell and J. A. Tropp, "CoSaMP: iterative signal recovery from incomplete and inaccurate samples," Appl. Comput. Harmon. Anal. **26**, 301–321 (2009).
361. F. Marvasti, A. Amini, F. Haddadi, M. Soltanolkotabi, B. H. Khalaj, A. Aldroubi, S. Sanei, and J. Chambers, "A unified approach to sparse signal processing," EURASIP J. Adv. Signal Process. **2012**, 44 (2012).
362. C. M. Watts, C. C. Nadell, J. Montoya, S. Krishna, and W. J. Padilla, "Frequency-division-multiplexed single-pixel imaging with metamaterials," Optica **3**, 133–138 (2016).
363. C. C. Nadell, C. M. Watts, J. A. Montoya, S. Krishna, and W. J. Padilla, "Single pixel quadrature imaging with metamaterials," Adv. Opt. Mater. **4**, 66–69 (2016).
364. S. A. N. Saqueb and K. Sertel, "Phase-sensitive single-pixel THz imaging using intensity-only measurements," IEEE Trans. Terahertz Sci. Technol. **6**, 810–816 (2016).
365. W. L. Chan, M. L. Moravec, R. G. Baraniuk, and D. M. Mittleman, "Terahertz imaging with compressed sensing and phase retrieval," Opt. Lett. **33**, 974–976 (2008).
366. W. L. Chan, K. Charan, D. Takhar, K. F. Kelly, R. G. Baraniuk, and D. M. Mittleman, "A single-pixel terahertz imaging system based on compressed sensing," Appl. Phys. Lett. **93**, 121105 (2008).
367. W. L. Chan, M. L. Moravec, R. G. Baraniuk, and D. M. Mittleman, "Terahertz imaging with compressed sensing and phase retrieval," in *Conference on Lasers and Electro-Optics (CLEO)* (OSA, 2007), Vol. **33**, paper CThU4.
368. S. Yu, A. Shaharyar Khwaja, and J. Ma, "Compressed sensing of complex-valued data," Signal Process. **92**, 357–362 (2012).
369. Y. C. Shen, L. Gan, M. Stringer, A. Burnett, K. Tych, H. Shen, J. E. Cunningham, E. P. J. Parrott, J. A. Zeitler, L. F. Gladden, E. H. Linfield, and

A. G. Davies, "Terahertz pulsed spectroscopic imaging using optimized binary masks," Appl. Phys. Lett. **95**, 231112 (2009).
370. N. P. Pitsianis, D. J. Brady, and X. Sun, "Sensor-layer image compression based on the quantized cosine transform," Proc. SPIE **5817**, 250–257 (2005).
371. Z. Xu and E. Y. Lam, "Image reconstruction using spectroscopic and hyperspectral information for compressive terahertz imaging," J. Opt. Soc. Am. A **27**, 1638–1646 (2010).
372. H. Shen, L. Gan, N. Newman, Y. Dong, C. Li, Y. Huang, and Y. C. Shen, "Spinning disk for compressive imaging," Opt. Lett. **37**, 46–48 (2012).
373. K. H. Jin, Y. Kim, D.-S. Yee, O. K. Lee, and J. C. Ye, "Compressed sensing pulse-echo mode terahertz reflectance tomography," Opt. Lett. **34**, 3863–3865 (2009).
374. L. Gan, "Block compressed sensing of natural images," in *15th International Conference on Digital Signal Processing (DSP)* (2007), pp. 403–406.
375. M. Rahm, J. S. Li, and W. J. Padilla, "THz wave modulators: a brief review on different modulation techniques," J. Infrared Millim. Terahertz Waves **34**, 1–27 (2013).
376. Y. Bai, T. Bu, K. Chen, and S. Zhuang, "Review about the optical-controlled terahertz waves modulator," Appl. Spectrosc. Rev. **50**, 707–727 (2015).
377. M. R. Hashemi, S. Cakmakyapan, and M. Jarrahi, "Reconfigurable metamaterials for terahertz wave manipulation," Rep. Prog. Phys. **80**, 094501 (2017).
378. R. Degl'Innocenti, S. J. Kindness, H. E. Beere, and D. A. Ritchie, "All-integrated terahertz modulators," Nanophotonics **7**, 127–144 (2018).
379. H. Alius and G. Dodel, "Amplitude-, phase-, and frequency modulation of far-infrared radiation by optical excitation of silicon," Infrared Phys. **32**, 1–11 (1991).
380. D. Shrekenhamer, C. M. Watts, and W. J. Padilla, "Terahertz single pixel imaging with an optically controlled dynamic spatial light modulator," Opt. Express **21**, 12507–12518 (2013).
381. L. Liu, S. Rahman, L.-J. Cheng, P. Fay, Z. Jiang, J. Qayyum, M. I. B. Shams, and H. G. Xing, "Approaching real-time terahertz imaging with photo-induced coded apertures and compressed sensing," Electron. Lett. **50**, 801–803 (2014).
382. A. Kannegulla, Z. Jiang, S. M. Rahman, M. I. B. Shams, P. Fay, H. G. Xing, L. J. Cheng, and L. Liu, "Coded-aperture imaging using photo-induced reconfigurable aperture arrays for mapping terahertz beams," IEEE Trans. Terahertz Sci. Technol. **4**, 321–327 (2014).
383. S. Augustin, J. Hieronymus, P. Jung, and H. W. Hübers, "Compressed sensing in a fully non-mechanical 350 GHz imaging setting," J. Infrared Millim. Terahertz Waves **36**, 496–512 (2015).
384. E. J. Candès, T. Strohmer, and V. Voroninski, "PhaseLift: exact and stable signal recovery from magnitude measurements via convex programming," Commun. Pure Appl. Math. **66**, 1241–1274 (2013).
385. R. I. Stantchev, B. Sun, S. M. Hornett, P. A. Hobson, G. M. Gibson, M. J. Padgett, and E. Hendry, "Noninvasive, near-field terahertz imaging of hidden objects using a single-pixel detector," Sci. Adv. **2**, e1600190 (2016).
386. S. M. Hornett, R. I. Stantchev, M. Z. Vardaki, C. Beckerleg, and E. Hendry, "Subwavelength terahertz imaging of graphene photoconductivity," Nano Lett. **16**, 7019–7024 (2016).
387. R. I. Stantchev, D. B. Phillips, P. Hobson, S. M. Hornett, M. J. Padgett, and E. Hendry, "Compressed sensing with near-field THz radiation," Optica **4**, 989–992 (2017).
388. D. B. Phillips, M.-J. Sun, J. M. Taylor, M. P. Edgar, S. M. Barnett, G. M. Gibson, and M. J. Padgett, "Adaptive foveated single-pixel imaging with dynamic supersampling," Sci. Adv. **3**, e1601782 (2017).

389. W. L. Chan, H. T. Chen, A. J. Taylor, I. Brener, M. J. Cich, and D. M. Mittleman, "A spatial light modulator for terahertz beams," Appl. Phys. Lett. **94**, 213511 (2009).
390. C. M. Watts, D. Shrekenhamer, J. Montoya, G. Lipworth, J. Hunt, T. Sleasman, S. Krishna, D. R. Smith, and W. J. Padilla, "Terahertz compressive imaging with metamaterial spatial light modulators," Nat. Photonics **8**, 605–609 (2014).
391. H.-T. Chen, W. J. Padilla, J. M. O. Zide, A. C. Gossard, A. J. Taylor, and R. D. Averitt, "Active terahertz metamaterial devices," Nature **444**, 597–600 (2006).
392. N. I. Landy, S. Sajuyigbe, J. J. Mock, D. R. Smith, and W. J. Padilla, "Perfect metamaterial absorber," Phys. Rev. Lett. **100**, 207402 (2008).
393. K. Goda, K. K. Tsia, and B. Jalali, "Serial time-encoded amplified imaging for real-time observation of fast dynamic phenomena," Nature **458**, 1145–1149 (2009).
394. A. Mahjoubfar, D. V. Churkin, S. Barland, N. Broderick, S. K. Turitsyn, and B. Jalali, "Time stretch and its applications," Nat. Photonics **11**, 341–351 (2017).
395. S. A. Diddams, L. Hollberg, and V. Mbele, "Molecular fingerprinting with the resolved modes of a femtosecond laser frequency comb," Nature **445**, 627–630 (2007).
396. S. Schumann, C. Jansen, M. Schwerdtfeger, S. F. Busch, O. Peters, M. Scheller, and M. Koch, "Spectrum to space transformed fast terahertz imaging," Opt. Express **20**, 19200–19205 (2012).
397. M. E. Gehm, R. John, D. J. Brady, R. M. Willett, and T. J. Schulz, "Single-shot compressive spectral imaging with a dual-disperser architecture," Opt. Express **15**, 14013–14027 (2007).
398. A. Wagadarikar, R. John, R. Willett, and D. Brady, "Single disperser design for coded aperture snapshot spectral imaging," Appl. Opt. **47**, B44–B51 (2008).
399. O. Furxhi, D. L. Marks, and D. J. Brady, "Echelle crossed grating millimeter wave beam scanner," Opt. Express **22**, 16393–16407 (2014).
400. K. Lee, H. J. Choi, J. Son, H.-S. Park, J. Ahn, and B. Min, "THz near-field spectral encoding imaging using a rainbow metasurface," Sci. Rep. **5**, 14403 (2015).
401. E.-M. Stübling, S. Busch, J. C. Balzer, and M. Koch, "Development of a multi-channel time-to-space terahertz spectrometer," Opt. Express **24**, 23146–23153 (2016).
402. K. Lee, K. H. Jin, J. C. Ye, and J. Ahn, "Coherent optical computing for T-ray imaging," Opt. Lett. **35**, 508–510 (2010).
403. K. Lee and J. Ahn, "Single-pixel coherent diffraction imaging," Appl. Phys. Lett. **97**, 241101 (2010).
404. H. Guerboukha, K. Nallappan, and M. Skorobogatiy, "Exploiting k-space/frequency duality toward real-time terahertz imaging," Optica **5**, 109–116 (2018).

Hichem Guerboukha received a B.Sc. degree in Engineering Physics and a M.Sc. degree in Applied Science from the Polytechnique Montréal, Montréal, Quebec, Canada, in 2014 and 2015, respectively. He is currently working toward a Ph.D. degree in THz computational imaging. His research interests include THz instrumentation and waveguides, THz communications, and THz computational imaging. He was the recipient of the Etoile Student-Researcher from Fonds de Recherche–Nature et Technologies in 2015 and the Best M.S. Thesis Prize from the Polytechnique Montréal in 2015.

Kathirvel Nallappan received a B.E. degree in Electronics and Communication Engineering and a M.Tech degree in Laser and Electro-optical Engineering during 2010 and 2013, respectively, from Anna University, Tamilnadu, India. After working as a Senior Project Fellow in the Structural Engineering Research Center (CSIR), India for a period of one year, he joined as a research intern in the research group of Prof. Maksim Skorobogatiy at Polytechnique Montréal, Canada. He is currently working toward the Ph.D. degree in Terahertz Communications at Polytechnique Montréal. His research interest includes terahertz and infrared free space communications, THz waveguides, spectroscopy, and imaging.

Maksim Skorobogatiy has been a Professor of Engineering Physics at Polytechnique Montréal since 2003. He graduated in 2001 from MIT with a Ph.D. in Physics and an M.Sc. in Electrical Engineering and Computer Science. He then worked at the MIT spin-off Omniguide Inc. on the development of hollow-core fibers for guidance of high-power mid-IR laser beams. He was awarded a Tier 2 Canada Research Chair (CRC) in Micro and Nano Photonics and then a Tier 1 CRC in Ubiquitous THz Photonics in 2016. Thanks to the support of the CRC program, he could pursue many high-risk exploratory projects in guided optics, and recently THz photonics, which have resulted in significant contributions in these two booming research fields. In 2012 he was awarded the rank of Professional Engineer by the Order of Engineers of Québec, Canada. In 2017, he was promoted to Fellow of The Optical Society (OSA) for his pioneering contributions to the development of microstructured and photonic crystal multimaterial fibers and their applications to light delivery, sensing, smart textiles, and arts. Additionally, in 2017 he was promoted to Senior Member of the IEEE for his contributions in engineering and applied research.